DEVELOPMENT OF MESOSCALE AND MICROSCALE METHODS FOR THE MECHANICAL CHARACTERIZATION OF CELLS AND CELL-SUBSTRATE INTERACTIONS

by

ONUR AYDIN

A Thesis Submitted to the
Graduate School of Engineering
in Partial Fulfillment of the Requirements for
the Degree of

Master of Science
in
Mechanical Engineering

KOC UNIVERSITY
JULY 2015

Koç University
Graduate School of Sciences and Engineering

This is to certify that I have examined this copy of a master's thesis by

Onur Aydın

and have found that it is complete and satisfactory in all respects,
and that any and all revisions required by the final
examining committee have been made.

Committee Members:

_____
B. Erdem Alaca, Ph.D. (Advisor)

_____
Halil Bayraktar, Ph.D.

_____
Mehmet Z. Baykara, Ph.D.

Date: _____

ABSTRACT

Mechanical factors that affect cells play key roles in many human diseases such as myopathies, neurodegenerative diseases, and cancer metastasis. Mechanical characterization of cells and cell-substrate interactions is therefore significant to the diagnosis and treatment of such diseases. Moreover, understanding cell mechanics can facilitate the integration of cells into machine design at the microscale. In this study, a mesoscale and a microscale method are developed for the mechanical characterization of cells and cell-substrate interactions.

The mesoscale approach is to integrate uniaxial stretching with optical microscopy. A custom built stretcher device is developed for deforming an elastic substrate and adherent cells. Microscopy is used to image both the substrate and the cells. Substrates with embedded fluorescent microspheres are prepared to demonstrate the measurement of local in-plane strain fields. This method enables establishing accurate correlations between substrate deformation and cell response.

The microscale approach is based on the idea of building a smart surface comprising an array of MEMS sensors to measure traction forces between adherent cells and the surface itself. Electromechanical design of a single MEMS traction sensor utilizing piezoresistive silicon nanowires is reported. The design process is geared towards optimizing both the piezoresistive response, and the mechanical sensitivity. The design of a suitable fabrication flow is also reported and the initial fabrication results are presented. In concluding, a method for the characterization of MEMS sensor, and design methodology and fabrication approach for a sensor array are proposed for future research.

ÖZET

Canlı hücreler üzerindeki mekanik etkilerin kas ve sinir dokusu hastalıkları ve kanser metastazı gibi birçok hastalıkta rol oynadığı bilinmektedir. Hücrelerin mekanik özelliklerinin ve hücre-alttaş etkileşim kuvvetlerinin ölçümü, bu hastalıkların teşhis ve tedavisi için ciddi önem taşımaktadır. Ayrıca, hücre mekaniğinin daha iyi anlaşılması, hücrelerin mikro ölçekte makine elemanı olarak kullanılmasını mümkün kılabilir. Bu çalışmada, hücrelerin mekanik özelliklerinin ve hücre-alttaş etkileşim kuvvetlerinin ölçümü için orta ve küçük ölçekte olmak üzere iki yöntem geliştirilmiştir.

Orta ölçekte geliştirilen yöntem, tek eksenli çekme ile optik mikroskobun tümleştirilmesi yoluyla çalışmaktadır. Geliştirilen tek eksenli çekme cihazı, üzerinde hücreler bulunan elastik numuneye gerinim uygulamak için, mikroskop da hücreleri ve numuneyi görüntülemek için kullanılmaktadır. İçerisinde gömülü floresan kürecikler olan numuneler hazırlanarak yerel gerinim ölçümü gerçekleştirilmiştir. Bu ölçüm, hücrelerin tepkileri ve davranışları ile üzerinde bulundukları numunenin mekanik deformasyonu arasında kesin bağıntılar kurulmasını sağlayabilir.

Mikro ölçekte yapılan çalışma, tek bir hücre ile tutunduğu yüzey arasındaki etkileşim kuvvetlerinin ölçümü için tasarlanan MEMS algılayıcı üzerinedir. Tasarlanan kuvvet algılayıcı, piezorezistif nanotel bileşkeler kullanarak uygulanan kuvvetin elektronik sinyale dönüştürülmesi yoluyla çalışmaktadır. Çalışma kapsamında, MEMS kuvvet algılayıcının elektromekanik tasarımı ve imalat süreç akışı geliştirilmiştir. Tasarım aşamasında piezorezistif bileşkelerin hassaslığı ve mekanik yapının uygulanan kuvveti nanotellere aktarmadaki verimliliği göz önünde bulundurulmuştur. MEMS algılayıcının ilk prototip tasarımı, imalat süreç akışı ve imalattan alınan ön çıktılar sunulmakta ve çalışmanın devamı ile ilgili olarak, uygun karakterizasyon yöntemi ve algılayıcı dizisi için imalat süreci önerilmektedir.

ACKNOWLEDGEMENTS

I am deeply grateful to Dr. Erdem Alaca for the guidance he has given me throughout the past four years and for the opportunity to join his research group. I also thank Dr. Halil Bayraktar for his guidance throughout my graduate study.

I would like to thank my colleagues Gökhan Nadar and Bekir Aksoy for their contributions to this work.

On behalf of everyone working on our MEMS sensor project, I would like to thank Aziz Ulvi Çalışkan, Sema İmrahor İlyas, Ardınç Edis, Cüneyt Bağcıoğlu, Murat Pak, Tarık Akyol, and Aylin Ersoy for their collaboration and their work on the fabrication stage of our MEMS sensor project.

I would also like to thank Dr. Arda Yalçınkaya for his insight and recommendations on the MEMS sensor design.

I am grateful to my parents for their unconditional support and encouragement.

This work was financially supported by the Scientific and Technological Research Council of Turkey (TUBITAK) under Grants 112E580 and 112T823.

TABLE OF CONTENTS

LIST OF TABLES

LIST OF FIGURES

NOMENCLATURE

MEMS	Micro-electromechanical systems
IF	Intermediate filaments
AFM	Atomic force microscopy
DIC	Digital image correlation
I/O	Input/Output
DAQ	Data acquisition
DM	Dichroic mirror
M	Mirror
EmF	Emission filter
ExF	Excitation filter
PDMS	Poly dimethylsiloxane
CNC	Computer numeric control
NW	Nanowire
DC	Direct current
SMU	Source-measure unit
CMOS	Complementary metal-oxide-semiconductor
SOI	Silicon on insulator
BOX	Buried oxide
RIE	Reactive ion etching
HF	Hydrofluoric acid
UV	Ultraviolet
ω_c	Cut-off frequency of the passive low pass filter
R^2	Coefficient of correlation
y_1, y_2, y_0	Coordinates of the edges and center point of sample in y direction
x_1, x_2, x_0	Coordinates of the edges and center point of sample in x direction
v	Stretching speed
$\boldsymbol{x}$	Positions of beads at any time
$\boldsymbol{X}$	Initial positions of beads
t	Time
$\boldsymbol{\phi}$	Position function
$\boldsymbol{u}$	Displacement vector
$\boldsymbol{\nabla u}_{iK}$	Displacement gradient tensor
$\boldsymbol{I}$	Identity tensor

$\boldsymbol{F}$	Deformation gradient tensor
$\boldsymbol{C}$	Right Cauchy-Green deformation tensor
$\boldsymbol{E}$	Green-Saint-Venant strain tensor
ε_{xx}	Longitudinal component of strain
ε_{yy}	Lateral component of strain
$\varepsilon_{xy}, \varepsilon_{yx}$	Shear components of strain
$\boldsymbol{E}_i$	Electric field vector
$\boldsymbol{i}_j$	Current vector
$\boldsymbol{\rho}_{ij}$	Resistivity tensor
$\Delta\boldsymbol{\rho}_{ij}$	Change in resistivity tensor
ρ_0	Resistivity in the unstressed state
$\boldsymbol{\sigma}_{kl}$	Stress tensor
$\boldsymbol{\pi}_{ijkl}$	Piezoresistance tensor
π_L, π_T	Effective longitudinal and transverse piezoresistance coefficients
N	Dopant concentration
T	Temperature
P(N,T)	Piezoresistance factor as a function of dopant concentration and temperature
$\Delta\rho/\rho_0$	Relative change in resistivity
$\Delta R/R_0$	Relative change in resistance
$\Delta I/I_0$	Relative change in current
E_{eff}	Effective elastic modulus
ε	Axial strain applied on the nanowires
G	Piezoresistance gauge factor
θ	Angle of the applied force vector with the positive x-axis
ε_1	Axial strain on the horizontal nanowires
ε_2	Axial strain on the vertical nanowires
σ_a	Axial stress on the nanowires
σ'	von-Mises stress

Chapter 1

INTRODUCTION

The recent advances in molecular biology and the human genome project have made it increasingly simple to understand the building blocks of life. However, the effects of external mechanical stimuli on the synthesis, assembly, and function of the biological building blocks still remain mostly unclear. Cell mechanics, external physical forces, and the mechanics of extracellular environment play crucial roles in many human diseases. Among these examples are osteogenesis imperfecta (brittle bone disease) caused by abnormalities in extracellular matrix, metastasis due to tumor cell adhesion assisted by hydrodynamic flow, emphysema resulting from decreased lung rigidity, asthma resulting from the constriction of air ducts, hypertension due to increased blood vessel wall rigidity, and the adhesion of red blood cells to endothelium observed in sickle cell anemia.

The small size scale and the small magnitudes of the physical forces that are involved provide major challenges for the study of cell mechanics and the mechanics of cell-substrate interactions. Despite the challenges, studies on the mechanics of cells and cell-substrate interactions are important for the understanding of cell mechanics. Advancing our knowledge on cell mechanics can lead the way to the diagnosis and treatment of many human diseases that are related to mechanical effects.

In this study, we present a review of cell mechanics and develop two methods for the mechanical characterization of cells and cell-substrate interactions in mesoscale and microscale.

Chapter 2 provides a literature review on cell mechanics with focus on the effects of external mechanical stimuli on cell response, the methods for the mechanical characterization of cells and the forces between cells and extracellular environment, and the intermediate filament networks.

Chapter 3 describes the design and operation of a uniaxial tensile stretcher integrated with fluorescent microscopy that is designed for cell mechanics studies at the mesoscale. A technique for the quantitative measurement of local deformations of the stretched sample using embedded fluorescent microspheres is developed and demonstrated.

Chapter 4 details the electromechanical design, fabrication, and characterization of a MEMS traction sensor utilizing piezoresistive silicon nanowires that is to be used for the measurement of surface traction forces between the sensor itself and adherent cells. The fundamental principles underlying the electromechanical design are discussed. A complete fabrication process flow is proposed and the initial fabrication result is presented. A method for the characterization of the designed MEMS sensor device is also proposed.

This thesis is concluded with a summary of the work that was performed and an outlook on the future efforts is given.

Chapter 2

LITERATURE REVIEW

2.1. Mechanical effects influencing cell response

Living organisms have a much more complex structure compared to traditional engineering materials such as metals, ceramics, and polymers. In the last few years, the correlations between structure, mechanical behavior, and biological function have been studied for various cells, tissues, and organs. Studies on heart, lung, bone, blood vessel, and skeletal and cardiac muscle have revealed important connections between biomechanics and biological function and enabled advances in the diagnosis and treatment of various orthopedic, cardiac, circulatory, and pulmonary diseases [1, 2]. It is a widely accepted opinion that mechanical forces play an active role in cellular processes. Hence, there is a need for the systematic investigation of the mechano-transduction mechanisms at both the cellular and the molecular level.

In vitro studies revealed that both the mechanics of the extracellular environment [3, 4] and externally applied forces [5, 6] have significant effect on cell differentiation, cell growth, morphology, and motility. Altering the mechanical properties of the substrate is shown to have direct consequences in stem cell differentiation [3]. Moreover, cell growth and development are directly influenced by substrate rigidity [4, 7]. In a study by Lo *et al* [8], it was demonstrated that cell movement can be guided by manipulating the mechanical properties of the substrate. *In vivo* studies have also resulted in similar observations. For instance, genetic expression is shown to be significantly affected by shear stress in endothelial cells [9]. Other studies have shown that various cellular processes are governed by the interactions of cells with extracellular matrix through focal adhesion cites [10, 11].

Mechanical interactions also have a significant effect on neurons. The high amount of tension that axons undergo during traumatic brain injuries cause neuron death [12] whereas continuous tensile loading at a slow rate assists in neural growth [13]. Neurons grow in a non-

homogeneous mechanical environment consisting of glial cells [14, 15]. Zheng *et al* [5] found that within the range of 0.5–1.5 nN, every 10 pN increment in axial tension increases axon growth rate by 1.5 μm/hour. Franze *et al* [6] observed that mechanical stresses that exceed a threshold value of 275 pN/mm^2 cause the neuronal growth cones to collapse as a result of which, the neuron retracts and continues growth toward a softer substrate. Tensile stress acting on the axons also causes accumulation of neurotransmitter vesicles at the presynaptic terminals [16]. Measurement of neuron response to mechanical stimuli is of prime importance for a better understanding of neural activities. Information and insight provided by such investigations are crucial for the treatment of pathological neuron behavior such as axon growth post trauma [7] and the apprehension of memory and learning processes [16].

Alterations in cell mechanics can also cause function loss. For instance the red blood cells, due to their biconcave structure, can undergo large amounts of elastic deformation, enabling them to pass inside very narrow capillaries. However, malaria infection causes red blood cells to lose their elasticity and get a spherical shape [17]. As a result, they can no longer pass inside the narrow capillaries, causing blockages and organ failure.

The mechanical interaction forces between cells and the extracellular environment play key roles in numerous cellular functions [18-21]. Different extracellular environments impose different mechanical forces on cells, such as the expansion and contraction during heart beating, cyclic tensile loading during exhaling and inhaling, or the peristaltic movements of various organs [22, 23]. Cell migration, for instance, does not only depend on the biochemical composition but also the mechanical properties of the extracellular environment [24]. Cells can probe the extracellular environment and asses its mechanical properties such as the stiffness of the substrate that they are adhered to [8, 25, 26]. During the formation of organs, changes in the stiffness of the extracellular substrate can cause changes in the cell's cytoskeletal organization and even the cell's type, thus cells differentiate, conforming to the specific tissue that they belong to [27, 28]. Studies also showed that groups of two different types of cells randomly dispersed in an environment migrate and with time form cell clusters consisting of cells of similar mechanical properties [29, 30]. Although the biochemical structures that function as mechanisms of cell adhesion and spreading have been explained, there is little information regarding the dynamics of systems comprising such structures and their direct effect on cell physiology.

The changes and developments in cell cytoskeleton are of prime importance during the development stage when organs form. In several studies, cells were placed on substrates

consisting of pillar arrays with different spacing values between the pillars. One observation was that endothelial cells placed on densely spaced pillars began apoptosis (programmed cell death) whereas when they were placed on sparsely distributed pillars, cells remained healthy and were able to divide [31-33].

The network of structural filaments in the cell, namely the cytoskeleton, is a key factor determining the cell's sensitivity and response to external mechanical stimuli. Especially, protein filament structures known as intermediate filaments (IFs) which constitute part of the cytoskeleton are known to provide and maintain the mechanical integrity of biological cells [34, 35]. Numerous studies have shown that cells lacking a proper IF network due to mutations in genes that code for the IF proteins experience significant embrittlement, and such mutations that disturb the IF network cause various human diseases [36-39]. The IF proteins have filament structures having diameters on the order of 10 nm [40]. IF proteins are cell-specific and therefore there are different IF filaments present in different cell types. For instance, epithelial cells have keratin filaments, muscle cells have desmin filaments, and neurons have vimentin, nestin, and peripherin filaments.

Intermediate filaments have important functions in the formation and preservation of neurons which have a unique and highly heterogeneous morphology [41]. Neurons consist of a small cytoplasm, multiple extensions called dendrites, and a single extension called the axon. Axons can be very long structures and neuronal IFs play key roles in axons' formation, growth, and mechanical integrity [41]. The IF filaments are synthesized at the cell body and transported to the axons and dendrites by microtubules [42-45]. The IFs may be damaged during transportation from the cell body to the axons and dendrites. Such damage can affect the neurophysiological development and cause complications. It has been observed that different types of IFs are synthesized at different stages of axonal growth. Studies have shown that IFs play a key role in the formation of axons and in maintaining their mechanical integrity from formation through growth [46].

Understanding the contributions of IFs to cell mechanics requires simultaneous characterization of the mechanical forces and the dynamic changes in IF synthesis, assembly, and motility [47-49]. Although the characterization of mechanical interactions and intracellular dynamics can provide valuable insight into the roles of IFs in cells and tissues; carrying out such measurements simultaneously is a challenge [50, 51]. The development of nanoscale electromechanical sensing platforms can enable the measurement of mechanical interactions without relying on microscopy methods. This way, the intracellular dynamics of

IFs can be studied by epifluorescence microscopy while simultaneous mechanical measurements are carried out by the nano-electromechanical sensing platforms [52, 53].

2.2. Mechanical characterization of cells and cell-substrate interactions

Despite the importance of identifying and characterizing mechanics of cells and cell-substrate interactions, progress has been limited in the area. Mechanical characterization of forces at the single cell and molecule level requires experimental instrumentation that is highly complex and difficult to realize. The rigidity of living cells are approximately seven order of magnitudes lower than that of traditional engineering materials which are metals, ceramics, and polymers (Figure 2.1). The rigidity and morphology of cells depend on the cytoskeleton whose structure and function is influenced by cell-cell and cell-substrate interactions. For the experimental characterization of mechanical forces involved in these interactions, one important consideration is the controlled application of load on the cell while maintaining adhesion of the cell to the substrate, and the measurement of interaction forces between the cell and the substrate. Another consideration is the careful measurement of the displacements caused by the applied load. There are several methods reported in the literature for the mechanical stimulation of single cells. The applied load can be in the form of uniaxial or biaxial tension or compression, shearing, hydrostatic pressure, bending, or torsion. Some methods utilize various probes to locally deform the cell whereas in other methods the entire cell is subjected to mechanical load. Another approach for the characterization of cell mechanics and mechanics of cell-substrate interactions involves the mechanical stimulation of a group of cells.

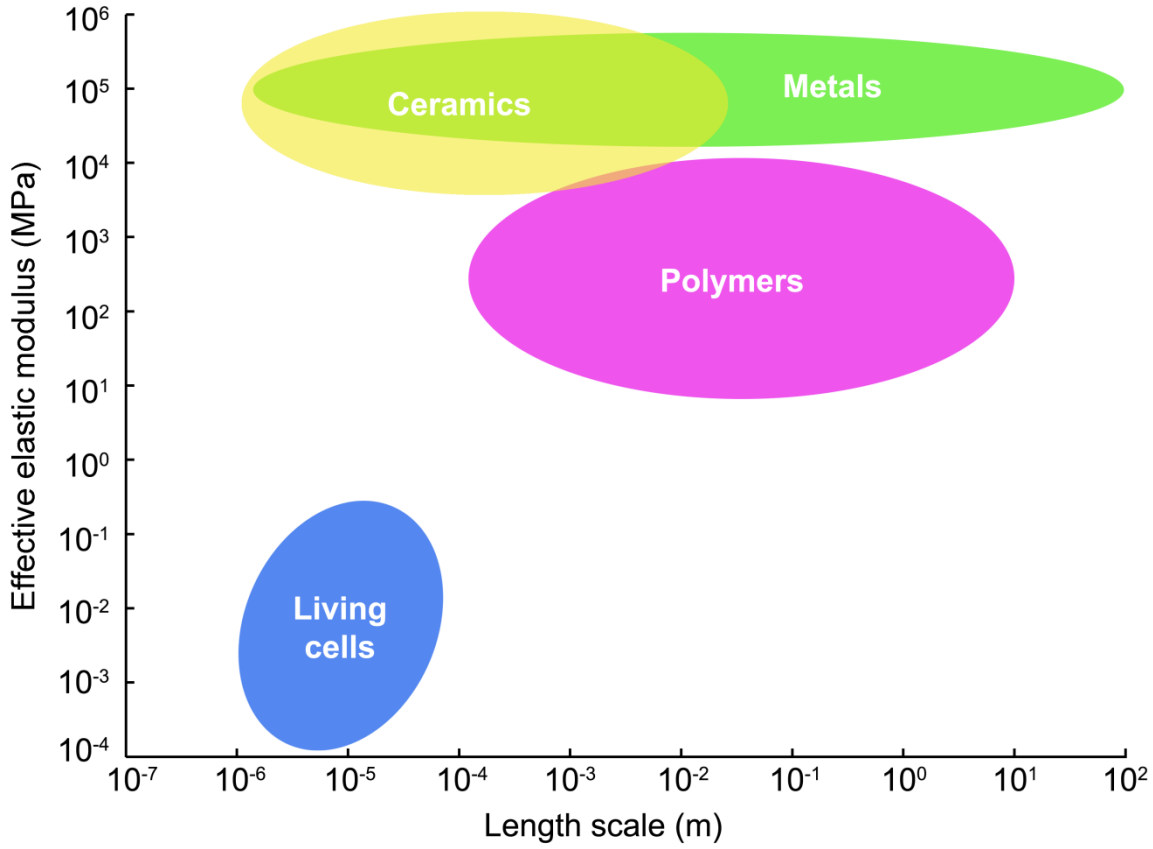

Figure 2.1: A comparison of the rigidity and characteristic dimension of biological cells with those of traditional engineering materials [54].

2.2.1. Common non-MEMS methods for mechanical stimulation of cells

A majority of the methods besides MEMS that used for the mechanical stimulation of cells are reviewed (Figure 2.2) [54, 55]:

1.) A glass probe manipulated by a piezoelectric actuator locally deforming the cell membrane.

2.) Stretching of the silicone elastomer membrane having cells adhered on the surface. This technique can be utilized to apply loads on 10^2 to 10^4 cells simultaneously. The loading can be uniaxial or biaxial.

3.) Micropipette aspiration where a portion of the cell membrane is sucked into a small glass tube by applying a negative pressure. This is the most commonly employed technique for the mechanical characterization of cells. Force measurement resolution depends on the pressure measurement technique that is employed. It is possible to use this technique to measure the elastic properties of the cell if friction is neglected.

However, the high magnitudes of local stress and the complexity of the generated stress-state make such characterizations difficult.

4.) Application of shear stress to a cell or a group of cells by subjecting them to a fluid flow. It is possible to determine the applied shear stress using a viscometer or a parallel plate flow cell.

5.) Swelling or constriction of cell by altering osmotic pressure. This method can be used for the mechanical stimulation of cells but the quantitative measurement of forces is not possible.

6.) Mechanical stimulation of the cell using an atomic force microscopy (AFM) probe. This method enables very precise measurement of the applied force. The AFM tip is usually functionalized to achieve contact with the cell in a selective manner, enabling the measurement of forces due to specific biochemical interactions. However, AFM experiments suffer from several complications including the complexity of the AFM setup, and the influence of the aqueous environment on the physical interaction between the cell and the AFM tip. Furthermore, the photodiodes used in the AFM method to measure the applied force are capable of detecting displacements in a limited range which depends on the stiffness of the AFM cantilever. This makes it infeasible to carry out force measurements in a wide range using a single AFM probe.

7.) Applying force on the cell using magnetic beads. Using this method, it is possible to determine the elastic and viscoelastic properties of cells if a proper analysis of the applied deformation is implemented. A problem encountered in such experiments is the decrease in the magnitude of magnetic force with smaller bead size. This problem can be solved by increasing magnetic bead size but the method becomes inapplicable if the bead becomes as large as the sample cell.

8.) Applying forces on cells using optical tweezers and various particles. This method can be used to apply forces below 0.1 nN which enables experiments on the single molecule level. To apply forces exceeding 0.1 nN, the laser power needs to be increased which causes damage to the sample cells.

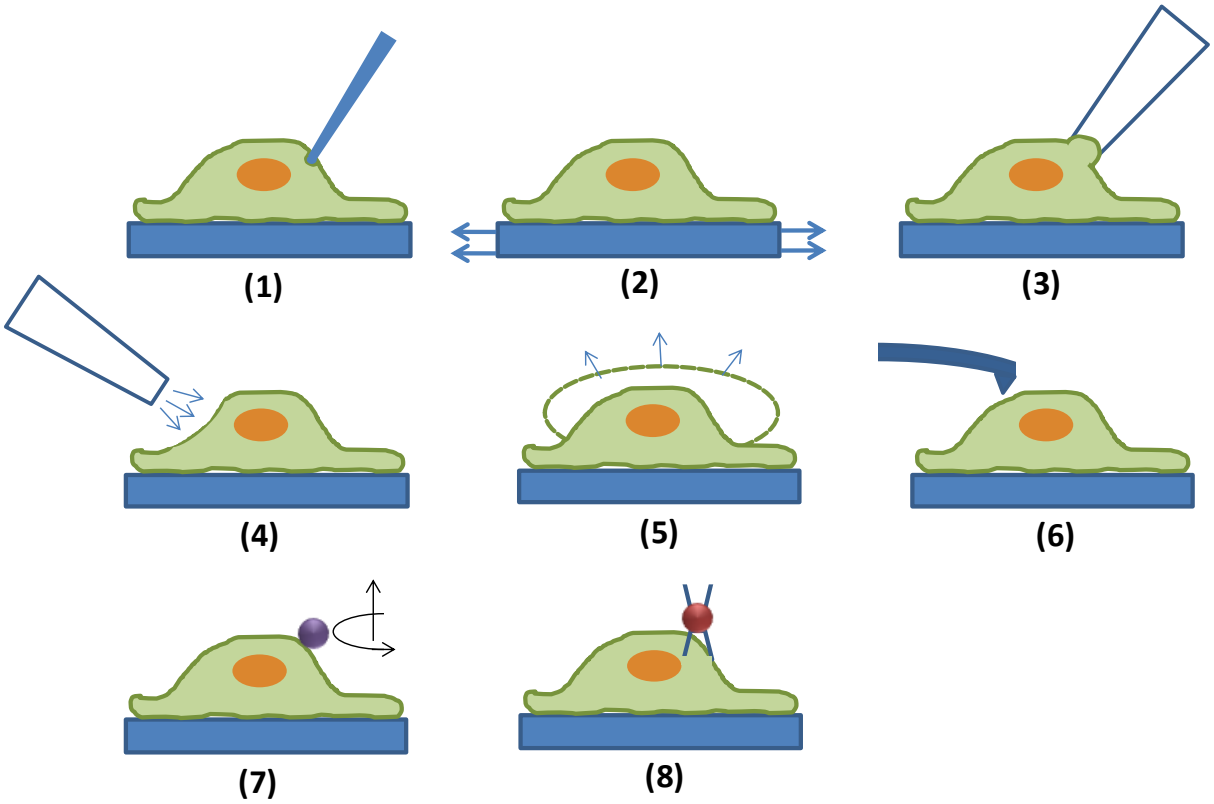

Figure 2.2: Common methods for mechanical stimulation of cells [54, 56].

The aforementioned techniques have made significant progress in cell mechanics. Nevertheless, more effective measurements require overcoming challenges common to most of these methods. Most of the methods described above enable indirect measurement of elastic and viscoelastic properties of cells. The reason for this is the complexity of the loading conditions and the substrate, which also makes it difficult to compare experimental results with cell mechanics models. Furthermore, the commonly employed mechanical cell stimulation techniques offer a single mode of stimulation or measurement. The complex and bulky instrumentation often do not allow for different kinds of stimulation or measurement to be carried out simultaneously. Probing a cell with multiple AFM tips simultaneously, for instance, while being an experiment that would provide valuable insight, is impractical [55].

MEMS have proven to be a valuable approach in cell mechanics due to the advantage of quantitative determination of cellular forces. MEMS sensors, due to their ability to measure displacements, also eliminate the need for optical microscopy for displacement measurement. These advantages have crucial implications, one of which is that the optical microscopy methods can be used for the assessment of cellular activities instead of mechanical

measurement since MEMS can be utilized for the simultaneous measurement of force and displacement. The loading conditions and substrate can be identified in a simpler manner in MEMS, enabling comparison of experimental results with modelling.

The cell contraction forces are on the order of several tens of nanoNewtons. MEMS sensors can be used to measure forces in this range. Furthermore, the upper limit of the force that can be generated by a MEMS actuator can reach several hundreds of nanoNewtons. This makes it possible to stimulate cells in a force range that is not applicable with magnetic or optical tweezers and most AFM probes.

Regarding size scale, MEMS serve as a bridge between macro scale systems and micro/nano scale systems. There are numerous successful and well-established MEMS sensor and actuator designs available in the literature that enable on-chip stimulation and measurement without relying on bulky and complex external instrumentation. This approach is also advantageous in terms of measurement reliability due to the low noise. Moreover, most actuators and sensors have improved performance with reducing size scale. Electrostatic actuators, for instance, have higher sensitivity, better time response, and lower power consumption at smaller sizes.

2.2.2. Micromechanical tools

A review of micromechanical tools used in mechanical stimulation of cells and the characterization of cell mechanics and cell-substrate interactions is presented prior to reviewing MEMS. The micromechanical tools mentioned in this section are passive mechanical structures having springs of known stiffness, and the displacements of the springs are generally measured using optical microscopy. Motion is usually generated by an external actuator such as a piezoelectric crystal. The most commonly utilized micromechanical tools are micropost arrays, micromechanical probes, and microstretchers (Figure 2.3). These structures are produced using microfabrication technology, and their design is based on the range of force and displacement that is desired depending on the intended experiment. Measurement of force is carried out indirectly by measuring the displacements of springs with known stiffness.

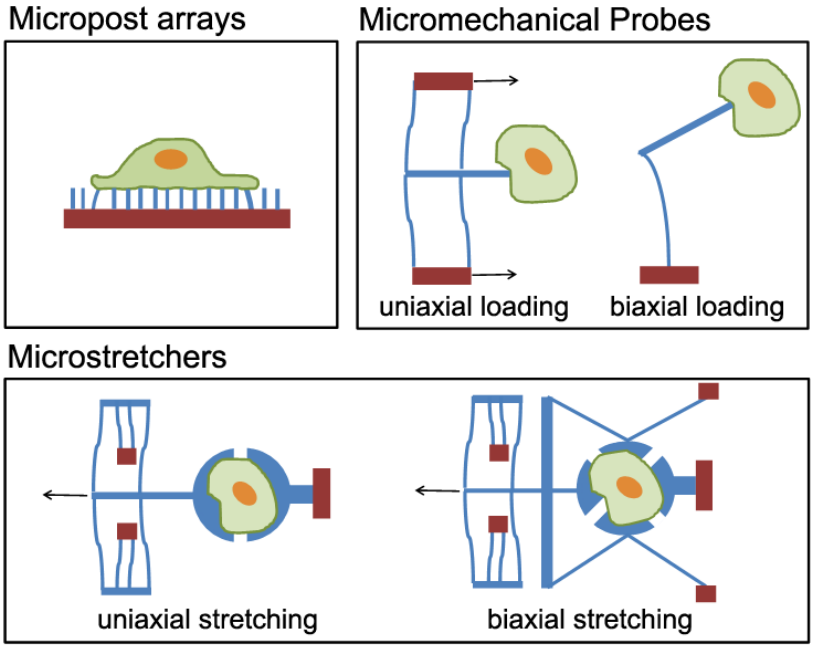

Figure 2.3: Micromechanical tools used in cell stimulation and characterization: Micropost arrays, micromechanical probes, and microstretchers.

Micropost arrays are generally fabricated using polymer materials having low stiffness, and they are used for the analysis of cell-substrate interactions. The cell is laid onto a substrate that comprises an array of microposts and the interaction forces between the cell and the substrate bend the microposts. The in-plane displacements of the micropost tips are measured using optical microscopy, and a map of the force field can be generated. The major advantage of this technique is the ability to perform measurements on multiple points on the cell. Micropost arrays have been used to give rise to several interesting findings. Roure *et al* [57] used epithelial cells and micropost (or micropillar) arrays and found that the cell-substrate interaction forces were largest at the edges of the cells. Sniadecki et al [53] used an elastomer micropost array with partially dispersed cobalt nanowires. This way, the posts with nanowire attachments could be actuated by an external magnetic field and the posts without nanowires could be used for sensing. This study revealed that focal adhesion size increases at the locations where a post applies force to the cell. The measurement resolution in the micropost array method depends on the resolution of optical microscopy imaging, thus enhancing microscopy imaging resolution is a key factor for high resolution measurement. One way to improve imaging resolution is to tag the micropost tips with fluorescent molecules. Reliable measurement in micropost array method also requires that the cells do not

spread along the length of the posts, *i.e.*, cell adhesion is limited to the post tips only. This is a key requirement since the calculation of traction forces from measured in-plane displacement of micropost tip rests on the assumption that cells interact with the substrate only at the post tips. The adhesion of cells to the micropost tips can be achieved by functionalizing the post tips with fibronectins using the microcontact method, but assuring that the fibronectin solution is not deposited on the sidewalls of the microposts remains a difficult task [58].

Probing cells with microfabricated mechanical probes is another commonly applied method in cell mechanics studies. In this method, a probe attached to a shuttle that is anchored by springs of known stiffness is used to apply force on a cell, similar to the AFM approach. Based on the mechanical design, uniaxial or biaxial loading is possible. A piezoelectric actuator is usually employed to manipulate the probe and apply forces on the cell. When the probe makes contact with the cell and applies a force on it, the reaction force generates displacements of the springs that the probe is attached to. The displacement is measured by optical microscopy and the applied force is computed from the measured displacement data and the known stiffness of the springs. When using this method, reliable force measurement requires highly precise and accurate characterization of spring stiffness. The stiffness measurement is usually carried out using AFM prior to the cell experiments. Although this method is similar to probing cells with AFM cantilevers, the relative simplicity and miniature size of the instrumentation allows optical microscopy imaging of the cell whereas the AFM instrumentation may block the view of the sample cell. Yang and Saif [59] used this method to analyze the response of actin networks in fibroblasts to applied force.

Microstretcher devices generally comprise a mechanical platform for cell adhesion and various springs of known stiffness anchoring the cell adhesion sites. The adherent cell is stretched by an external actuator and the forces are determined from the measured displacements of springs and their known stiffness values. Serrel *et al* [60] developed a microfabricated uniaxial stretcher device and examined the force response of single fibroblasts. Lin *et al* [61] analyzed the contraction forces generated by living heart muscle cells. In another study by Lin *et al* [62] a microfabricated structure was used to apply tension on groups of neural stem cells and the effect of mechanical tension on the cerebral cortex neurogenesis was investigated.

The performances of micromechanical tools that rely on external actuators for manipulation and optical microscopy for measurement are on a similar level with the common cell stimulation techniques previously described (micropipette aspiration, AFM, magnetic

tweezers, etc.). Especially at the single cell level, the force levels are congruent with the force range of the micromechanical tools (Figure 2.4). Microstretchers also offer the advantage of reliable comparison of experimental data with modelling studies due to the convenient definition of the boundary conditions. On the other hand, the reliance of the micromechanical tools on external actuators and displacement measurement by optical microscopy brings about several disadvantages:

i) These techniques cannot reach the resolution of AFM or optical tweezers which can be used to stimulate single molecules.

ii) Simultaneous implementation of several stimulation units is not practical

iii) The use of imaging equipment for the measurement of spring displacement makes it impractical to optimize the microscopy method for the imaging of cells and cellular processes.

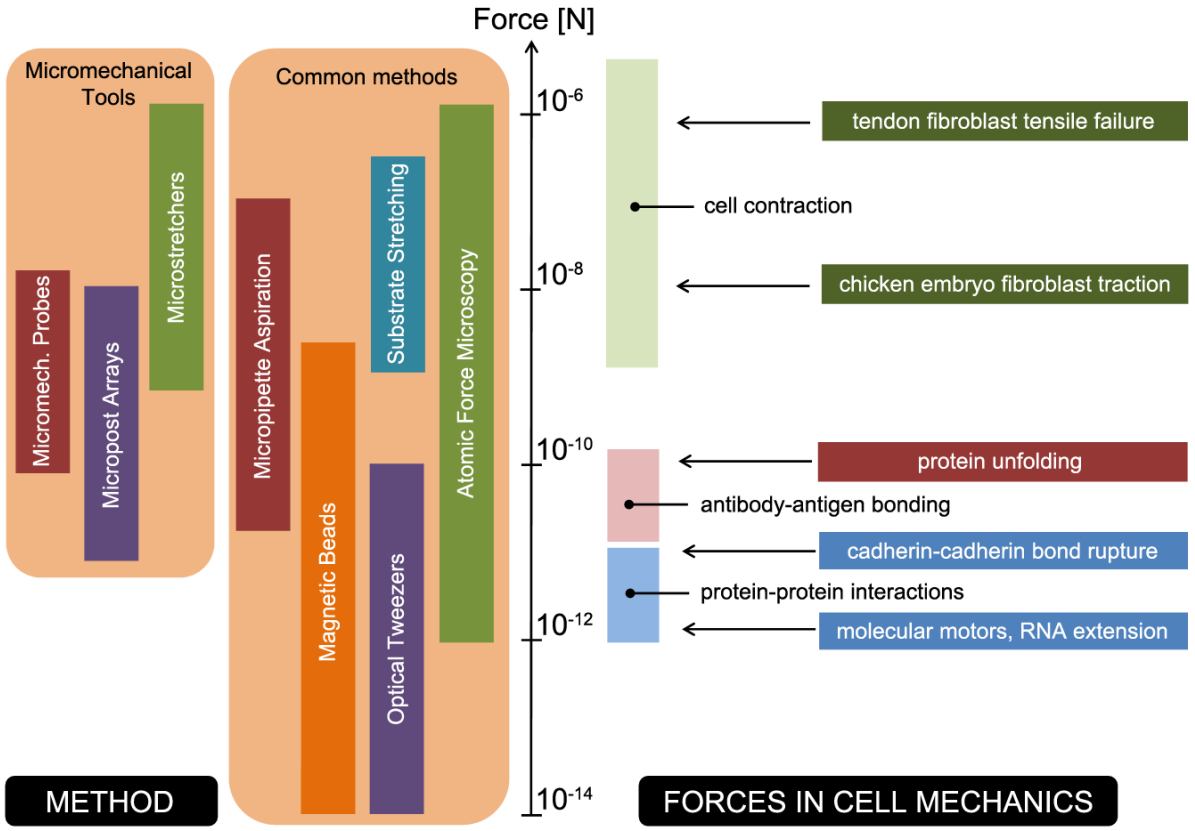

Figure 2.4: A comparison of the force ranges of various micromechanical cell stimulation and measurement methods with the common methods for mechanical stimulation of cells, and the corresponding biological events [55, 63].

2.2.3. MEMS devices for cell mechanics studies

There have been a limited number of studies reporting MEMS test platforms for cell mechanics having on-chip actuators. An example is a mechanical test platform designed by Eppell *et al* [64], utilizing on-chip electrostatic actuator designed for tensile testing of collagen fibrils. In this study, the sample is attached at two ends to rigid pads and tension is applied by an electrostatic actuator while springs maintain uniaxial loading conditions. The force generated by the electrostatic actuator is calibrated by obtaining voltage-displacement curves without the sample and using the stiffness values of the springs. The displacement is measured using an on-chip Vernier gage and optical microscopy. The device is used to carry out monotonic tension tests and fatigue tests on collagen fibrils. Scuor *et al* [65] designed a MEMS device utilizing on-chip electrostatic comb drive actuators for the biaxial stretching of single live cells. It is also possible to integrate on-chip capacitive displacement sensors with the MEMS based devices, enabling the mechanical characterization of cells within a wide force range (10^{-8} – 10^{-4} N) [66].

The utilization of MEMS actuators and sensors eliminates the reliance on external equipment for the mechanical stimulation of cells and measurement of cell's force response. This reduces measurement noise and improves resolution. Li *et al* [67] demonstrated chemisorption measurements using piezoresistive nano-cantilevers at very high frequencies with a mass resolution of less than 1 attogram. MEMS devices with on-chip actuators and sensors allow the optical imaging methods to be used solely for the examination of biological activities. Furthermore, the level of miniaturization allows for the design and fabrication of devices capable of carrying out measurements at multiple locations simultaneously.

MEMS actuators allow for displacement-controlled or force-controlled experiments. A displacement-controlled actuator, for instance, generates a prescribed displacement regardless of the reaction forces. A device integrating a displacement-controlled actuator and a force sensor is an ideal platform for the determination of nonlinearities such as softening or bond fracture [55].

The microfabrication technology that is used for the realization of MEMS devices enables fabrication of devices specifically designed for cell mechanics studies. Using microfabricated structures, cell response can be evaluated on different substrates having three dimensional (3D) surface topographies such as trenches and wells fabricated specifically to

hold a single cell [68]. It is also possible to realize actuators and sensors that are capable of operating in aqueous environments [69, 70].

Chapter 3

UNIAXIAL TENSILE STRETCHER AND FLUORESCENT MICROSCOPY

Studies have emerged in the past few decades to investigate the effects of the mechanics of cell-substrate interactions on the morphology and behavior of biological cells. In these studies, cells are studied in engineered conditions where the mechanical state of the *in vivo* environment is simulated. A common approach is to plant the cells on a flexible membrane, deform the cells indirectly by stretching the membrane in a tensile stretcher device, and image the cells by light microscopy. Hayakawa *et al* [71] utilized a stretcher device to examine the effect of cyclic stretching on the rearrangement of cytoskeletal elements and cell reorientation. They placed rat vascular smooth muscle cells on a silicone polymer membrane, deformed the cells by stretching the silicone membrane, and observed that cells that were randomly oriented on a petri dish were aligned at 50 to 80 degrees with the direction of stretching when a cyclic stretch was applied. Naruse *et al* [72] used a tensile stretcher setup to investigate the molecular mechanism of cell reorientation as a response to mechanical stretch. They showed that cells align perpendicular to the stretch axis when the intracellular calcium ion concentration increases as stretch-activated calcium ion channels are activated due to cyclic stretching. Yost *et al* [73] developed a uniaxial stretcher device and demonstrated that mechanical stretching affects the production of β_1-integrin by neonatal rat cardiac fibroblasts. Bonakdar *et al* [74] utilized a uniaxial stretcher and fluorescent microscopy (Figure 3.1) to investigate the effect of cyclic stretching on the viability of myoblasts with mutations in the desmin gene. The cells were adhered onto a PDMS membrane and stretched while fluorescent microscopy was used to count the numbers of live and dead cells.

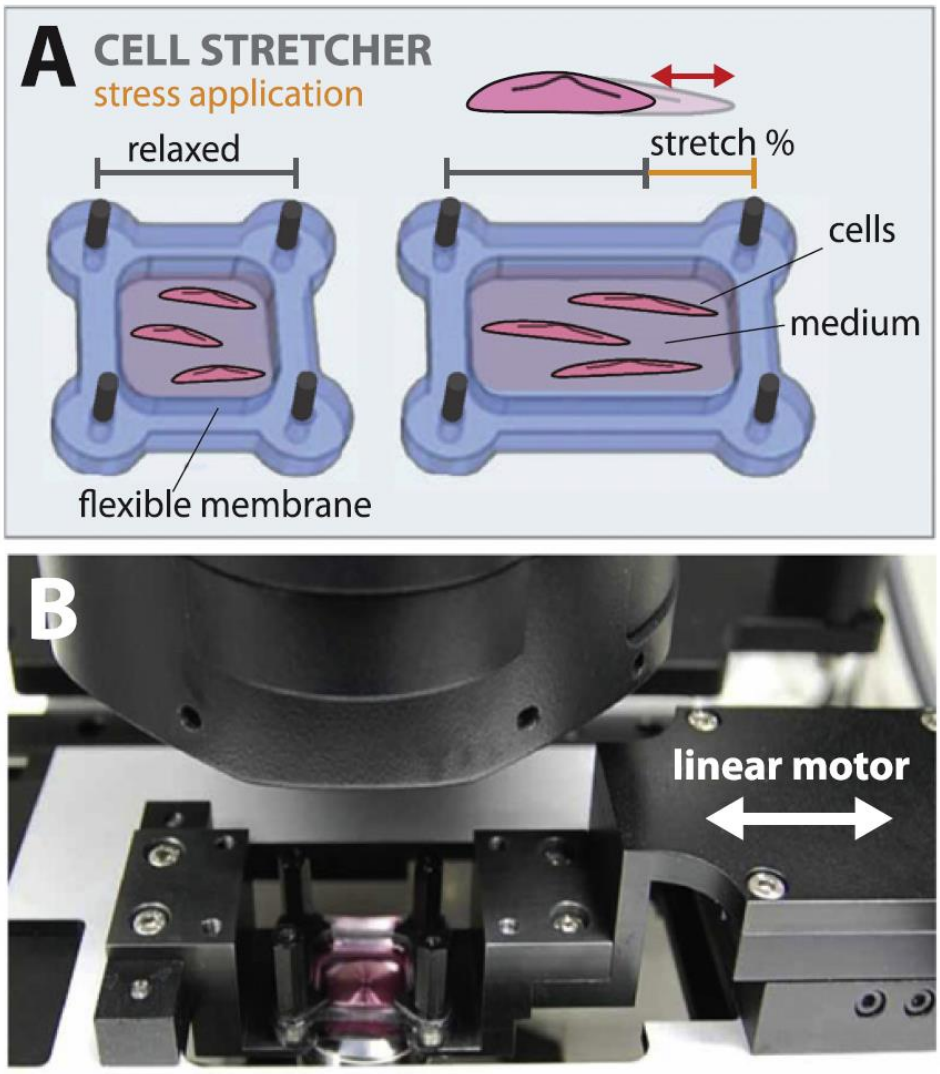

Figure 3.1: Uniaxial stretcher and fluorescent microscopy system used by Bonakdar *et al* [74].

These studies help answer questions regarding the effects of the extracellular mechanical environment on cell morphology and behavior. However, the simulated mechanical environment is often poorly characterized. A commonly employed measure of the externally applied mechanical deformation is the percentage stretch which is calculated as the ratio of cross-head displacement to the original length of the specimen, *i.e.*, the cross-head strain. The cross-head strain is a scalar value that corresponds to the average longitudinal strain. It contains no information regarding the lateral or shear components of strain or their spatial distribution. A detailed analysis of the applied mechanical deformation with the ability to distinctly measure the longitudinal, lateral, and shear components of the applied in-plane strain is required to investigate the effect of these different strain components on cell morphology and behavior. Moreover, the strain components may have a non-uniform spatial

distribution if the substrate has heterogeneous mechanical properties as some biomaterials do, or if the specimen has non-uniform cross-sectional area. In the case of non-uniformly distributed strain, the local strain in the vicinity of the cells that are analyzed may be different than the cross-head strain since the latter is an average value. Measurement of the spatial distribution of strain is therefore another requirement for accuracy when the in-plane strain components have non-uniform distribution.

The instrumentation and technique presented in this study can be used to measure both the spatial distribution and the time evolution of local in-plane strain components with high resolution. The method we employed is based on the integration of a uniaxial tensile stretcher device with fluorescent microscopy. The role of the tensile stretcher is to deform the specimen which is a transparent polymer membrane with fluorescent beads embedded in it. Fluorescent microscopy is utilized to record images of the specimen during stretching. The trajectories of the fluorescent beads are identified by implementing image processing on consecutive frames. We assume the displacements of the fluorescent beads are the result of specimen deformation only, *i.e.*, the beads adhere perfectly to the specimen. The spatiotemporal distribution of longitudinal, lateral, and shear components of in-plane strain are then calculated from the displacements of the beads. In addition to the ability to measure the different strain components separately; this method also has the advantage of performing strain measurements without making physical contact with the specimen. Non-contact strain measurement methods are more reliable for experiments on soft materials compared to contact measurement methods such as clip-on extensometers and strain-gages [75]. Moreover, the contact measurement methods are often incapable of measuring the lateral and/or shear strain components.

An alternative method for non-contact measurement of strain components is digital image correlation (DIC) [76]. In this method, a speckle pattern is generated on the surface of the specimen by applying spray paint, images of the speckle pattern before and after deformation (Figure 3.2) are taken with a camera, and image processing techniques are used to calculate the 2D displacement field, and subsequently, the strain components. Within the past few decades, numerous authors have reported successful utilization of the DIC method for the measurement of in-plane strain components and Poisson's ratio. Zhang *et al* [77] used the DIC method to measure the heterogeneous spatial distribution of in-plane strain components in aluminum specimens with holes. Tscharnuter *et al* [78] used DIC to measure the time-evolution of Poisson's ratio of polypropylene specimens with different loading

histories. Pritchard *et al* [79] used DIC to measure the spatial distribution and time evolution of in-plane strain components and Poisson's ratio for a variety of soft materials. Although the DIC method is widely and successfully applied to measure in-plane strain, it also has several shortcomings. Obtaining the displacement data from the sequence of images of the speckle pattern is a complex and computationally expensive process. The speckle pattern is a major factor that affects the accuracy and resolution of the displacement measurement. The speckle size distribution and the pixel subset size have been shown to influence displacement measurement accuracy [80]. Furthermore, when calculating the strain values from displacement field data, systematic errors arise that depend on various factors including data smoothing, interpolation, and subset size [81].

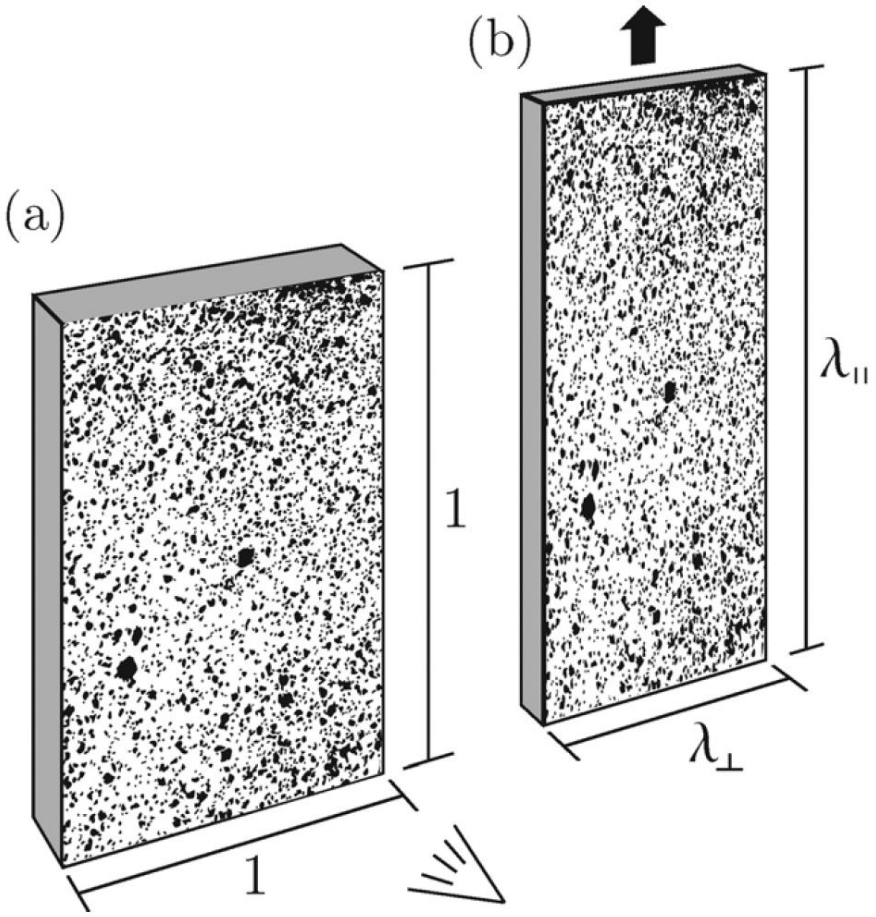

Figure 3.2: In DIC, 2D strain field is measured by imaging the speckle pattern before (a) and after (b) deformation and using image correlation software to track displacements [79].

The method presented in this study involves tracking the displacements of embedded fluorescent beads to measure in-plane strain. The main reason for using this method instead of the DIC method is the convenience of using fluorescent microscopy – an already available and well established technique for imaging live cells – to image both the specimen deformation and the biological cell. This way, the tensile stretcher and fluorescent microscopy assemblies that were previously utilized for bio-mechano-transduction studies [71-74] can be used to measure local in-plane strain components with the sole addition of embedding fluorescent beads into the polymer specimens. Moreover, imaging the specimen deformation and biological cell can be done simultaneously if dual-color imaging is used. The simultaneous imaging of the cell and the fluorescent beads in the vicinity of the cell enables establishing more accurate correlations between applied deformation and cell response. Another reason for selecting the present method over DIC is the computational simplicity. The displacement data that is used for the calculation of in-plane strain is obtained by tracking the positions of fluorescent beads which are distinct points distributed randomly in the image plane. No finite element grid meshing or interpolation was implemented. The accuracy and spatial resolution then depends on the size and spatial frequency of the beads. High spatial resolution can be obtained using fluorescent beads having diameters down to the sub-micrometer range, which are commercially available and have been utilized in the past in similar studies involving the measurement of 2D displacement and traction fields [82, 83].

The presented method was demonstrated by measuring the local strain values at the center regions of two different specimens, one having a rectangular geometry with uniform cross-section, and the second having a dumbbell geometry. Both specimens were prepared using PDMS elastomer. Finite element analysis was performed for both specimen geometries to determine the expected distribution of strain. For the rectangular specimen, strain is expected to be distributed uniformly. The dumbbell specimen was chosen for comparison because finite element analysis showed a non-uniform strain distribution for this specimen geometry. Much of the deformation is confined to the narrow neck region and the local strain at the neck region is larger than the average cross-head strain. To demonstrate the capability and the value of the present method to measure local in-plane strain, the longitudinal component of measured local strain was compared with the applied cross-head strain for the two different specimen geometries.

3.1. Experimental Setup and Operation

3.1.1. Design of Uniaxial Tensile Stretcher

The overall mechanical design of the uniaxial tensile stretcher was laid out with focus on flexibility, easy customization, and compatibility with inverted microscope setups. The stretcher (Figure 3.3) utilizes a linear actuator that applies tensile load, and a load cell to measure the tension in the specimen. The linear actuator is a stepper motor with a lead screw as the motor shaft. The specimen is gripped tightly at two ends by custom-made aluminum grips. One of the grips is movable while the other is fixed. The motion of the movable grip is actuated by the stepper motor and a linear guide rail system is used to achieve stable linear motion of the grip. The movable grip is attached to the motor shaft via a mounting piece and the fixed grip is attached to the load cell via another mounting piece. The grip mounting pieces are designed for permanent use while the grips themselves can easily be changed. Hence, a variety of different grips can be used with samples of different sizes and shapes. The linear actuator, load cell, and the grips are assembled onto two pieces of T-slotted aluminum extrusion that make up the backbone of the stretcher and enable easy mounting and customization. The entire assembly can be mounted onto most inverted microscope stages using simple L-shaped brackets that can be custom made for the microscope stage and attached to the t-slotted extrusion on the stretcher assembly.

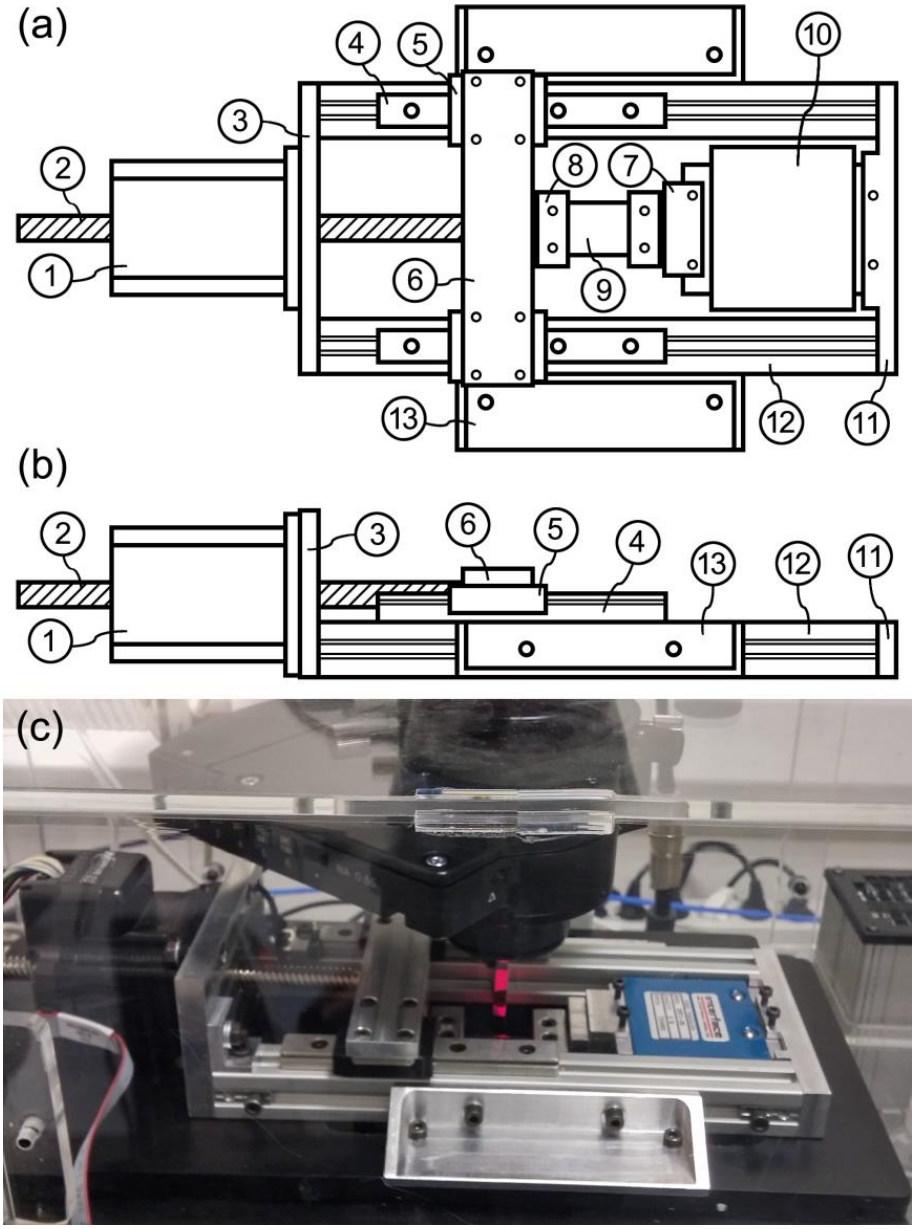

Figure 3.3: Schematic top (a) and front (b) views of the stretcher illustrating the basic components: The stepper motor (1) and lead screw (2), motor mounting plate (3), linear guide rails (4) and carts (5), movable grip mounting piece (6), fixed grip mounting piece (7), grips (8), specimen (9), load cell (10), load cell mounting plate (11), t-slotted aluminum extrusions (12), and brackets for mounting the stretcher onto a microscope stage (13). View of the tensile stretcher mechanism mounted onto the stage of an inverted microscope (c).

3.1.2. System Characterization

The uniaxial tensile stretcher is operated and controlled using a PC and the LabVIEW development environment. The specimen is stretched by the linear stepper motor, and tension is measured by a load cell. Both the stepper motor and the load cell are powered by a DC power supply and the appropriate electrical connections are made between the motor, load cell, and the PC. A block diagram of the stretcher system is shown in Figure 3.4a, detailing the electrical connections between the power supply, stepper motor, load cell, and the PC.

The linear stepper actuator (IMS MDrive23™ Series) has an integrated driver and a programmable controller with two communication interfaces; a general purpose digital I/O port and an RS-485 communication port. The RS-485 communication port was connected to the PC via a communication converter and was used to assign functions to the general purpose I/O channels for driving the motor. The general purpose I/O channels were then connected to the PC via a shielded connector block (NI BNC-2110) and a DAQ card (NI PCI-6036E) and the motor was controlled through this interface using a LabVIEW subroutine.

The tension in the specimen was measured by a load cell (Interface SMT1-5N) which consists of strain gauges configured as a Wheatstone bridge. A DC power supply was used to provide 10V excitation to the load cell and the output signal was filtered and amplified using a custom signal conditioner circuit. The conditioned output was then connected to the PC through the shielded connector block and DAQ card, and the same LabVIEW subroutine that controls the linear stepper motor was used to record the load cell output.

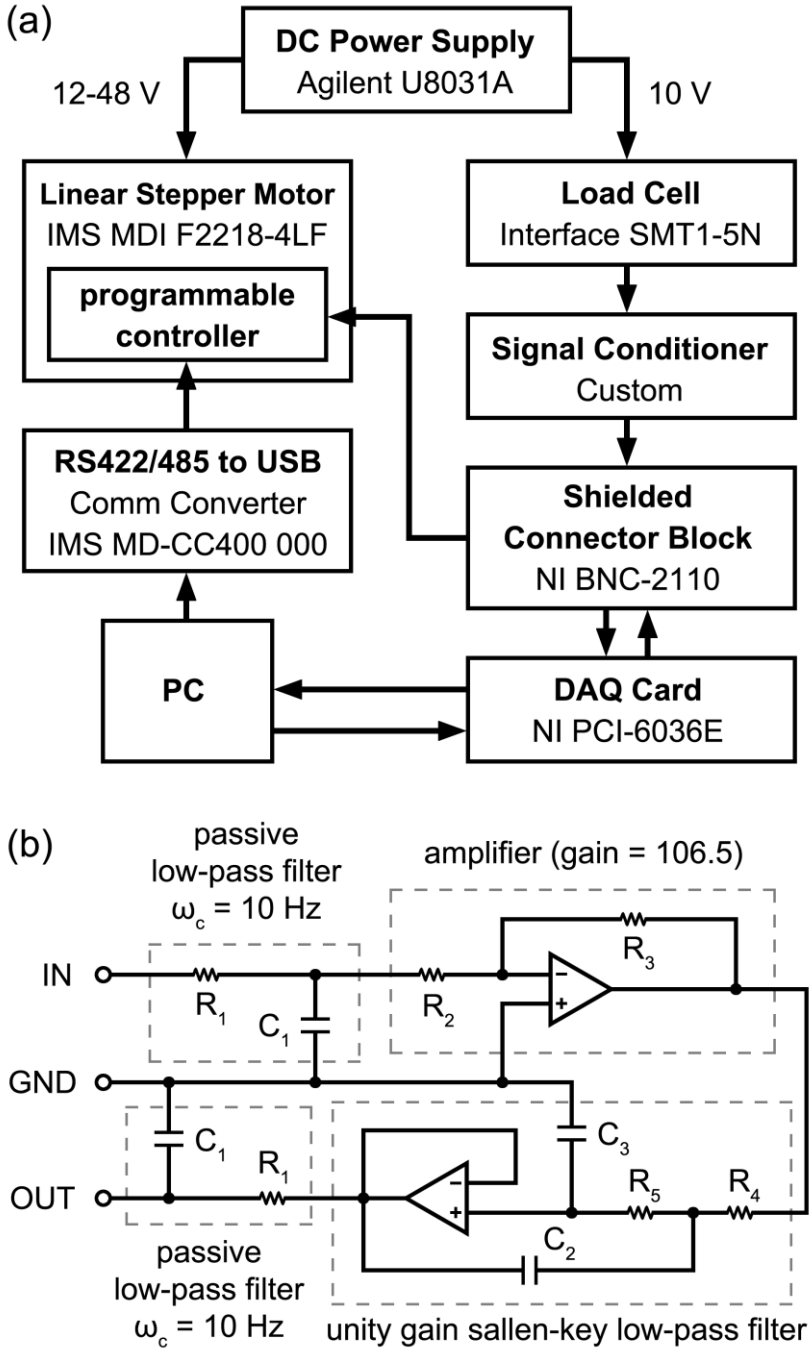

Figure 3.4: Block diagram of the stretcher system (a) and schematic of the custom built signal conditioner circuit for filtering and amplifying load cell readout signal (b).

Due to the lack of an encoder or a displacement sensor to provide displacement feedback for actuation, the linear actuator was controlled in an open loop configuration. This requires meticulous characterization of the actuator mechanism for the sake of displacement data accuracy. The linear stepper actuator uses a lead screw to convert the rotary motion of the rotor to linear motion. The motor datasheet specifies that the stepper motor has a step

angle of 1.8° and the lead screw travels 50.8μm for one full step of the stepper motor. The integrated driver is capable of dividing the full 1.8° step angle into 256 bits or "microsteps" by modulating the current input to the electromagnets in the stator, resulting in a gain value of 0.198 μm/microstep. We attached a scale bar onto the movable grip and measured the actual displacement generated by the motor by taking images of the scale bar under a microscope and implementing image processing. A linear relationship was observed between the measured displacement (in μm) and the motor command (in number of microsteps) with a coefficient of determination of $R^2 = 0.9999$, and a gain value of 0.196 μm/microstep which is in close proximity of the value calculated from the datasheet.

The load cell was also calibrated before experimentation. It has a load capacity of 5N and the rated output value specified in the calibration certification is 2.10946 mV/V. This means that for 10V DC excitation, and an applied load of 5N, the voltage output of the load cell should be 21.0946 mV resulting in a sensitivity value of 4.2189 mV/N. To enhance measurement resolution, the raw output signal of the load cell was amplified and filtered using a custom built signal conditioning circuit (Figure 3.4b). The signal conditioning circuit consists of two passive RC low-pass filters, an operational amplifier with gain value of 106.50, and a unity gain sallen-key low-pass filter. The load cell was calibrated using precise weights ranging from 1 gram to 20 grams. The output voltage of the signal conditioner circuit was measured and recorded for each different load, and the resulting calibration curve is shown in Figure 3.5. There is a highly linear relationship between the measured output voltage and applied load with a coefficient of determination value of $R^2 = 1.0000$, and a sensitivity of 0.4339 V/N. A sensitivity value of 0.4493 V/N was obtained by multiplying the raw output sensitivity calculated from the calibration certification and the amplifier gain of our custom built signal conditioner circuit. This value is in agreement of the results of our calibration.

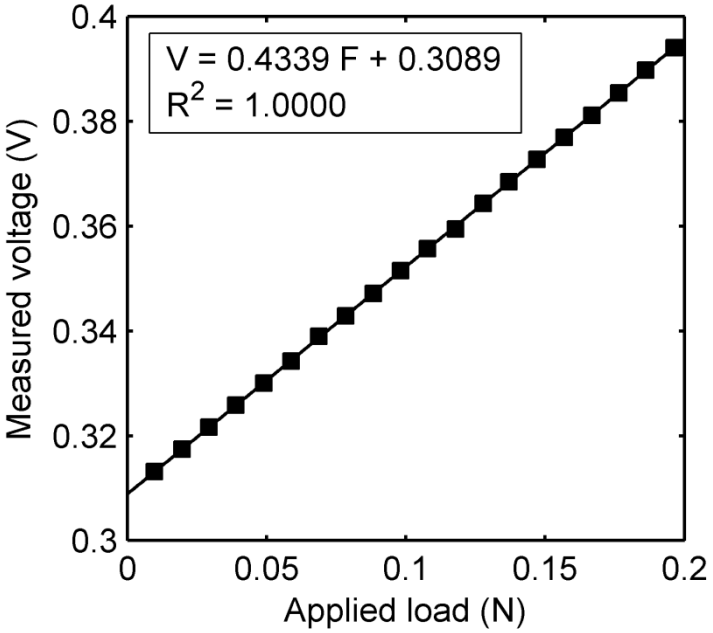

Figure 3.5: Load cell calibration curve obtained using the output of the signal conditioner circuit.

3.1.3. Fluorescent Microscopy Imaging

After the stretcher was assembled and all calibrations were done, the stretcher was integrated to Olympus Xi81 inverted microscope (Figure 3.6a). The images were recorded with an Andor Ixon3-897 reinforced by a quantitative digital camera technology called Electron Multiplying Charge Coupled Device, EMCCD. For magnification we used a 10x air objective. The integrated system enables us to record both white light and fluorescence images during the tensile testing.

The maximum tracking distance of any bead embedded in the specimen across the frame is 819.2 μm due to small field of view of the 10x objective and pixel size of the camera. Since the beads that we are tracing move towards the pulling direction, we cannot trace them after a while. To overcome this problem, we used the motorized the stage of the microscope and synchronized it with the stretcher to keep the beads in frame while the specimen is strained up to 150% -200%. Two parameters need to be taken into account in synchronization of the stage with the stretcher: the center point of the specimen and the relative velocities of the stage and the stretcher. The center point is located after the specimen is placed between the grips and the stretcher is mounted on the stage. The microscope we used provides us the stage position in x, y, and z directions. First, we got the specimen in focus by moving stage in

z direction. Then we scanned the specimen's surface from fixed end to the free end and we recorded the y positions of the end points, y_1 and y_2. Then the y coordinate of the center point is

$$y_0 = (y_2 + y_2)/2 \tag{3.1}$$

Then we moved the stage at y_0 and we scanned the surface in x direction to get edge coordinates. We moved the stage until we got to the edges of the specimen and recorded the x positions of the edges, x_1 and x_2. Then the x coordinate of the center point can be calculated as

$$x_0 = (x_1 + x_2)/2 \tag{3.2}$$

The center point of the specimen is (x_0, y_0) around which we investigate the local strains. When the specimen is stretched with a velocity of ν, the center point moves with a velocity of ν/2 since one end of this specimen is fixed. For compensation, the stage velocity should be - ν/2. For instance, when the specimen is pulled with a velocity of 200 μm/s, the center point moves with a velocity of 100 μm/s and eventually leaves the field of view. The stage needs to move with a velocity of -100 μm/s to compensate for the motion of the center point. Figure 3.6b shows the trajectories of the beads when the stage does not move. After a certain amount of stretching, all the beads that were originally at the center disappear from the field of view. To compensate for this motion, the stage was moved with the same velocity of the center point in reverse direction, thus we were able to track the reference beads for the entire duration of the experiment. A comparison of stretching without stage control and stretching with stage control to compensate for the motion of the beads is shown in Figure 3.6b and Figure 3.6c. We applied the same strain in both cases and recorded trajectories of the beads. At 8% cross-head strain, for the case of no stage control, 70 of the original 107 beads remained in the field of view (Figure 3.6b), *i.e.,* 37 beads moved out of the field of view, whereas for the case of stretching with stage control, all 107 beads remained in the field of view (Figure 3.6c).

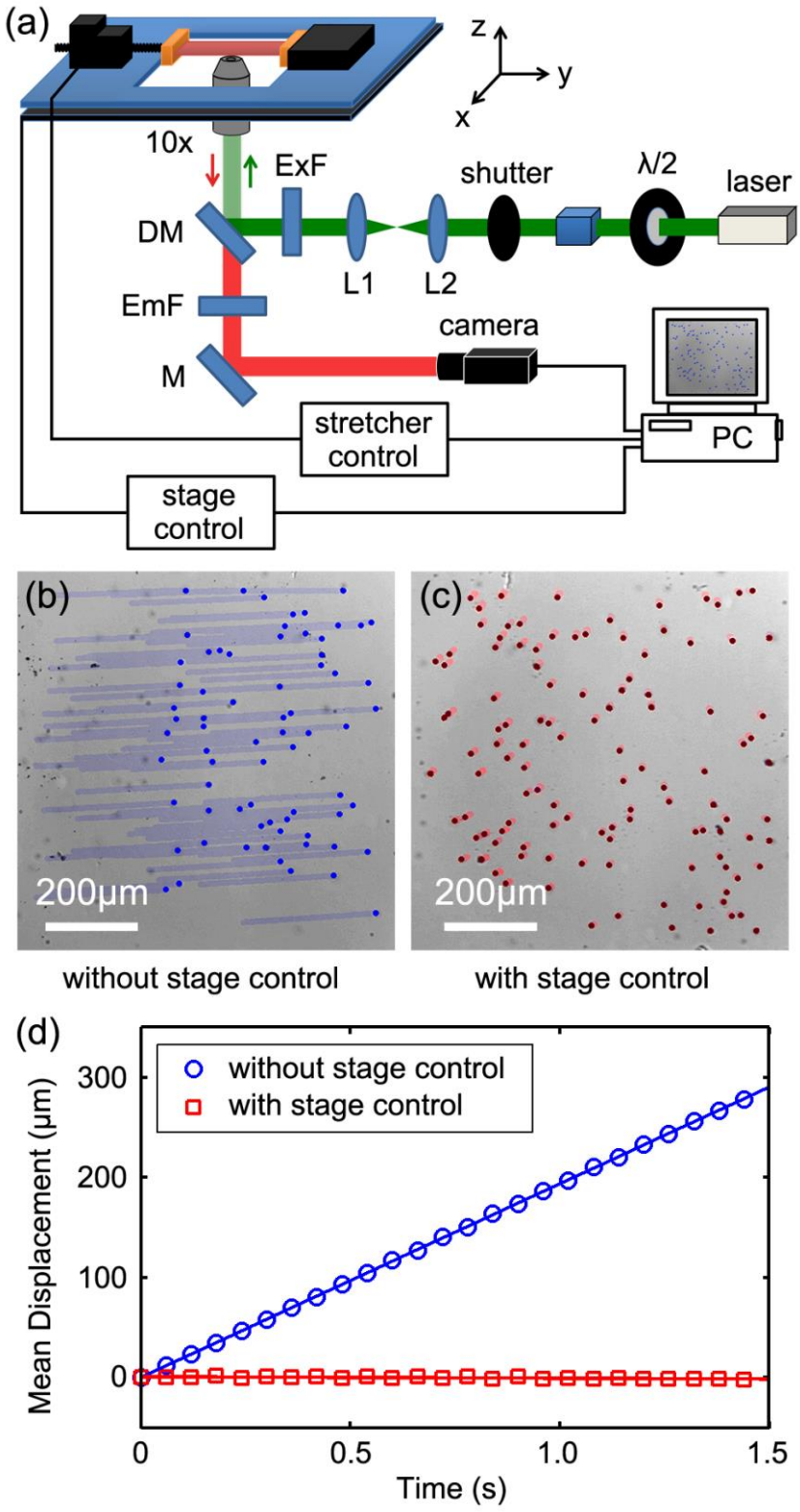

Figure 3.6: Schematic representation of optical setup (a). Trajectories of beads recorded under white light illumination without stage control (b) and with stage control (c). Comparison of the mean displacement of beads with and without stage control (d).

3.2. Sample Preperation

PDMS is a very useful substrate due to its rapid polymerization and compatibility with multiple substrates at various conditions. In addition to these properties, having simple and low-cost fabrication, optical transparency, chemical inertness, and non-toxicity encouraged us to use PDMS as a specimen material [84]. The manufacturing of PDMS specimen is done using the Sylgard 184 silicon elastomer kit purchased from Dow Corning. The kit comes with a precursor (pre-polymer) and a curing agent. Precursor and curing agent are combined at a weight ratio of 10:1 in a weighing boat. Then we add red color dyed polystyrene microspheres (5 μm diameter) purchased from Phosphorex Inc. to the mixture of pre-polymer and curing agent. Having fluorescent microspheres as ingredient enables real time particle tracking by fluorescent microscopy. The compound is spun with an average spin rate to make sure that we have a homogeneous mixture.

Two different specimens were prepared for the experiments reported in this study. One specimen has a rectangular geometry with a gage length of 30 mm, and a width of 20 mm. This specimen was prepared by pouring the pre-polymer, curing agent, and fluorescent bead mixture into a petri dish and cutting the desired shape after polymerization using a scalpel. The second specimen geometry has a dumbbell shape with dimensions that are one-third the dimensions specified in ASTM D412-C standard. The narrow neck section of the dumbbell specimens has a length of 11 mm and a width of 2 mm. The dumbbell specimens were prepared using an acrylic mold that was made using a CNC laser cutter. . Since all processes prior to pouring the mixture into the mold, especially mixing, generate air bubbles in the mixture, an additional vacuum degassing is strongly suggested after mixture transferring [85], in order to clear the air bubbles. Once mixture gets its final shape in the mold, we let it polymerize at room temperature for at least 48 hours. Room temperature curing is preferred in this particular application because the fluorescent microspheres lose their fluorescence properties irreversibly if they are subjected to high temperatures – which we observed with the samples cured at 150°C for 15 minutes.

3.3. Results and Discussion

3.3.1. Tracking Fluorescent Microspheres

The fluorescent microspheres were tracked using MATLAB. The fluorescent bead tracking algorithm consists of three main steps. The first step is to call the video that is recorded during microscopy imaging by the camera into the MATLAB workspace frame by frame. The next step is to locate the beads on the image plane. This is done by applying a band-pass filter on the image. Once the beads are located at each frame, the third step is to track individual beads in consequent frames. In other words, the coordinates of the same bead are identified at each frame. Figure 3.7a and Figure 3.7b show the trajectories of the beads that were identified using our tracking algorithm for bright-field image and fluorescent image, respectively.

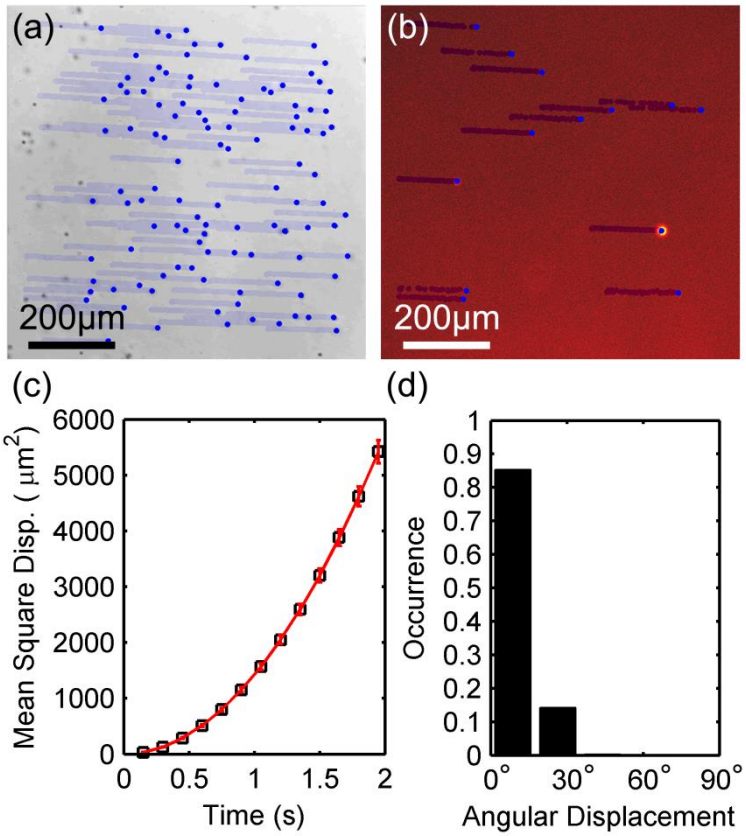

Figure 3.7: Tracking the bead movement by random walk analysis. Trajectories of beads recorded under white light illumination (a). Trajectories of beads recorded by fluorescent imaging (b). Mean square displacement of the beads versus time (c). Histogram of the angular displacement of beads (d).

Once the trajectories of the beads were recorded, we also calculated the mean square displacement (Figure 3.7c) and angular displacement (Figure 3.7d) values of the beads. The time evolution of average mean square displacement follows a parabolic trend, which suggests an active driving force for the motion of the beads. This result is in accordance with our expectations since there actually is an active driving force which is the applied tensile strain. The distribution of the angular displacement of the beads, on the other hand, shows that most beads move along the horizontal direction. The angular displacement shown in Figure 3.7d is the angle that the trajectory curve makes with the horizontal axis. This finding illustrates that there is very little lateral motion of the beads, which is as expected under uniaxial loading. This result is also an indication that the beads adhere well to the substrate since the motion of the beads is not random but directed along the stretch axis.

3.3.2. Calculation of Local 2D In-plane Strain Components

Fluorescent microscopy and subsequent image processing provide the positions of embedded fluorescent beads as a function of time as the specimen deforms. Treating the center points of the embedded fluorescent beads as material points, the motion of the deforming specimen is described by

$$\boldsymbol{x} = \boldsymbol{\phi}(\boldsymbol{X}, t) \tag{3.3}$$

where $\boldsymbol{X}$ denotes the initial positions of the material points, and as the specimen deforms the positions of the same material points at time t are given by $\boldsymbol{x}$. Once the positions of the fluorescent beads are obtained from microscopy and image processing, the *displacement vector* can be computed as

$$\boldsymbol{u}(\boldsymbol{X}, t) = \boldsymbol{\phi}(\boldsymbol{X}, t) - \boldsymbol{X}. \tag{3.4}$$

To calculate the strain tensor, first the *displacement gradient tensor* is defined as

$$\nabla \boldsymbol{u}_{iK} = \frac{\partial \boldsymbol{u}_i}{\partial \boldsymbol{X}_K} \tag{3.5}$$

then the *deformation gradient tensor* is defined in terms of the displacement gradient tensor as

$$\boldsymbol{F} = \nabla \boldsymbol{u} + \boldsymbol{I} \tag{3.6}$$

and lastly, the *right Caucy-Green deformation tensor* is defined as

$$\boldsymbol{C} = \boldsymbol{F}^T \boldsymbol{F} \tag{3.7}$$

In formulating the strain tensor, the right Cauchy-Green deformation tensor is used instead of the deformation gradient tensor to ensure that the computed strain is decoupled from rigid body motion.

$$\boldsymbol{E} = \frac{1}{2}(\boldsymbol{C} - \boldsymbol{I}) \tag{3.8}$$

In Equation 3.8, $\boldsymbol{E}$ is the *Green–Saint-Venant strain tensor* which is the most appropriate strain definition for the purposes of this study because the tensile stretcher is capable of stretching the PDMS samples to strain values exceeding 150% and the Green–Saint-Venant strain tensor formulation is convenient for large deformation mechanics [86]. Moreover, this strain definition is also an appropriate choice for the comparison of measured local strain and applied cross-head strain since both are engineering strains. In 2D Euclidian space, the strain tensor $\boldsymbol{E}$ in Equation 3.8 can be expressed in component form as

$$\boldsymbol{E} = \begin{bmatrix} \varepsilon_{xx} & \varepsilon_{xy} \\ \varepsilon_{yx} & \varepsilon_{yy} \end{bmatrix} \tag{3.9}$$

where the scalar components ε_{xx}, ε_{yy}, and ε_{xy} which is equal to ε_{yx} are the longitudinal normal, lateral normal, and the shear components of strain.

The in-plane strain components were computed for a PDMS specimen of rectangular geometry that was stretched up to 50% longitudinal strain. Time evolution of strain components is shown in Figure 3.8. The magnitudes of longitudinal and lateral strain components increase linearly with time since a constant strain rate was applied during stretching. The magnitude of shear component of strain remains approximately zero which is as expected in uniaxial loading conditions.

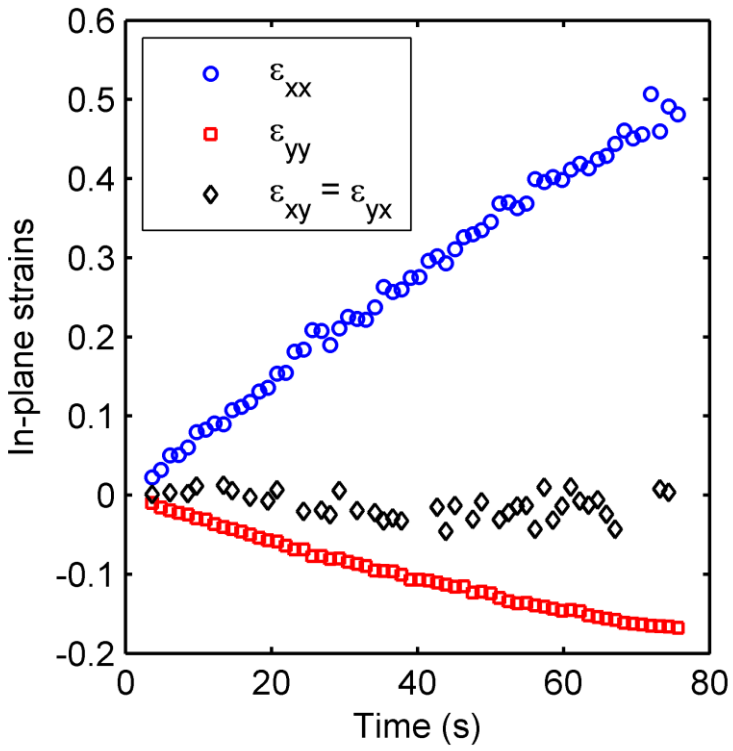

Figure 3.8: Time evolution of local in plane strain components.

In addition to the time evolution of strain, test results also provide a comparison between the cross-head strain and local strain. During stretching of the PDMS specimen, the displacement generated by the linear stepper motor was recorded in LabVIEW. Hence, both the initial length of the specimen and the displacement of the moving grip are known at any time during the experiment. Assuming the displacement generated by the linear stepper motor is equal to the elongation of the specimen – *i.e.*, there is no slippage at the grips – the cross-head strain can be calculated as the ratio of elongation to initial length. Cross-head and local strain values were compared for rectangular and dumbbell shaped specimens. Figure 3.9a shows the comparison of cross-head strain and longitudinal component of measured local strain for a rectangular specimen. Within the range of strain applied in this experiment, the cross-head and local strains overlap with each other indicating a uniform distribution of strain.

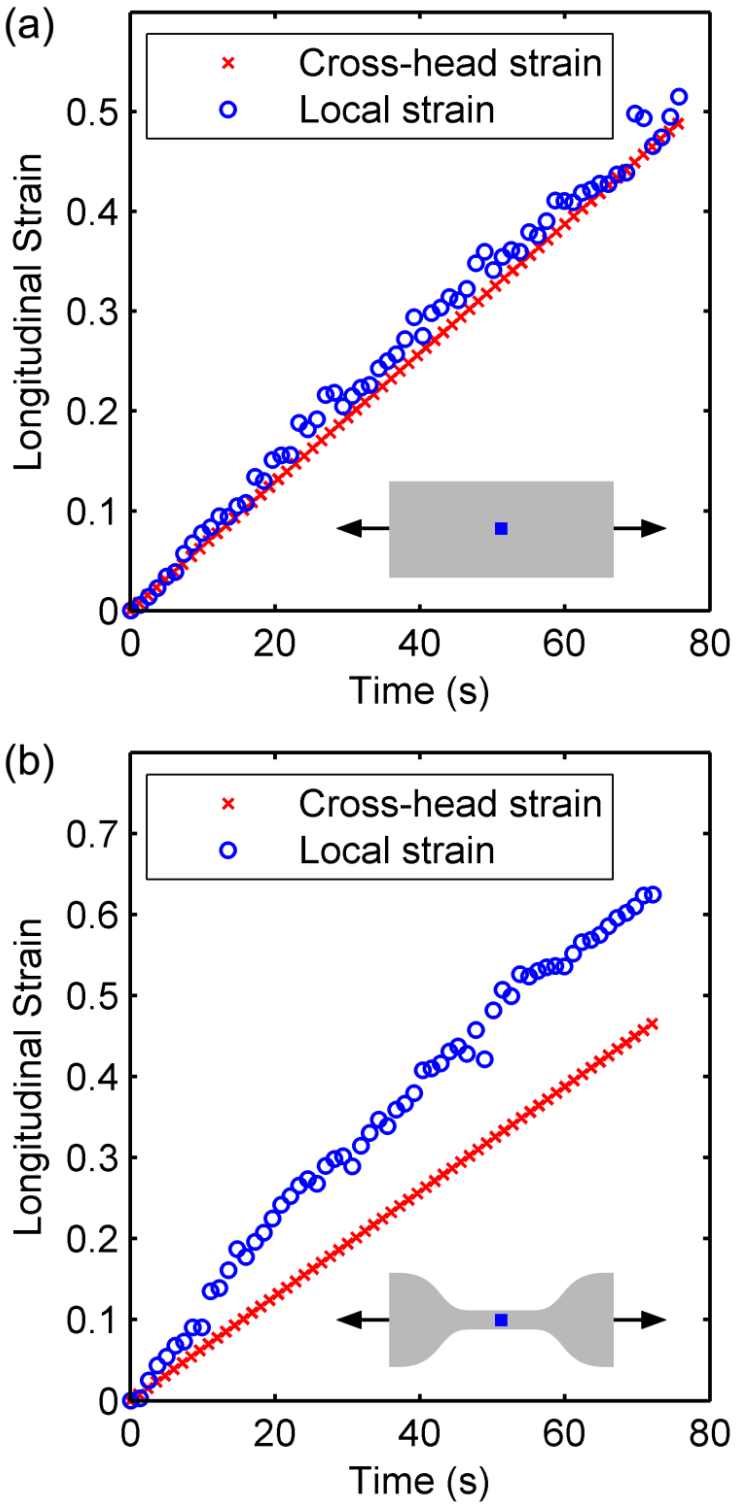

Figure 3.9: Comparison of local longitudinal strain and cross-head strain for a rectangular sample (a) and a dog-bone sample (b).

For the dumbbell shaped specimen, the comparison of applied cross-head strain and local strain measured at the narrow neck region show that the local strain at the neck is larger than the cross-head strain (Figure 3.9b). This result agrees with our expectations based on finite element analysis. Note that the local strain rate is also greater than the cross-head strain rate. These results indicate that the cross-head strain is not a complete and sufficient measure of applied deformation when the sample has a non-uniform geometry, and the spatial distribution of strain should be accounted for in such cases. This has crucial implications for bio-mechano-transduction studies that are performed using uniaxial stretcher setups since the strain that is applied to a single cell on the deformed substrate needs to be measured for an accurate correlation between mechanical deformation and cell response.

Chapter 4

MEMS TRACTION SENSOR

The MEMS traction sensor developed in this work is designed around the idea of creating a "smart" surface that can measure the in-plane traction forces between the surface itself and adherent cells. The surface comprises a two dimensional array of individual force sensors capable of simultaneous quantitative measurement of in-plane cell-substrate interaction forces at multiple loci of adhesion of a single cell within the sub-microNewton range. The novelty of this design lies in the ability to produce a 2D map of traction forces between a single cell and the substrate using a single MEMS chip, enabling other external instrumentation such as optical microscopy, AFM, or mechanical probing to be optimized and utilized for examining biochemical events, or for probing the cell. Figure 4.1 illustrates the experimental setup that is envisioned. In this setup, the MEMS sensor array and the adherent cells are placed in a chamber that consists of two glass plates separated by a PDMS spacer. The chamber has an inlet and an outlet for the circulation of an aqueous solution creating a suitable environment for cell viability in terms of temperature, acidity, etc., and also supplying the cells with nutrients. While the MEMS traction sensor array can be used for the measurement of cell-substrate interaction forces, the cells can simultaneously be imaged by optical microscopy using an oil-immersion objective and biochemical events or cellular processes can be examined. The specific experiment proposed in this study is the imaging of the intermediate filament networks of neurons by fluorescent microscopy and establishing correlations between the properties and mechanical response of IF networks and measured traction force fields. We believe that such investigations will provide new insights useful for the diagnosis and treatment of various diseases related to pathological IF networks in neurons.

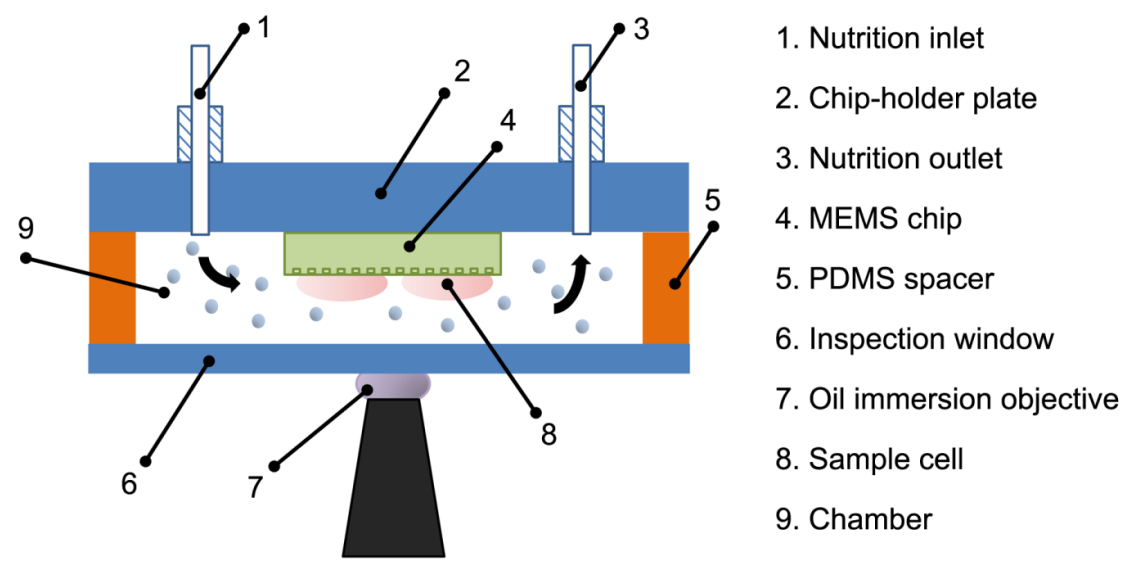

Figure 4.1: Schematic of an experimental setup where cells adhered on the MEMS traction sensor array are held in a suitable aqueous environment while imaging of cellular processes and measurement of traction force field are carried out simultaneously.

In this section, the electromechanical design and fabrication of individual MEMS traction sensors are reported, and a method for the characterization of these sensors and design methodology and fabrication flow for a sensor array are proposed.

4.1. Electromechanical Design of MEMS Traction Sensor

The key factors determining the electromechanical design of the MEMS traction sensor are the size and force scales, function, and the fabrication technology. To measure cell traction forces at multiple points, the sensor size needs to be smaller than the critical dimension of the cell, so the upper limit of sensor size is determined by cell size. The lower limit is determined primarily by the fabrication technology. The dimensions of the sensor design reported in this study are 20x20x2 μm. In other words, the sensor covers an area of 20x20 μm and has a thickness of 2 μm. Although some cells have smaller sizes than these dimensions, an array of sensors having these dimensions can be used to measure traction forces at multiple points along the length of axons which can have lengths reaching macroscale dimensions. Furthermore, the sensor dimensions reported in this section are determined primarily by the fabrication constraints and our device design can be further miniaturized without performance loss and can be fabricated using techniques that were not available to us.

In terms of the working principle, our MEMS traction sensor design is based on using piezoresistive silicon nanowires (NWs) as electromechanical transducers. Piezoresistivity is an electromechanical effect, observed in doped silicon among other materials, whereby applied mechanical stress causes a change in the material's electrical resistivity. Compared to other commonly used methods of transduction such as capacitive, magnetic, or optical transduction, the method of piezoresistive transduction has a key advantage which is the ability to use silicon NW piezoresistors and thus build sensors having considerably miniaturized sizes. Using piezoresistive silicon NWs, the critical dimensions of the devices can be reduced from micrometers to tens of nanometers. This level of miniaturization is impractical with capacitive transducers, because the capacitances become too small to measure as the electrodes shrink down to the nanoscale. Piezoresistive silicon nanowires also offer high sensitivity and – in quasi-static DC measurements – immunity to parasitic capacitances and inductances. Allain *et al* [87] developed a test device comprising an electrostatic actuator, electrostatic capacitive displacement sensor, and a piezoresistive silicon NW connected in series and fabricated on a single chip. They used the capacitive sensor and the piezoresistive NW to measure the same displacement that was generated by the electrostatic actuator. Their results (Figure 4.2) show that piezoresistive NWs have superior performance in terms of measurement resolution and noise compared to capacitive sensing mechanisms.

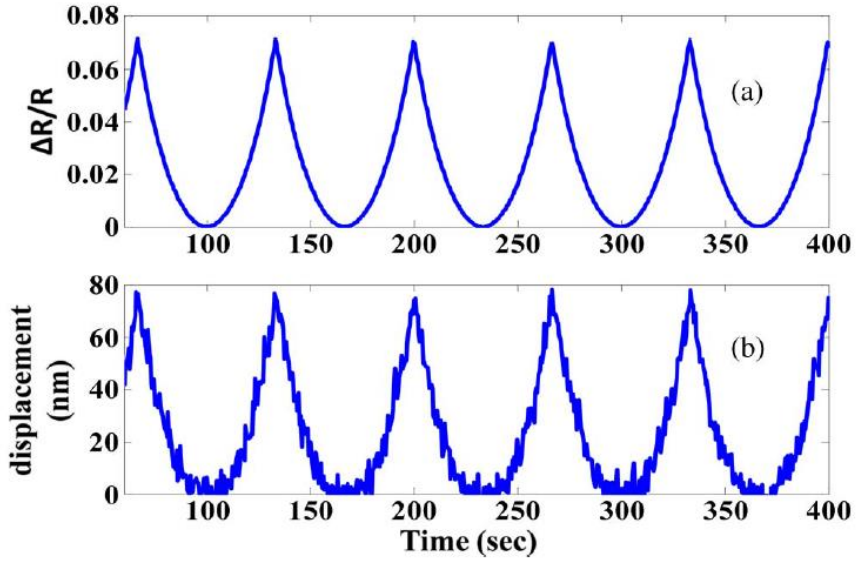

Figure 4.2: Comparison of the relative change in resistance of a piezoresistive silicon NW (top) and the output of a capacitive displacement sensor (bottom) as a response to the same applied displacement [87].

The methodology we used for the design of the MEMS traction sensor was laid out in two stages that interdependently focus on optimizing sensor performance. The first stage is optimizing the piezoresistor performance by the careful selection of design and fabrication process parameters. This requires reviewing the mathematical description of the piezoresistive effect and the piezoresistive properties of single crystal silicon. The second stage is the optimization of the sensor's mechanical response using finite element modelling. These efforts are outlined in the following subsections and the developed device design is presented.

4.1.1. Piezoresistance of Single Crystal Silicon

For an anisotropic crystalline material, the electric field ($\boldsymbol{E}$) and current ($\boldsymbol{i}$) vectors in 3D space are related to each other by the relationship,

$$\boldsymbol{E}_i = \boldsymbol{\rho}_{ij}\boldsymbol{i}_j \tag{4.1}$$

Where $\boldsymbol{\rho}_{ij}$ is the resistivity tensor of second rank. Piezoresistivity is described by the constitutive relation between the relative change in resistivity and the applied stress:

$$\frac{\Delta\boldsymbol{\rho}_{ij}}{\rho_o} = \boldsymbol{\pi}_{ijkl}\boldsymbol{\sigma}_{kl} \tag{4.2}$$

Here, ρ_o is the resistivity in the unstressed state which is scalar for the case of silicon since single crystal silicon is an isotropic conductor in the unstressed state. $\boldsymbol{\pi}_{ijkl}$ is the piezoresistance tensor of fourth rank, the elements of which are the material properties called the piezoresistance coefficients. In the most general case, the piezoresistance tensor has 81 components. Since the resistivity, stress, and piezoresistance tensors are all symmetrical, the number of independent components reduces to 21. Furthermore, for an anisotropic single crystal with cubic symmetry, the number of independent nonzero components reduces to 3 which are π_{1111}, π_{1122}, and π_{2323}. Using the short-hand notation (double indices are reduced to single indices: 11→1, 22→2, 33→3, 23→4, 13→5, 12→6), the relation between relative change in resistivity and stress can be written in matrix form as,

$$\begin{bmatrix}\Delta\rho_1/\rho_0\\ \Delta\rho_2/\rho_0\\ \Delta\rho_3/\rho_0\\ \Delta\rho_4/\rho_0\\ \Delta\rho_5/\rho_0\\ \Delta\rho_6/\rho_0\end{bmatrix} = \begin{bmatrix}\pi_{11} & \pi_{12} & \pi_{12} & & & \\ \pi_{12} & \pi_{11} & \pi_{12} & & \emptyset & \\ \pi_{12} & \pi_{12} & \pi_{11} & & & \\ & & & \pi_{44} & 0 & 0 \\ & \emptyset & & 0 & \pi_{44} & 0 \\ & & & 0 & 0 & \pi_{44}\end{bmatrix}\begin{bmatrix}\sigma_1\\ \sigma_2\\ \sigma_3\\ \sigma_4\\ \sigma_5\\ \sigma_6\end{bmatrix} \tag{4.3}$$

Equation 4.3 is valid only for single crystals with cubic symmetry [88, 89]

The reduction of the number of independent nonzero elements of the piezoresistance tensor from 81 to 3 simplifies the measurement of the piezoresistance coefficient values. Equation 4.3 is written with respect to an orthogonal coordinate frame whose axes coincide with the <100> directions of the cubic crystal lattice. The effective longitudinal and transverse piezoresistance coefficients along any arbitrary direction can be found by coordinate transformations. Table 4.1 gives the formulae for the calculation of effective longitudinal and transverse piezoresistance coefficients for the common configurations in which piezoresistors are utilized, and these configurations are illustrated in Figure 4.3.

Direction of strain	Direction of current	Configuration	Effective piezoresistance coefficient
<100>	<100>	Longitudinal	π_{11}
<100>	<010>	Transverse	π_{12}
<110>	<110>	Longitudinal	$(\pi_{11} + \pi_{12} + \pi_{44})/2$
<110>	$<1\bar{1}0>$	Transverse	$(\pi_{11} + \pi_{12} - \pi_{44})/2$

Table 4.1: Formulae for the effective piezoresistance coefficients for various configurations [88, 90].

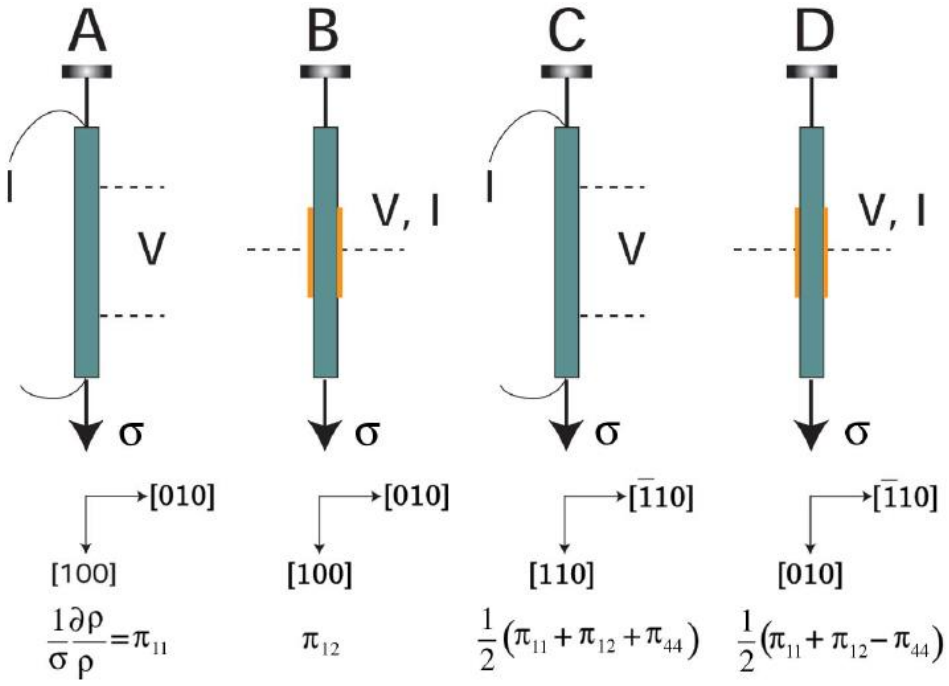

Figure 4.3: Test configurations that were used for the measurement of piezoresistance coefficients [89, 90].

Using the test configurations shown in Figure 4.3, Smith [90] measured the piezoresistance coefficients of silicon. In these tests, samples were loaded in uniaxial tension by hanging a weight at one end, and the resistances were measured by monitoring the voltage drop across the electrodes (dotted lines in Figure 4.3) while a constant current was applied. The results from configurations A and B in Figure 4.3 were used to directly determine the coefficients π_{11} and π_{12} respectively, and the value of π_{44} was inferred from the results of all four configurations [89, 90]. The results reported by Smith are shown in Table 4.2 below.

Piezoresistance coefficient	n-type silicon (resistivity = 11.7 Ωcm)	p-type silicon (resistivity = 7.8 Ωcm)
π_{11}	-102.2e-11 [Pa^{-1}]	6.6e-11 [Pa^{-1}]
π_{12}	53.4e-11 [Pa^{-1}]	-1.1e-11 [Pa^{-1}]
π_{44}	-13.6e-11 [Pa^{-1}]	138.1e-11 [Pa^{-1}]

Table 4.2: Piezoresistance coefficients of n-type doped and p-type doped silicon reported by Smith [90].

As evident from the values in Table 4.2, the piezoresistance coefficients depend on doping type. The piezoresistance coefficients also depend on crystal orientation, dopant concentration, and temperature. Hence, the dependence of piezoresistance on these factors was examined and suitable parameters were selected for the piezoresistor design.

The effect of crystal orientation on piezoresistance coefficients is due to the anisotropic nature of single crystal silicon. The values of π_{11}, π_{12}, and π_{44} in Equation 4.3 are defined such that the orthogonal coordinate frame according to which the directions of stress and resistivity are defined, coincides with the <100> directions of the cubic crystal lattice. The piezoresistance coefficient values for a coordinate system that is arbitrarily oriented with respect to the <100> crystal lattice frame can be computed using coordinate transformations. Kanda [91] used the values reported by Smith (Table 4.2) and plotted the effective longitudinal and transverse piezoresistance coefficients, π_L and π_T, of p-type and n-type doped silicon on the (100) crystal plane (Figure 4.4). His results show that for both p-type and n-type doped silicon, the maximum and minimum values of longitudinal and transverse piezoresistance coefficients correspond to either the <100> or the <110> directions on the (100) crystal plane. Note that, interestingly, these coefficients are the effective coefficients whose formulae were given in Table 4.1, and the configuration of stress and current that give these effective coefficients were shown in Figure 4.3. Table 4.3 gives the values of longitudinal and transverse piezoresistance coefficients of silicon along the <100> and <110> directions of the (100) plane, calculated from the values given in Table 4.2.

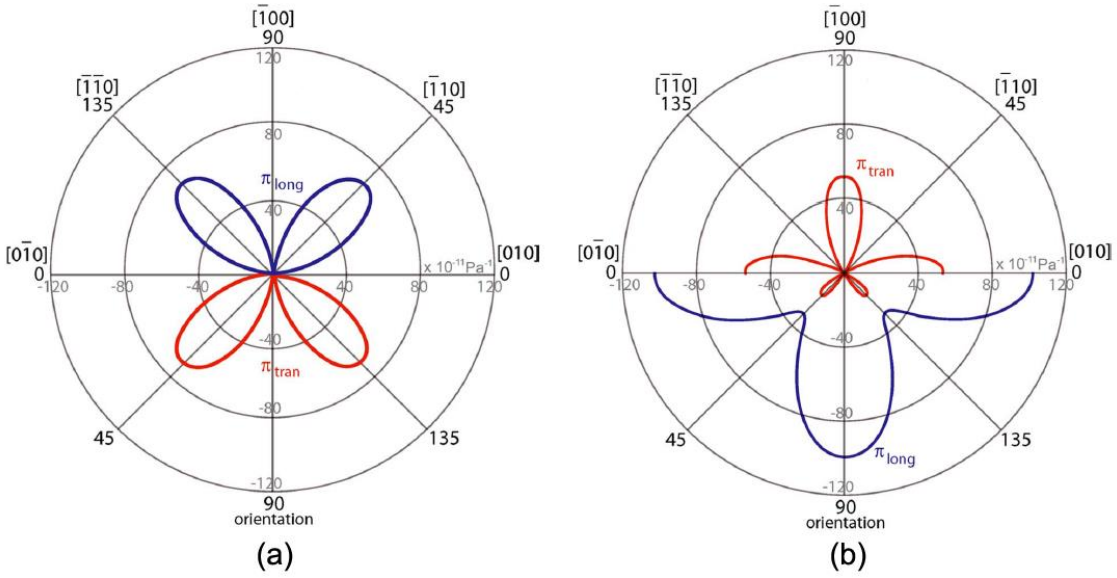

Figure 4.4: The longitudinal and transverse piezoresistance coefficients of p-type (a) and n-type (b) silicon on the (100) plane [89, 91].

direction on (100) plane	Effective longitudinal piezoresistance coefficient, πL		Effective transverse piezoresistance coefficient, πT	
	p-type silicon	n-type silicon	p-type silicon	n-type silicon
<100>	6.6e-11 [Pa^{-1}]	-102.2e-11 [Pa^{-1}]	-1.1e-11 [Pa^{-1}]	53.4e-11 [Pa^{-1}]
<110>	71.8e-11 [Pa^{-1}]	-31.2e-11 [Pa^{-1}]	-66.3e-11 [Pa^{-1}]	-17.6e-11 [Pa^{-1}]

Table 4.3: Values of the effective longitudinal and transverse piezoresistive coefficients of p-type and n-type silicon along the <100> and <110> directions of the (100) plane.

For the analysis of the orientation dependence of piezoresistance coefficients, we focused on the longitudinal and transverse coefficients along the directions that lie on the (100) plane of single crystal silicon. The reason for this is that silicon MEMS devices are fabricated on single crystal silicon wafers that are manufactured and supplied with predefined orientation. The most commonly used – hence the most easily available – silicon wafer orientation is the (100) wafer which is named as such because its top surface corresponds to the (100) crystallographic plane. Wafers have a disc shape with a flat which is a notch that indicates the orientation. In this project, we used wafers with (100) orientation that have [110] flats, that is, the directions parallel or perpendicular to the wafer flat are the <110> directions. Flats are used to control the alignment of fabricated features with respect to the crystallographic orientations. Figure 4.6 illustrates the orientations of nanowires fabricated along <100> and <110> directions on a (100) wafer. Fabricating nanowires oriented along the <100> directions requires a 45° alignment with the wafer flat. However, it is customary and convenient to align fabricated features parallel or perpendicular to the wafer flats since the alternative is a more difficult approach in photolithography. Thus, in our MEMS traction sensor design, we chose to use piezoresistive silicon nanowires that are oriented along the <110> directions.

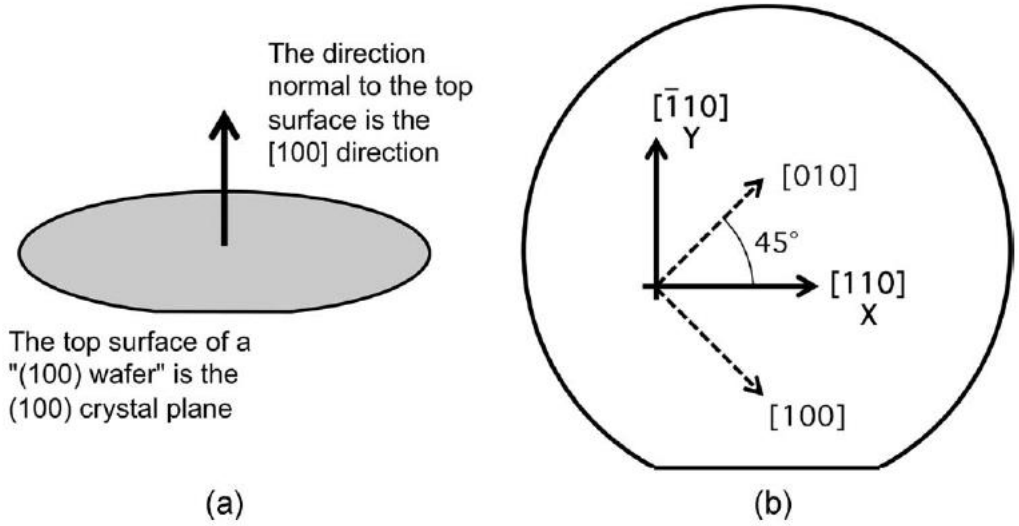

Figure 4.5: Crystal orientation of a (100) silicon wafer (a) and the in-plane crystallographic directions shown with respect to the wafer flat (b) [92].

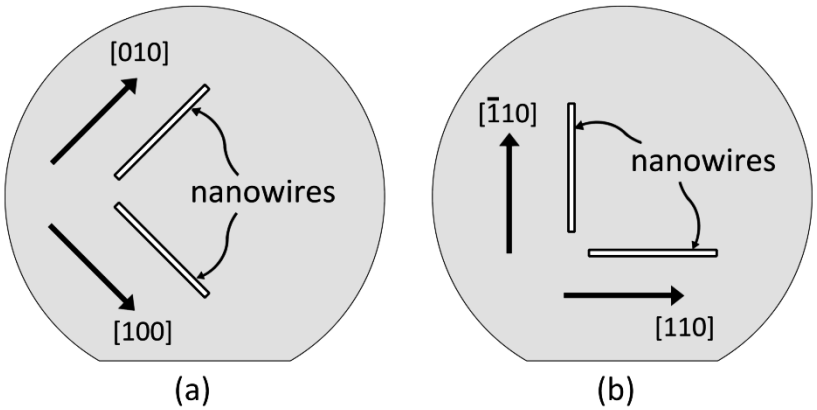

Figure 4.6: Nanowires oriented along <100> directions (a) and <110> directions on a (100) silicon wafer.

When using piezoresistive nanowires as electromechanical transducers, the most appropriate loading is uniaxial tension or compression where the transverse and shear components of stress are zero and the only non-zero stress component is the longitudinal (or axial) stress (σ_1 in Equation 4.3). In the case of a piezoresistive nanowire under uniaxial stress-state, Equation 4.3 reduces to a single scalar equation of the form,

$$\Delta\rho/\rho_o = \pi_L \sigma \tag{4.4}$$

where $\Delta\rho/\rho_o$ is the total relative change in resistivity of the nanowire, σ is the net uniaxial stress, and π_L is the effective longitudinal piezoresistance coefficient along the direction of the long axis of the nanowire. Note that Equation 4.4 is valid for a wire under uniaxial stress-state

in which the only non-zero stress component is the axial stress. In Equation 4.4, the piezoresistive response is characterized by a single scalar value which is the effective longitudinal piezoresistance coefficient. Since we already decided that the nanowires will be oriented along the <110> directions, we can now choose the dopant type using the values in Table 4.3. In this study, p-type doped silicon was chosen as the piezoresistive material since the effective longitudinal piezoresistance coefficient for p-type doped silicon is larger than that of n-type doped silicon by a factor of 2.3. Moreover, p-type doped silicon piezoresistors oriented along <110> directions are the most common choice for piezoresistive sensors [93, 94].

It is important to note that the value of π_L for p-type silicon along <110> directions that is given in Table 4.3 is calculated based on the values reported by Smith [90, 91] which is measured for a specific dopant concentration. Depending on the dopant concentration, the value of π_L will change, but the dependencies of the effective longitudinal piezoresistance coefficients of p-type and n-type doped silicon on dopant concentration follow similar trends [88]. Hence, the dependency on dopant concentration does not have an effect on our choice of dopant type.

The effect of dopant concentration was not evident in the initial findings of Smith. He saw that changing the dopant concentration did not have a profound effect on the piezoresistance coefficients [90]. However, the dopant concentrations of Smith's samples were very low (around 10^{15} cm^{-3}) and covered a narrow range. Numerous studies since Smith's publication have shown that dopant concentration has a significant effect on the piezoresistance coefficients. Kanda [91] introduced a theoretical model for the piezoresistance effect where he took the values reported by Smith as reference values and computed the piezoresistance factor, P(N,T) which he defined as the ratio of the piezoresistance coefficient at any dopant concentration (N) and temperature (T) to the reference values. Kanda's theoretical model shows that at room temperature, peizoresistance coefficients are approximately constant and equal to the reference value at low dopant concentrations but there is a steep drop in the piezoresistance coefficients as the dopant concentration increases above 10^{18} cm^{-3}. Experimental measurements of the piezoresistance coefficients of silicon suggest that while Kanda's model is reasonably accurate for low dopant concentrations (below 10^{17} cm^{-3}), it is inaccurate for high dopant concentrations [89, 95, 96]. Cho *et al* [96] provide a comprehensive review of the reported experimental values of piezoresistance

coefficients of silicon, and the combined data for p-type doped silicon and n-type doped silicon are shown in Figure 4.7 and Figure 4.8, respectively.

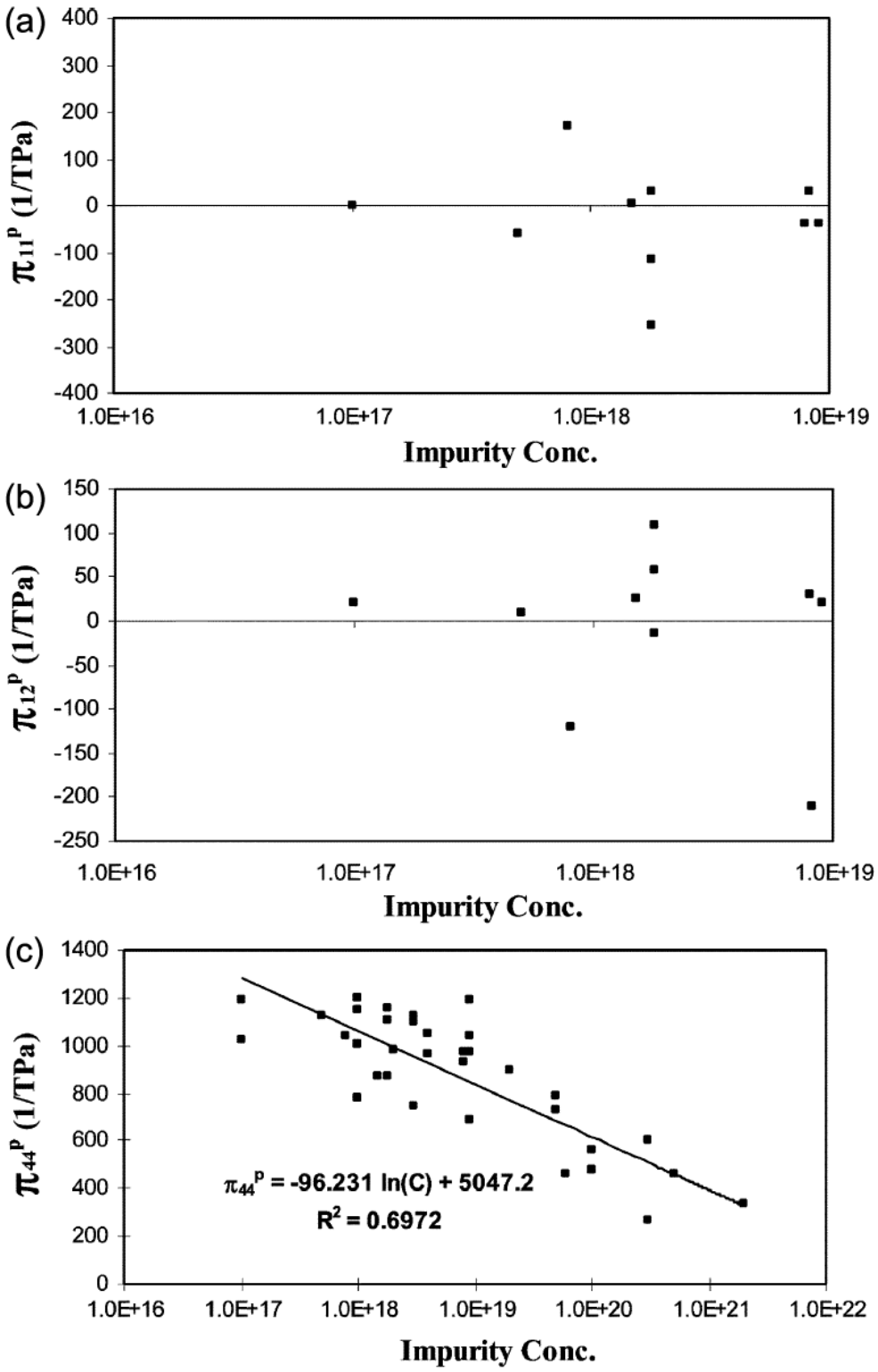

Figure 4.7: Experimentally measured values of the piezoresistance coefficients π_{11} (a), π_{22} (b), and π_{44} (c) of p-type doped silicon reported in literature [96].

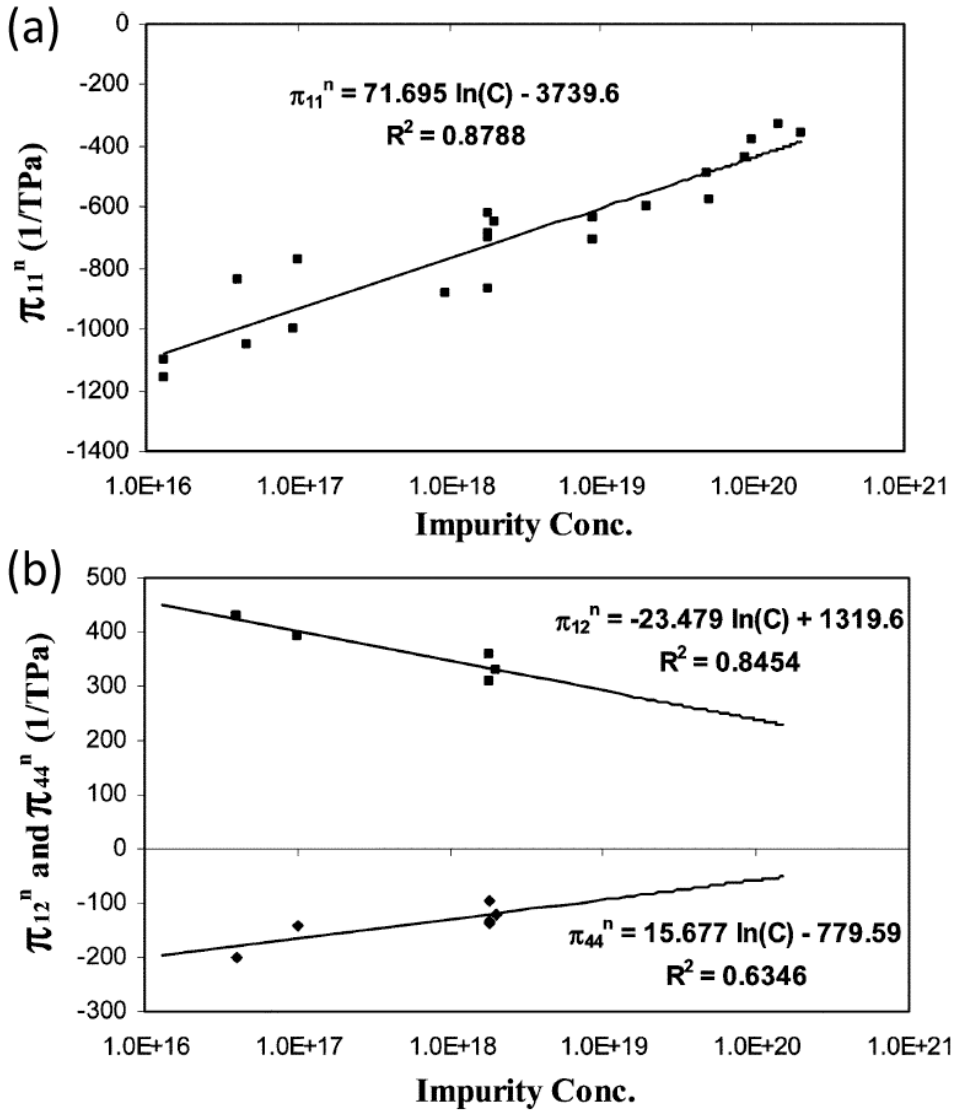

Figure 4.8: Experimentally measured values of the piezoresistance coefficients π_{11} (a), π_{22}, and π_{44} (b) of n-type doped silicon reported in literature [96].

The theoretical model [91] and experimental findings [96] for the piezoresistance coefficients do not agree with each other for dopant concentrations exceeding 10^{17} cm^{-3}. When designing piezoresistors with high dopant concentrations, it is more appropriate to use experimental values of piezoresistance coefficients as reference values because, depending on the selected dopant concentration, the actual piezoresistance coefficients may be up to an order of magnitude less than the original values reported by Smith (see Table 4.2). For dopant concentrations below 10^{17} cm^{-3}, there is not an adequate amount of experimental data to specify a trend, though the theoretical model suggests that the values of piezoresistance

coefficients remain relatively constant at low concentrations. Nonetheless, both theory and experimental data agree with each other around the critical dopant concentration value of 10^{17} cm^{-3} [89, 95, 96]. Based on the findings detailed above, we chose a dopant concentration of 10^{17} cm^{-3} and used the peizoresistance coefficient values in Table 4.2 for our piezoresistor design.

Another important factor affecting the values of piezoresistance coefficients is temperature. In fact, the high temperature coefficients of semiconductor resistance and piezoresistance coefficients are the major drawbacks of piezoresistive systems. While one can use the high temperature coefficients as an advantage by utilizing doped silicon resistors as thermal sensors [89], for applications using piezoresistors as electromechanical transducers, a strong temperature dependence is a disadvantage. Experimental studies on the temperature dependence of piezoresistive coefficients show that the magnitudes of all piezoresistance coefficients decrease with increasing temperature [96, 97]. The degree of nonlinearity in piezoresistive response depends on temperature as well [98]. The temperature coefficient of piezoresistance, which is the slope of the piezoresistance coefficient versus temperature curve, is inversely dependent on dopant concentration [89, 91, 93] as illustrated in Figure 4.9 for p-type and n-type doped silicon. In Figure 4.8, P(N,T) is the piezoresistance factor, defined by Kanda [91] as the piezoresistance coefficient value normalized by the reference value at room temperature (values in Table 4.2). Figure 4.9 shows that the dependence of piezoresistance coefficients on temperature (*i.e.* the temperature coefficient of piezoresistance) decreases significantly with increased dopant concentration. Even though increasing dopant concentration decreases the piezoresistive coefficients, the decrease in temperature coefficient is steeper. For this reason, it is common practice in piezoresistive MEMS sensor design to sacrifice from sensitivity and use high dopant concentrations in order to reduce the effect of temperature [89].

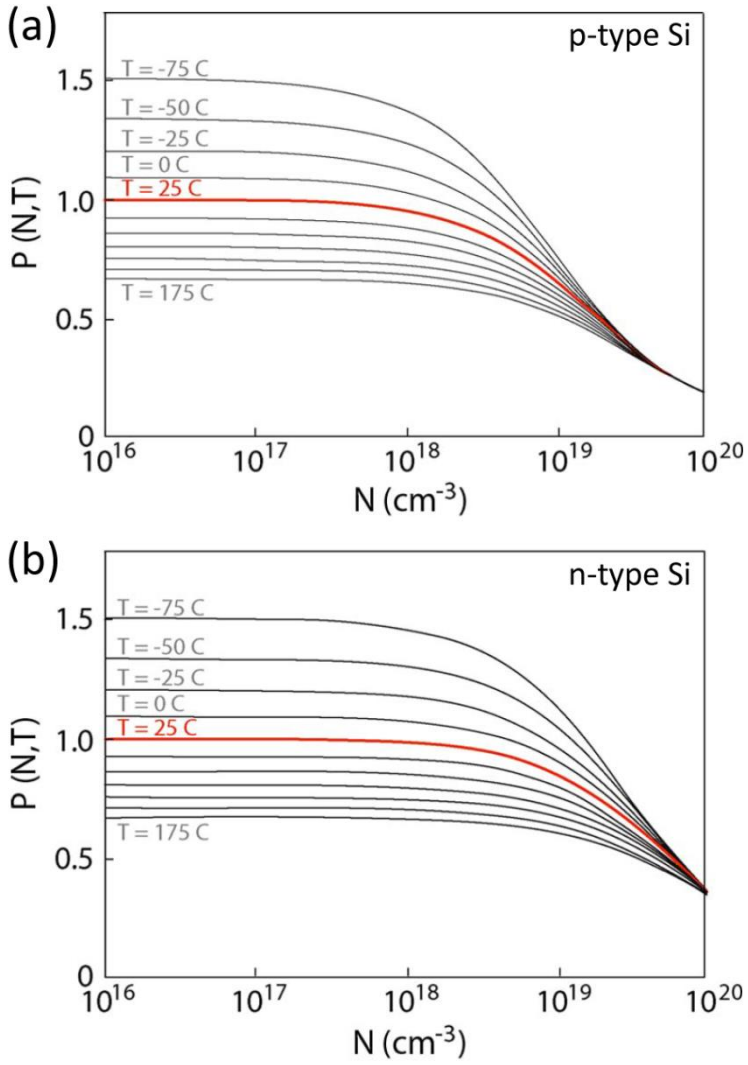

Figure 4.9: The temperature and dopant concentration of piezoresistance for p-type doped (a) and n-type doped (b) silicon [89].

Although selecting lower dopant concentrations reduces the temperature coefficient of piezoresistance, it does not eliminate the temperature effect entirely. There are, however, several methods that can be used to compensate for the thermal effects. One method is to incorporate a reference piezoresistor on which no stress is applied during the operation of the sensor. This way, the resistivity changes of the stressed piezoresistor and of the unstressed reference piezoresistor can be compared to compute the change in resistivity due to applied load only [99]. Using a Wheatstone bridge conditioning circuit is also common practice to compensate for thermal effects [88, 89, 99], though the Wheatstone bridge only compensates for the first order effects of temperature.

A unique advantage that we have in our study is that the target application for our sensor design is the measurement of surface traction forces between live cells and the substrate which requires that the environmental temperature should be kept within the very narrow range of 37±0.5°C corresponding to the human body temperature. This very narrow range specification for the working temperature allows us to use a low dopant concentration of 10^{17} cm^{-3} at the cost of a large temperature coefficient of piezoresistance since the temperature effect can be neglected in such a narrow range of temperatures. However, it is important to note that even if the environmental temperature remains constant, temperature effects may still be observed due to thermal drift – the heating of the piezoresistor as a result of the dissipated power [99]. We expect very low heat dissipation since the dopant concentration we selected is low, resulting in high resistance. Nevertheless, in our fabrication layout (discussed in detail in the next section), we incorporated two versions of each device design with and without on-chip Wheatstone bridge circuits to investigate the effect of thermal drift.

Another important factor to consider in piezoresistor design besides the piezoresistance coefficients is the noise level, which is known to be dependent on dopant concentration. At lower dopant concentrations, noise level increases due to decreased charge carrier concentration and decreased conductivity; and the inverse effect is seen with increasing dopant concentration. However, the decline in the magnitude of piezoresistance coefficients with increasing dopant concentration is larger than the decline in noise level – especially for quasi-static applications [95, 100].

Considering the factors involved in piezoresistor design as discussed above, the process parameters for piezoresistor fabrication that were selected in this study are summarized in Table 4.4.

Dopant type	p-type (Boron doping)
Dopant concentration	10^{17} cm^{-3}
Orientation	<110> directions on the (100) plane

Table 4.4: Process parameters selected for piezoresistor design.

For the integration of piezoresistive response into the mechanical modeling (discussed in the following sub-section) the piezoresistive gauge factor was used as the piezoresistor

sensitivity. The piezoresistive gauge factor for a nanowire under uniaxial stress-state can be derived from Equation 4.4 by first equating the relative change in resistivity to the relative change in resistance,

$$\Delta R/R_o = \pi_L \sigma \tag{4.5}$$

The relative change in resistance can be caused by both the relative change in resistivity and the changes in geometry, but for doped silicon, the relative change in resistivity dominates by up to two orders of magnitude. Therefore, the geometry effects can be neglected and Equation 4.5 can be used instead of Equation 4.4 [89, 93]. This simplification is useful because measuring resistance is more practical than measuring resistivity, since the latter requires that the sample geometry be known. Equation 4.5 can be further simplified by implementing Hooke's law,

$$\Delta R/R_o = \pi_L E_{eff} \varepsilon \tag{4.6}$$

where E_{eff} is the effective elastic modulus (or Young's modulus) along the axial direction of the nanowire, and ε is the applied axial strain. Note that although the elastic modulus is not dependent on dopant concentration or temperature (within the working ranges), it is dependent on the crystal orientation due to the anisotropy of silicon. Figure 4.10 shows the orientation dependence of the elastic modulus of silicon. On the (100) crystal plane of silicon, the effective elastic modulus is maximum along the <110> directions with a value of 169 GPa [92]. The product of effective longitudinal piezoresistance coefficient and the effective elastic modulus in Equation 4.6 is called the piezoresistive gauge factor, G.

$$G = (E\pi)_{eff} = \frac{\Delta R}{R_o}\frac{1}{\varepsilon} \tag{4.7}$$

G is defined as the sensitivity of a piezoresistive nanowire and is equal to the ratio of relative change in resistance of the nanowire (response) to the applied axial strain (input). The value of the gauge factor for a p-type doped silicon nanowire with a dopant concentration of 10^{17} cm^{-3} oriented along the <110> crystallographic directions is calculated using the corresponding value of effective longitudinal piezoresistance coefficient in Table 4.3 and the value of 169 GPa for the elastic modulus, and it is found to be equal to 121.34. This piezoresistive gauge factor value is used in the following stage of sensor design.

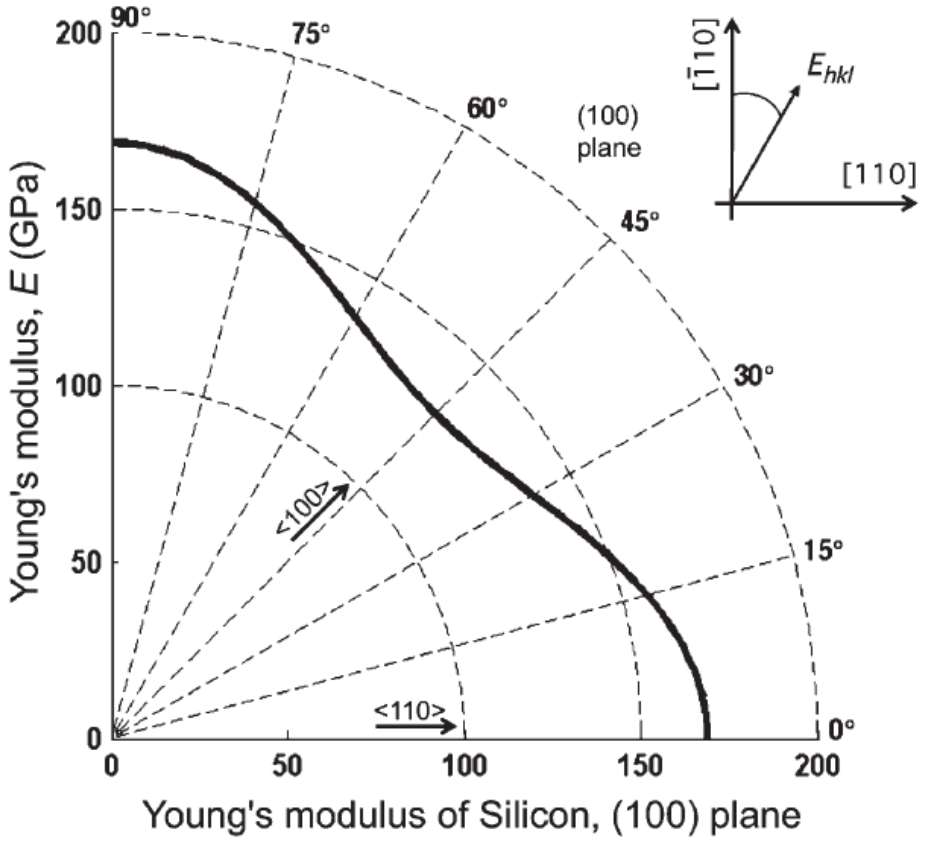

Figure 4.10: The elastic modulus of silicon for different orientations on the (100) plane [92].

4.1.2. Mechanical Design

The second stage of the sensor design is to come up with a mechanical structure that is able to effectively transmit the in-plane traction forces applied by the cell to the piezoresistive nanowires. While the piezoresistor design efforts discussed in the previous sub-section were carried out to maximize the relative change in resistance per given axial strain, the mechanical design efforts detailed here are carried out to maximize the axial strain per given applied force. COMSOL Multiphysics ® finite element modeling software was used to model the sensor geometry and determine the strain on the nanowires per applied force.

Figure 4.11 shows the basic schematic of the sensor structure showing the key components which are the interaction platform, piezoresistive nanowires, and the springs. The interaction platform is a suspended plate anchored by the springs and the nanowires. It is the structure with which the cells are going to interact and apply forces on. The interaction platform transmits the applied force onto the nanowires and applies strain on them. The function of the springs is to keep the motion of the platform in-plane.

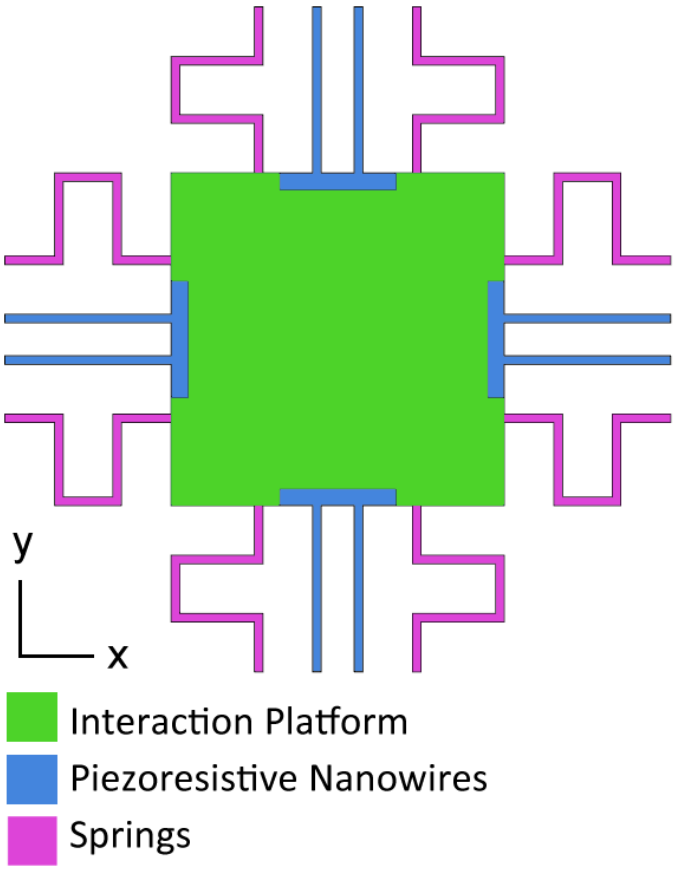

Figure 4.11: Schematic of the sensor design illustrating the basic components.

The sensor design comprises four nanowire pairs perpendicular to each edge of the platform. The reason for configuring nanowires in pairs is to achieve a closed-circuit for measurement. Since resistance measurement requires at least two electrical terminals, a single nanowire configuration would require an electrical connection to be made at the point where the nanowires are connected to the platform. Since the platform is a suspended moving structure, it is difficult to make such an electrical contact. Instead, two nanowires are arranged as a bridge between the anchor and the platform. The ends of the nanowires at the platform are connected together, and the anchored ends are used as the two electrical terminals of the piezoresistor.

Having four nanowire pairs oriented along perpendicular directions enables the sensing of the in-plane direction of applied force. When a force is applied in the positive x direction, the nanowire pair at the left-hand side experiences tensile strain while the nanowire pair at the right-hand side experiences compressive strain. The magnitudes of these tensile and compressive strains are equal but the signs are different. The resistance of the nanowires

loaded in tension increases whereas resistance decreases for the compressed nanowires. This way, the direction of a force parallel to the x-axis (whether it is to the right or to the left) can be determined. The same logic works for the determination of the direction of a force applied parallel to the y-axis (Figure 4.12a).

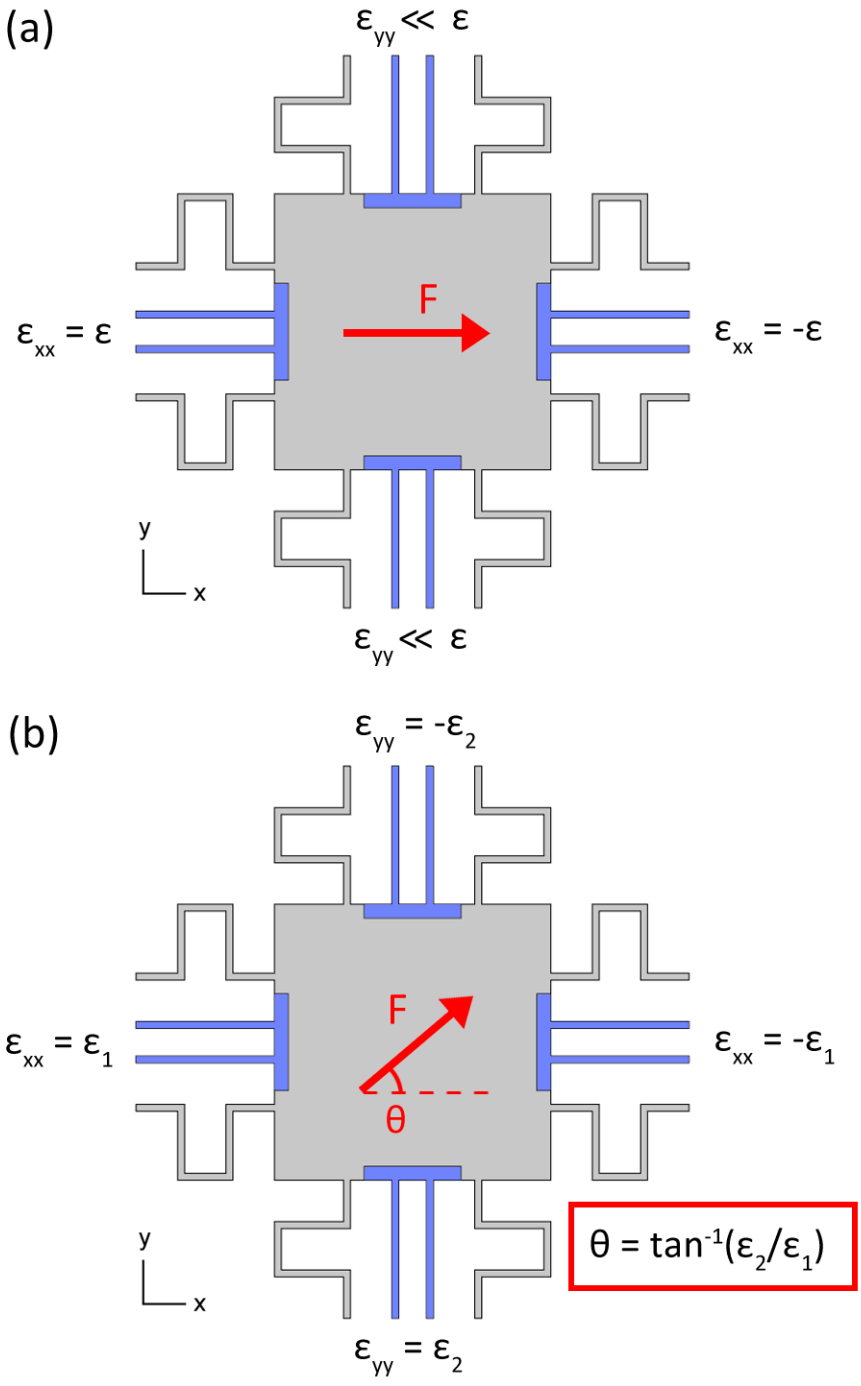

Figure 4.12: The method of detection of the direction of in-plane force. The angle the force vector makes with the horizontal axis can be determined by taking the arctangent of the ratio of strain magnitude on the vertical nanowires to that of horizontal nanowires.

The direction of a force applied in an arbitrary direction can also be determined. The direction is defined by the angle θ that the force vector makes with the positive x axis (Figure 4.12b). In this case, the magnitude of strain on the vertically oriented nanowires and the magnitude of strain on the horizontally oriented nanowires are called ε_2 and ε_1, respectively. Then, the direction of force i.e. the angle θ can be found as,

$$\theta = \tan^{-1}(\varepsilon_2/\varepsilon_1) \tag{4.8}$$

The schematic shown in Figure 4.11 is the top view. One important design aspect that is not visible in the top view is the different thicknesses of the basic components. In this work, the word thickness refers to the dimensions perpendicular to the wafer plane while in-plane dimensions are referred to as width or length. Figure 4.13 shows the dimensions of our basic sensor design including the cross-sectional view and the different thicknesses. The widths of the nanowires and springs were selected as 0.25 µm because this is the smallest dimension that we could fabricate using photolithography. The nanowire cross-section was then designed as 0.25 x 0.25 µm. The thickness of the springs and platform were 2 µm because this is the thickness of the device layer of the silicon-on-insulator (SOI) wafers that we used to fabricate our sensor designs.

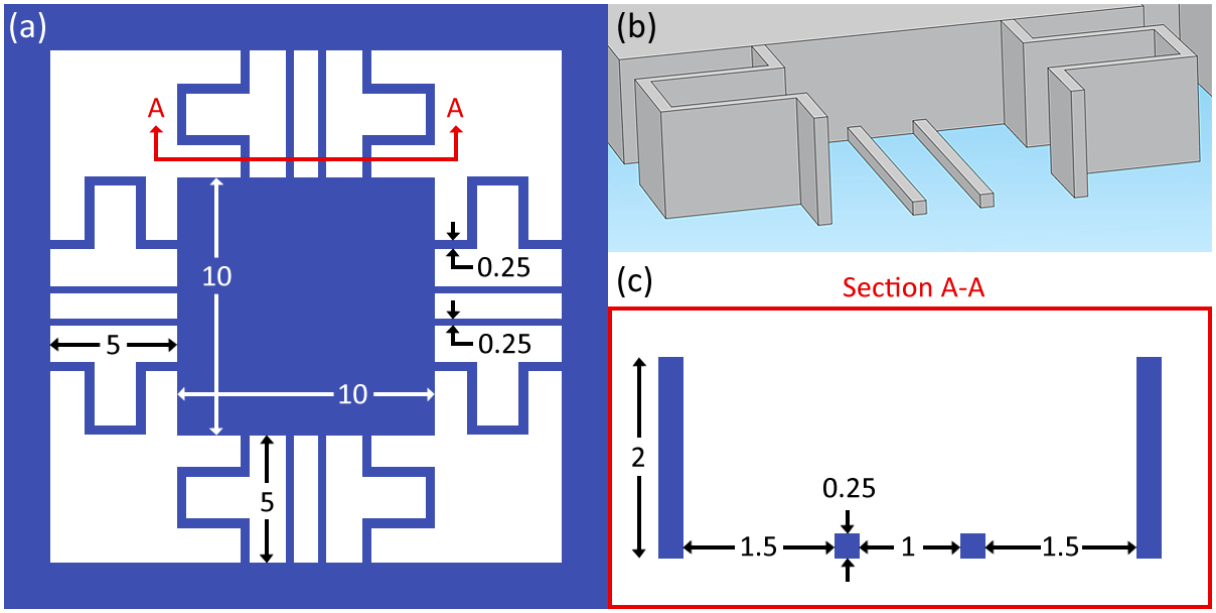

Figure 4.13: In plane-dimensions (a), inclined view (b), and the cross-sectional dimensions (c) of the basic sensor design.

Since the traction force is applied on the top surface of the interaction platform, it creates a moment with respect to the mass center of the platform. This moment causes an out-of-plane tilting motion of the platform, consequently bending the nanowires. This is an undesired effect since the nanowires should be in a uniaxial stress-state for effective transduction. Bending stresses induce non-uniformity in the stress distribution and reduces the net tensile or compressive stress. In the case of pure bending, the effects of compressive and tensile stresses cancel each other out and the net stress becomes zero. As a result, no resistance change can be observed. The springs were designed to constrain the motion of the platform to in-plane motion and maintain a uniaxial stress-state in the nanowires. To illustrate the function of the springs, the device design having dimensions shown in Figure 4.13 was modelled in COMSOL Multiphysics ® with and without springs. A force of 100 nN was applied on the top surface of the platform along the positive x-axis and the strain in x-direction was plotted. Figure 4.14 gives a qualitative comparison of deformation as a response to the same applied load for designs with and without the springs. In these plots, the deformations are exaggerated, but they are all exaggerated by the same factor of 1000.

Figure 4.14 gives a qualitative comparison. To quantify the effect of springs, we defined the percent deviation from uniaxial stress state as the ratio of the difference of axial stress σa and von-Mises stress σ' to von-Mises stress:

$$percent\ deviation\ from\ uniaxial\ stress\ state = 100\ (\sigma_a - \sigma')/\sigma' \qquad (4.9)$$

For nanowires loaded in tension, the first principal stress component is the axial stress component, and the von-Mises stress is an equivalent stress incorporating the effects of all stress components. In the case of pure uniaxial stress, the value calculated from Equation 4.9 should be zero.

For the sensor design with springs (Figure 4.14a and Figure 4.14b), the deviation from uniaxial stress-state was calculated to be 0.5%. For the same design without springs (Figure 4.14c and Figure 4.14d), the deviation from uniaxial stress-state was calculated to be 40%. It is also evident from a qualitative comparison as shown in Figure 4.14 that springs help maintain a uniform uniaxial stress-state. Figure 4.14c and Figure 4.14d show the strain distributions on the nanowires. The strain on the top surface is compressive at one end and tensile at the other end. Such a distribution is characteristic of a structure under bending stress.

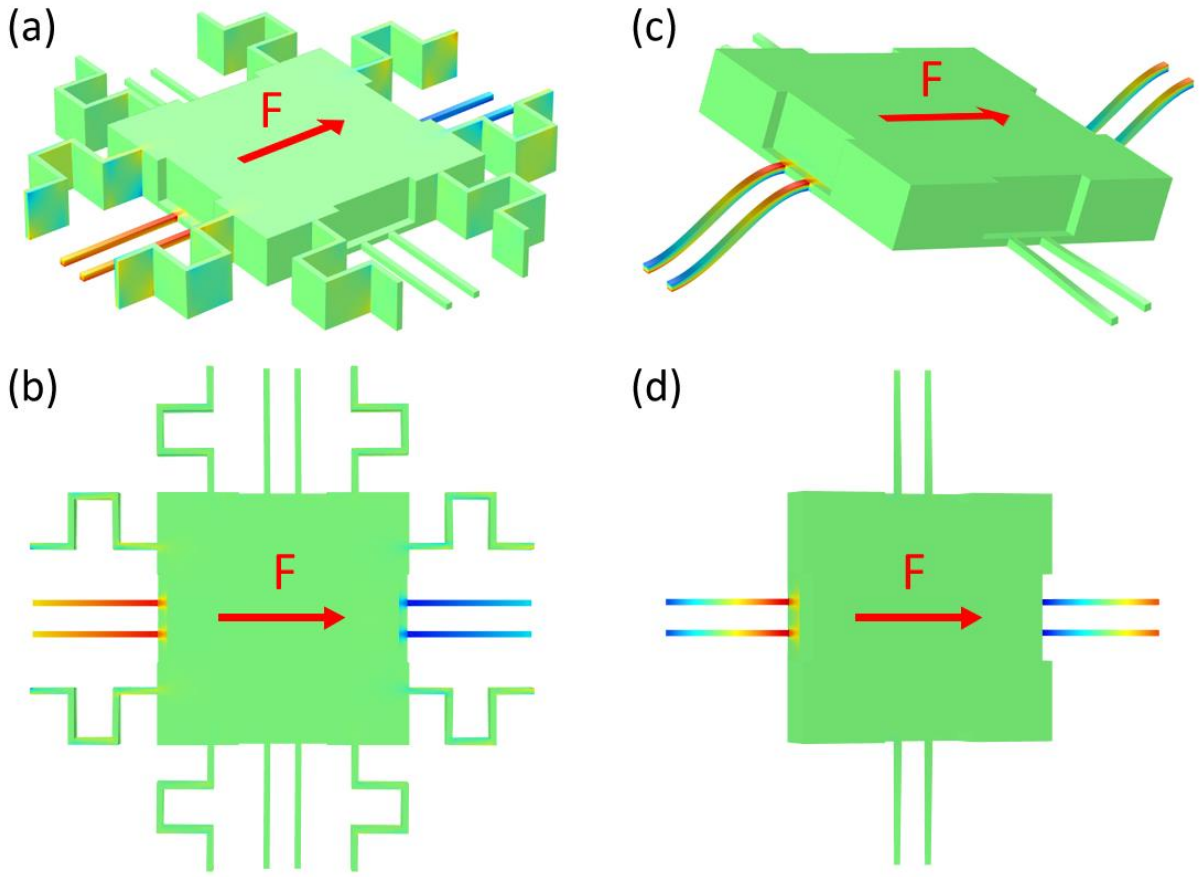

Figure 4.14: The isometric (a) and top (b) views of strain plots for a design with springs. The isometric (c) and top (d) views of strain plots for a design without springs.

This important function of the springs is attributed to the differences in the stiffness of springs along in-plane and out-of-plane directions. The thickness of the springs is much higher than their width, which makes the bending stiffness high, and so reduces the tilting motion. However, we also want to keep the in-plane stiffness as low as possible so that the applied force is transmitted to the nanowires effectively. This is achieved by designing springs with folded geometry. The effects of spring width and spring thickness on the mechanical response of the sensor were analyzed quantitatively using finite element analysis. A force of 100 nN was applied on the top surface of the platform parallel to the x-axis and the axial strain on the nanowires directed along the x-axis was calculated for different spring width and spring thickness values. The result is shown in Figure 4.15.

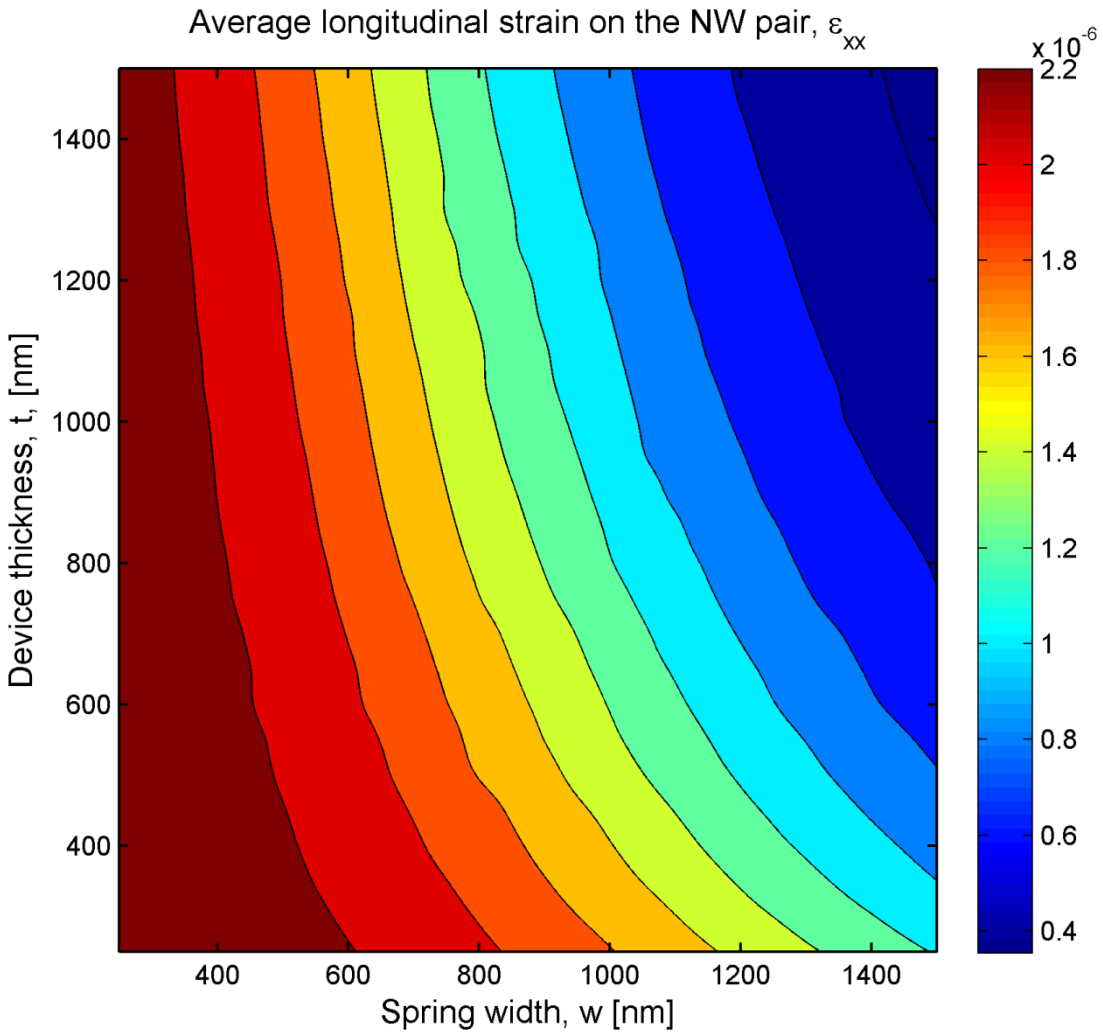

Figure 4.15: The effects of spring width and spring thickness on the axial strain on nanowires.

It is evident from Figure 4.15 that the spring width has a significant effect on the axial strain whereas spring thickness has a little effect. A high value of spring thickness is critical to the function of the springs to reduce out-of-plane tilting. Fortunately, increasing the spring thickness does not reduce the effectiveness of the transmission of force onto the nanowires. To have an effective design, it is important to have a minimum spring width though. A spring width of 0.25 μm was chosen in our design since it is the minimum width allowed by fabrication constraints.

The output of a piezoresistive sensor is a relative change in resistance which can be computed by monitoring the resistance value. A conventional way to measure resistance is to perform I-V characterization of the resistor where the applied voltage is swept and current flow is measured. Such a measurement can be carried out using a source-measure-unit

(SMU). To predict the piezoresistive response of our sensor design, we multiplied the strain value obtained from finite element modeling in COMSOL with the gauge factor value of 121.34. This gives us the expected value of the relative change in resistance in response to the applied force. For the applied force, we used a value of 100 nN in all simulations for a consistent comparison. Assuming that the entire piezoresistor is strained, and a constant SMU voltage V is applied, the relative change in current $\Delta I/I_o$ can be equated to the relative change in resistance $\Delta R/R_o$. The static current I_o can be calculated using Ohm's Law with a constant SMU voltage V and initial unstressed total resistance of the piezoresistor R_o. The magnitude of current change ΔI can then be calculated as the product of static current I_o and the relative change in current $\Delta I/I_o$. In our simulations, we used an SMU voltage value of 10 V.

We investigated the effect of nanowire dimensions on the output of the sensor. For the nanowire dimensions, we used four different length values ranging from 2 µm to 5 µm and four different width values ranging from 100 nm to 250 nm. Nanowire thickness was kept constant at 250 nm. We ran simulations for each combination of length and width, and calculated the values of current change and relative change in current for an applied load of 100 nN and an SMU voltage of 10 V. To be able to assess whether these signals can be measured or not, we used the specifications provided on the datasheet of Keithley 4200-SCS SMU device. These specifications are shown in Table 4.5. For the medium power SMU, the measurement accuracy limit depends on the magnitude of the static current. Figure 4.16 shows the outputs of devices having different nanowire dimensions plotted together with the measurement accuracy limit of the SMU.

				MEASURE		SOURCE	
		CURRENT RANGE[1]	MAX. VOLTAGE	RESOLUTION[3]	ACCURACY ±(% rdg + amps)	RESOLUTION[3]	ACCURACY ±(% rdg + amps)
4210-SMU[2] High Power SMU		1 A	21 V	1 µA	0.100% + 200 µA	50 µA	0.100% + 350 µA
		100 mA	210 V	100 nA	0.045% + 3 µA	5 µA	0.050% + 15 µA
	4200-SMU[2] Medium Power SMU	100 mA	21 V	100 nA	0.045% + 3 µA	5 µA	0.050% + 15 µA
		10 mA	210 V	10 nA	0.037% + 300 nA	500 nA	0.042% + 1.5 µA
		1 mA	210 V	1 nA	0.035% + 30 nA	50 nA	0.040% + 150 nA
		100 µA	210 V	100 pA	0.033% + 3 nA	5 nA	0.038% + 15 nA
		10 µA	210 V	10 pA	0.050% + 600 pA	500 pA	0.060% + 1.5 nA
		1 µA	210 V	1 pA	0.050% + 100 pA	50 pA	0.060% + 200 pA
		100 nA	210 V	100 fA	0.050% + 30 pA	5 pA	0.060% + 30 pA
4200-SMU and 4210-SMU with optional 4200-PA PreAmp		10 nA	210 V	10 fA	0.050% + 1 pA	500 fA	0.060% + 3 pA
		1 nA	210 V	3 fA	0.050% + 100 fA	50 fA	0.060% + 300 fA
		100 pA	210 V	1 fA	0.100% + 30 fA	15 fA	0.100% + 80 fA
		10 pA	210 V	0.3 fA	0.500% + 15 fA	5 fA	0.500% + 50 fA
		1 pA	210 V	100 aA	1.000% + 10 fA	1.5 fA	1.000% + 40 fA

VOLTAGE COMPLIANCE: Bipolar limits set with a single value between full scale and 10% of selected voltage range.

Table 4.5: SMU current measurement specifications of the Keithley 4200-SCS.

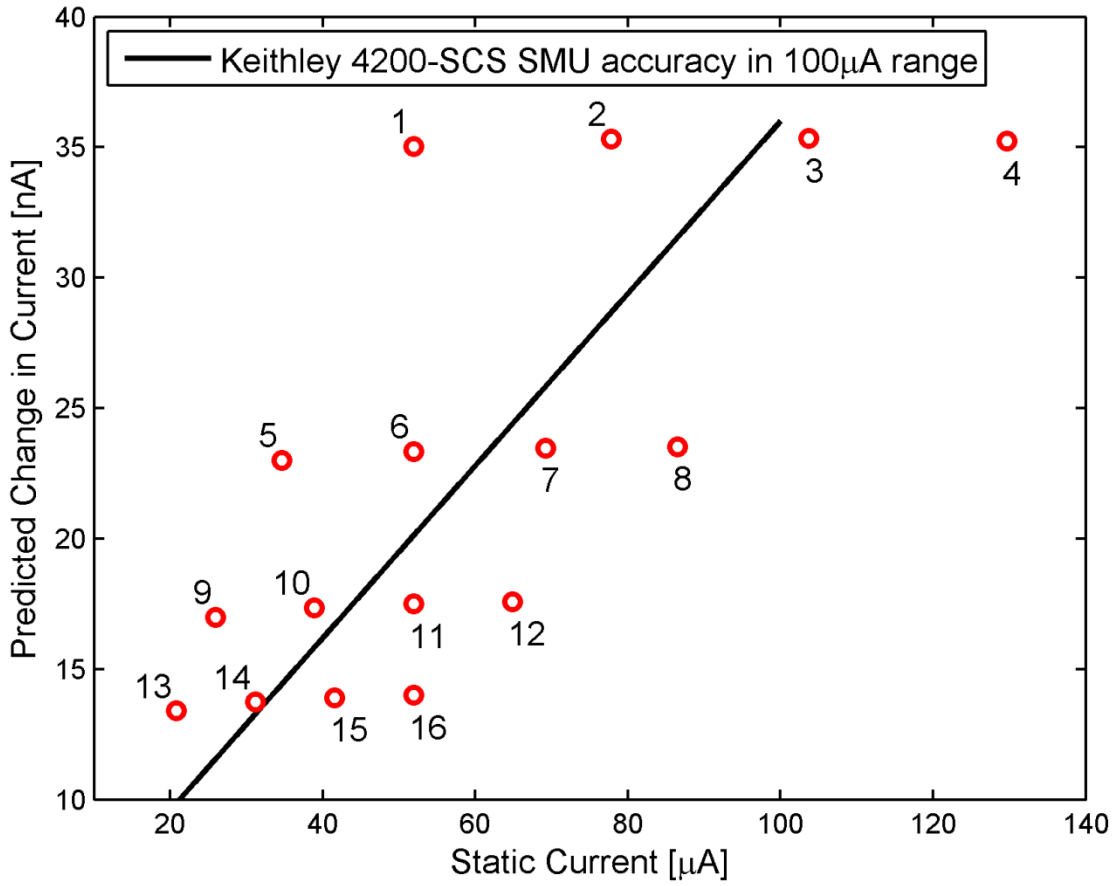

Figure 4.16: The predicted change in current and static current values of different device designs for 10 V SMU source voltage and 100 nN applied load plotted with the current measurement accuracy limit of the Keithley 4200-SCS SMU.

The measurement accuracy limit of the SMU refers to the minimum change in current that can be accurately measured. Note that this is not the measurement resolution which is a measure of precision. For the Keithley 4200-SCS medium power SMU, the values given in the datasheet (Table 4.5) show a linear dependence of the current measurement accuracy limit on the static current magnitude. The numbers 1 – 16 in Figure 4.16 correspond to the numbers of the different device designs. Each design has a different nanowire geometry, hence different response. The nanowire dimensions and the values of static current for 10 V supply, change in current due to an applied force of 100 nN, and the minimum force that can be accurately measured with the Keithley 4200-SCS SMU are listed in Table 4.6.

Device #	Nanowire length [μm]	Nanowire width [nm]	Static current for 10V [μA]	Current change for 100nN [nA]	Minimum force [nN]
1	2	100	51.9	35.0	57
2	2	150	77.8	35.3	81
3	2	200	103.7	35.3	188
4	2	250	129.7	35.2	213
5	3	100	34.6	23.0	63
6	3	150	51.9	23.4	86
7	3	200	69.2	23.5	110
8	3	250	86.5	23.5	134
9	4	100	25.9	17.0	68
10	4	150	38.9	17.4	91
11	4	200	51.9	17.5	115
12	4	250	64.8	17.6	139
13	5	100	20.8	13.4	74
14	5	150	31.1	13.7	97
15	5	200	41.5	13.9	120
16	5	250	51.9	14.0	144

Table 4.6: Nanowire dimensions, predicted current change and static current values, and the minimum force value that can be accurately measured with each different device design.

Evidently, nanowires with smaller cross-section provide better results. The device designs numbered 1, 2, 5, 6, 9, 10, 13, and 14 can be used to accurately measure an applied force of less than 100 nN. Unfortunately, in these designs, the nanowire widths are all smaller than 250 nm which is the smallest width that we can fabricate. Thus, these results are noted for future generation device designs should the technology to fabricate nanowires of smaller cross-section be available.

4.2. Sensor Fabrication

4.2.1. Fabrication Process Flow

For the fabrication of the MEMS traction sensor that we designed, we need access to sub-micrometer photolithography, and ion implantation. The only cleanroom facility in Turkey where we can fabricate these devices is the Semiconductor Technologies Research Laboratory (YITAL) of The Scientific and Technological Research Council of Turkey (TUBITAK). However, YITAL is geared towards complementary metal-oxide-semiconductor (CMOS) manufacturing. Due to this, we had to design a fabrication process flow for our MEMS sensor design that could be realized in a CMOS fabrication facility. Through regular meetings with the fabrication group at YITAL, we designed a fabrication process flow and started fabricating our sensor devices. The current fabrication process flow is detailed in this section, and the mask layout design is discussed in the following section.

As the substrate, we chose to use silicon-on-insulator (SOI) wafers for the fabrication of our sensors. SOI wafers have three different layers: a buried oxide (BOX) layer sandwiched between two silicon layers. The bottom silicon layer is a thick layer called the handle layer. The thinner top silicon layer is called the device layer where the devices are fabricated. The convenience of SOI wafers in MEMS fabrication is that the BOX layer acts as a natural etch stop, enabling precise control of device thickness. The specifications of the SOI wafers used in the fabrication process are listed in Table 4.7.

Diameter	100 mm
Orientation	(100)
Doping type	p-type (Boron)
Resistivity	20 – 30 Ωcm
Device layer thickness	2 ± 0.5 μm
Buried oxide thickness	2 μm ± 5%
Handle layer thickness	500 ± 10 μm

Table 4.7: Specifications of the SOI wafers used in fabrication.

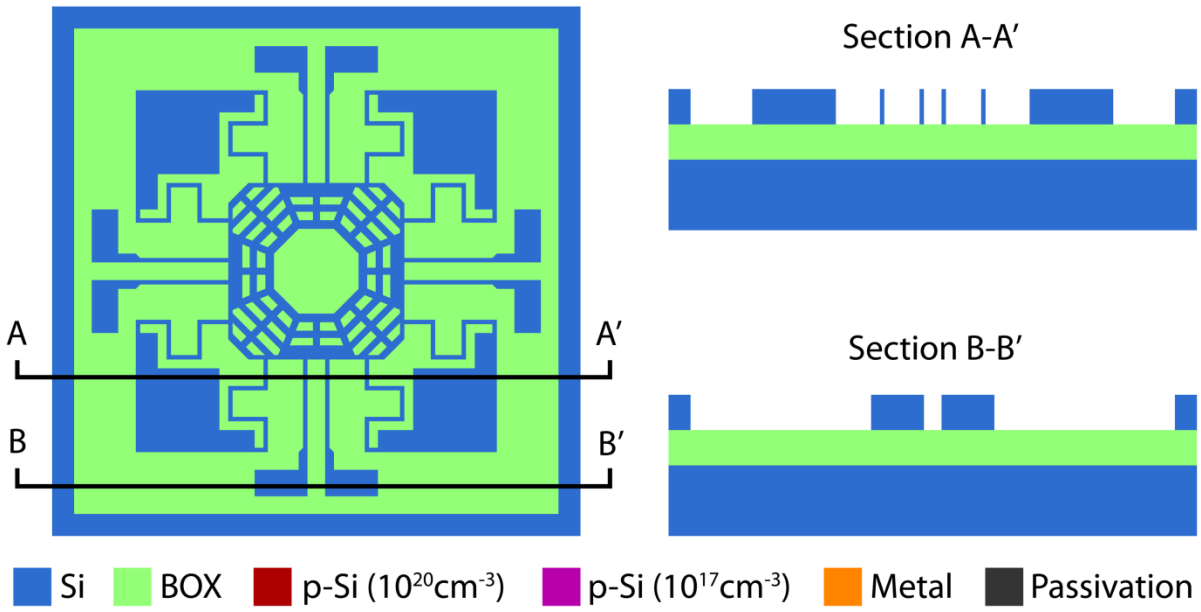

Figure 4.17: First silicon etch step where the anchors, springs, and the platform are defined and the nanowire bridge is outlined by a 2 µm RIE etch.

The first step in our fabrication process flow (Figure 4.17) is a reactive ion etching (RIE) process where the device layer is etched at a depth of 2 µm to define the platform and spring geometries, and outline the piezoresistor geometry. Note that the platform geometry shown in Figure 4.17 and the following figures is not a solid platform. It has etch holes that allow access to the underlying BOX layer. These etch holes are used for the release etching process which will be discussed below. The platform also has a large hole in the middle that is designed for characterization purposes (discussed in Section 4.4).

The next step in the fabrication flow (Figure 4.18) is a second RIE etching process where the geometry of the nanowire bridge is defined by reducing its thickness from 2 µm to 0.25 µm. The difference can be seen by comparing the cross-sectional views in Figure 4.17 and Figure 4.18. The first two etching steps are used to define the sensor geometry on the device layer.

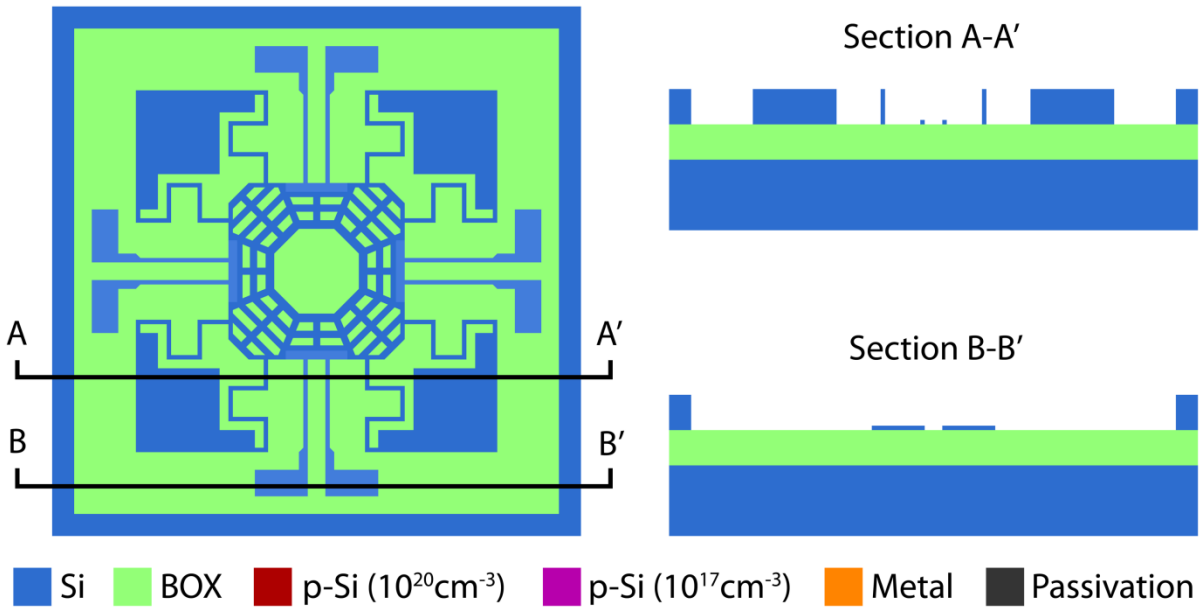

Figure 4.18: Second silicon etch step where the nanowire bridge thickness is reduced to 0.25 µm by a 1.75 µm RIE etch.

The third step is doping the piezoresistors by ion implantation (Figure 4.19). In this step, the piezoresistive nanowires and the metal contact pads are doped with Boron. The desired dopant concentration is 10^{17} cm^{-3} as per the design specifications discussed earlier.

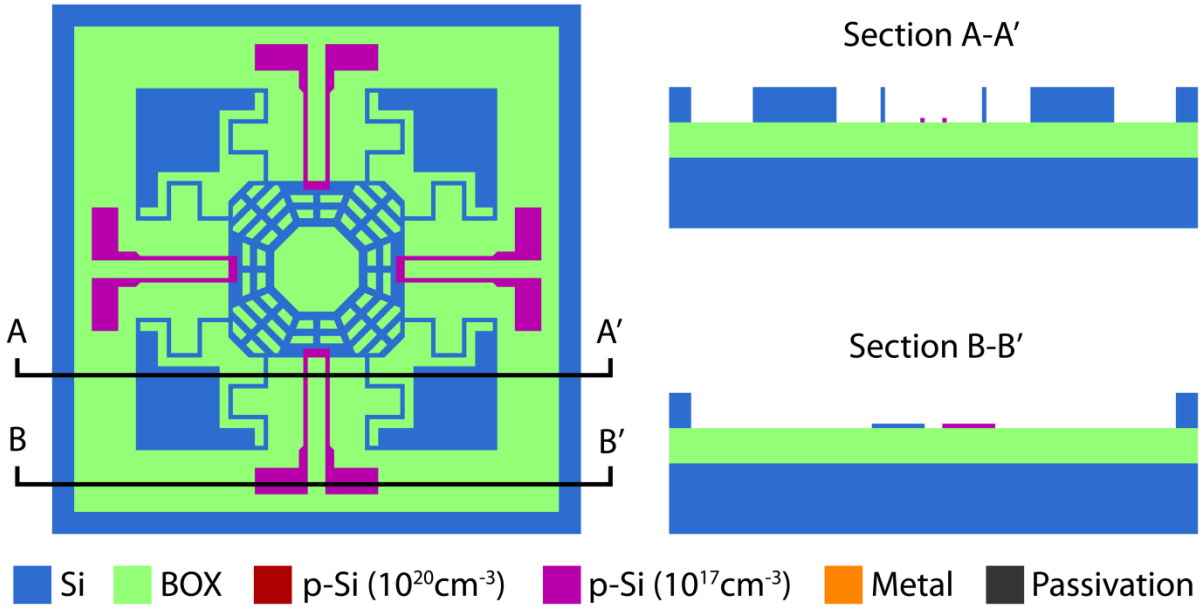

Figure 4.19: Doping of piezoresistive nanowires and metal contact pads with boron by ion implantation. A dopant concentration of 10^{17} is desired.

A second ion implantation step (Figure 4.20) is required for the doping of ohmic contact pads, since a high dopant concentration in p-type silicon is required to achieve good ohmic contact between doped silicon and metal [101]. A desired dopant concentration value of 10^{20} cm^{-3} was chosen. In this step, the unstrained portion of the nanowire bridge on the platform was also doped with high concentration in order to reduce the resistance of this portion. Note that in Figure 4.20 only half the pads are shown to be doped at high concentration. This is because in sensor array design, Schottky diodes are used with the nanowire bridges. In order to have a good Schottky contact between p-type doped silicon and metal, the dopant concentration of silicon needs to be low [101].

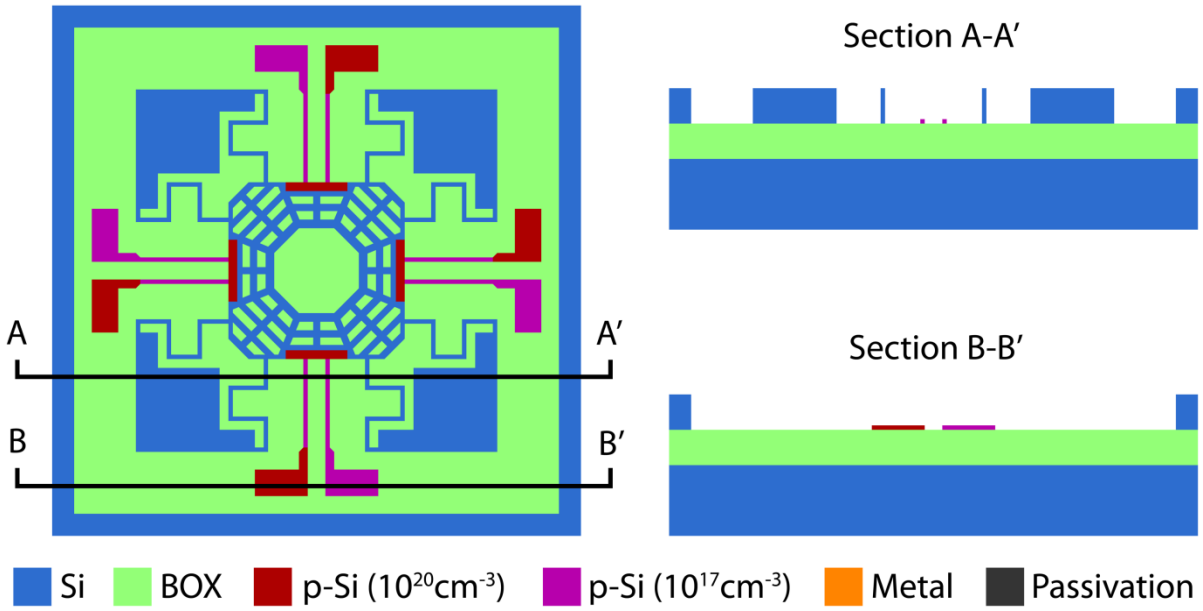

Figure 4.20: Doping of ohmic contact pads and unstrained piezoresistors with boron by ion implantation. In these regions, a dopant concentration of 10^{20} is desired.

Once the silicon etching and ion implantation steps are completed, the next step is metallization (Figure 4.21). We originally proposed to use the lift-off method for metal deposition, but the metal deposition process used by the fabrication group at YITAL does not allow for this technique. CMOS circuitry that the fabrication group works on requires very high purity metal, therefore their metal deposition processes are carried out at very low pressures (down to several nanoTorrs) with very tight humidity and contamination control. In the lift-off method, metal is deposited onto a sacrificial photoresist layer. Since placing photoresist coated wafers into the metal deposition chambers would increase the humidity and contamination, and create problems for the CMOS metallization processes, we could not use

lift-off for metal deposition. Instead, the proposed method for metallization is to first coat the entire wafer surface with metal using sputtering, and then use photolithography and metal etching to pattern the deposited metal layer. The commonly used choice of metal in YITAL is aluminum with a thin titanium seed layer to promote adhesion.

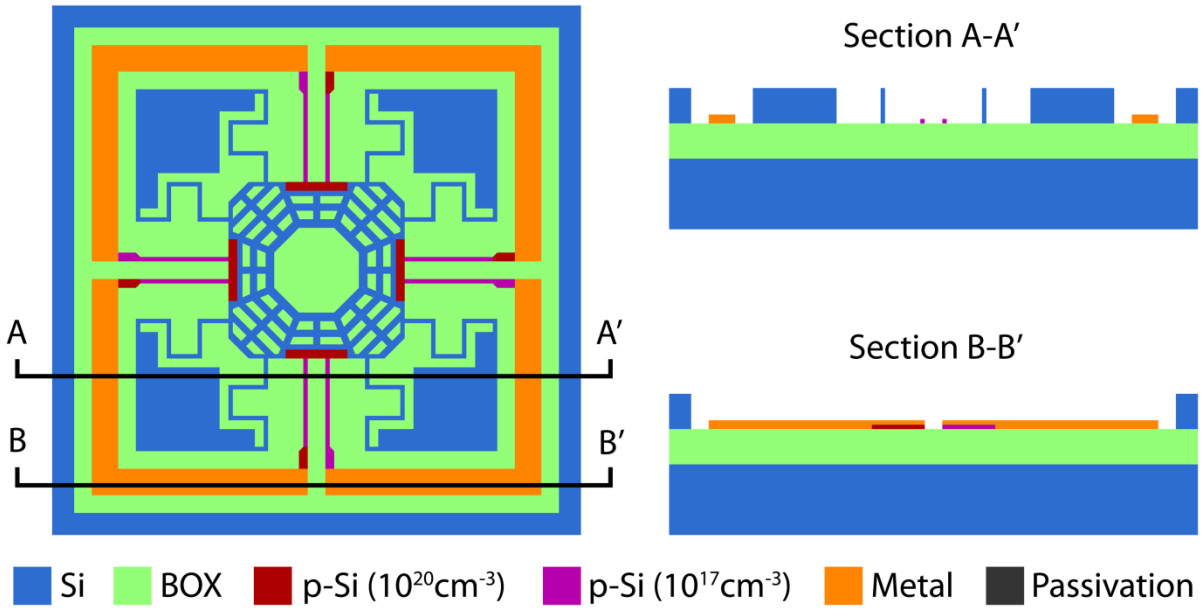

Figure 4.21: Metallization by sputtering and etching. Metal is first sputtered onto the entire wafer surface, and then it is patterned by etching.

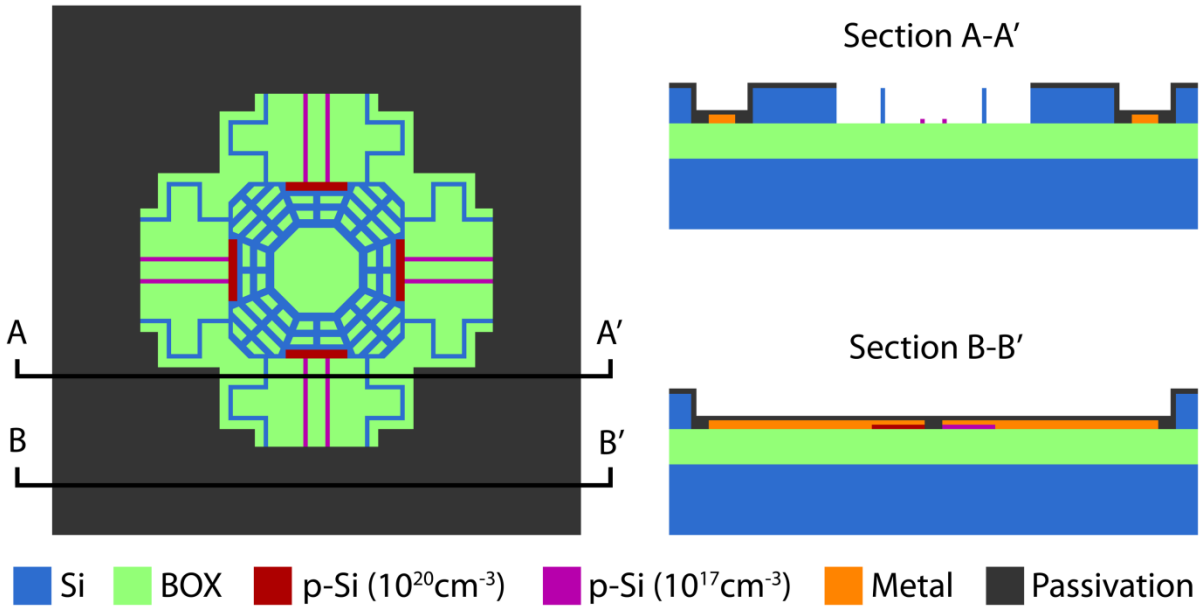

Figure 4.22: Passivation by polymer coating.

After metallization, the subsequent step is passivation (Figure 4.22). A passivation coating is needed for two reasons both related to the release etch step. In release etching, hydrofluoric acid (HF) is going to be used to etch the buried oxide layer under the platform, springs, and nanowires. Since HF also attacks aluminum and titanium, the metal layers need to be protected from HF exposure [102-104]. The second reason for passivation is to protect the exposed oxide that is not meant to be etched. A polymer coating is preferred for passivation since polymers can be deposited at low temperatures, and they can also be removed by dry methods such as oxygen plasma ashing [105].

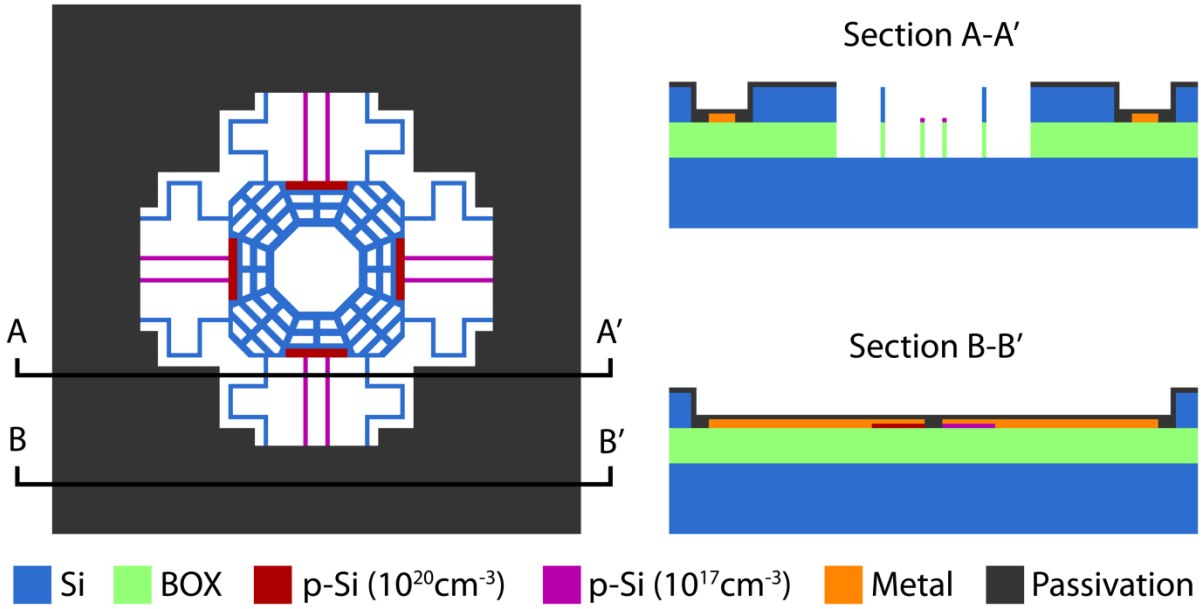

Figure 4.23: Buried oxide etching by Freon RIE prior to release.

The next step in the fabrication process flow is the anisotropic etching of the exposed buried oxide by Freon RIE (Figure 4.23). This step is carried out to remove the bulk of the buried oxide prior to HF vapor release (Figure 4.24). HF vapor etching is used for the release step because it prevents stiction [106]. Stiction is observed when suspended structures are released by aqueous etchants. If proper drying methods are not implemented, the capillary forces exerted by the fluid between the suspended structure and the handle layer pull the suspended structures down towards the handle layers, and eventually cause them to stick together permanently [103, 105, 106]. Release etching by vapor phase HF is one of the solutions to the stiction problem [106], and since this was a technique available to us, we decided to use HF vapor etching for the release process.

Directional etching of the exposed buried oxide by Freon RIE (Figure 4.23) prior to HF vapor release is critical for reducing the duration of the latter process. It is important that the duration of HF vapor exposure be minimized for two reasons. One reason is that the polymer passivation coating may detach from the substrate after prolonged exposure to HF [104] and the acid may leak and corrode the protected metal. The second reason is that although the etch rate of silicon in HF is much less than that of silicon dioxide; it still has a finite value. In other words, if we wait long enough, the silicon structures can also be etched considerably by HF.

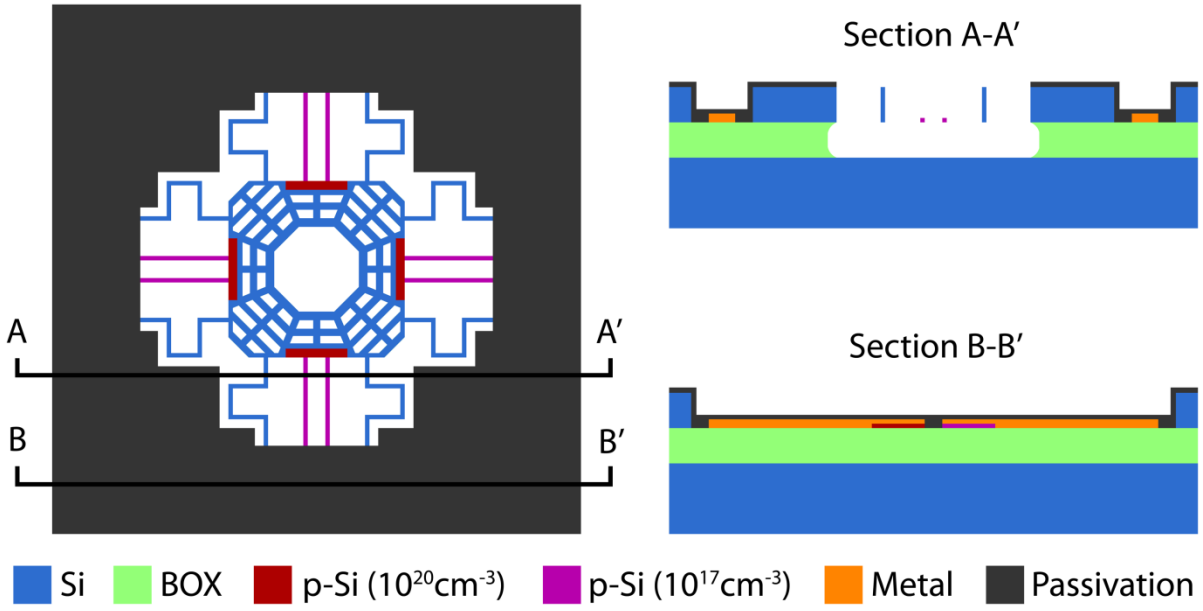

Figure 4.24: HF vapor release.

One step of the fabrication process flow that is not shown schematically is dicing where the individual dies are removed from the wafer using a motorized cutter. The dicing process is carried out after BOX etching by Freon RIE and before HF vapor release. All processes prior to dicing are wafer-level processes, *i.e.* the entire wafer is subjected to the same process. After dicing, the fabrication processes are on the die level. Dicing is done prior to HF release because HF release is a time controlled and challenging process which may take several trials before the process parameters are optimized. It is therefore a much better approach to carry out release etching on the die level since a failed attempt will only cost a single die whereas if release etching is performed on the wafer level, a failed attempt will cost the entire wafer.

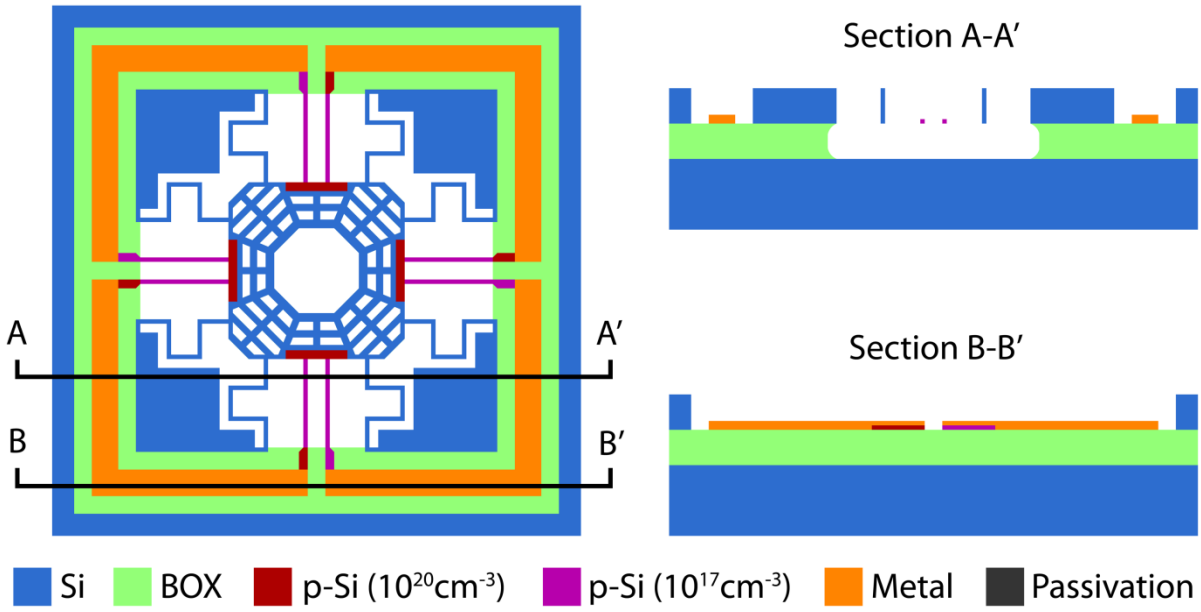

Figure 4.25: Removal of passivation layer by O_2 plasma ashing to gain access to metal contacts.

The final step in the fabrication process flow is the removal of the polymer passivation layer by oxygen plasma ashing. This procedure is done in order to gain access to the metal connections.

After the photolithography mask layouts were designed (as discussed in the following section) and fabricated, we started the fabrication of the MEMS sensor. The first silicon etch step (Figure 4.17) was performed by the fabrication group at YITAL, and the resulting structure is shown in Figure 4.26. Using the fabrication recipe they developed for the first RIE silicon etch step, the fabrication group were able to achieve an etch depth of 1.9 μm and a sidewall angle of 89.7°. The in-plane dimensions, however, were off by approximately 16% from the desired values. This error is attributed to the patterning of the hard etch mask, and can be solved by adjusting photolithography process parameters.

Note that small etch holes arranged in a rectangular array fashion (see Figure 4.26) are used instead of the spider-web shaped etch hole configuration illustrated in Figures 4.17–25. This change was due to the difficulties encountered with the spider-web shaped design during the mask writing stage. Rectangular arrays of small etch holes were more convenient for photolithography considerations.

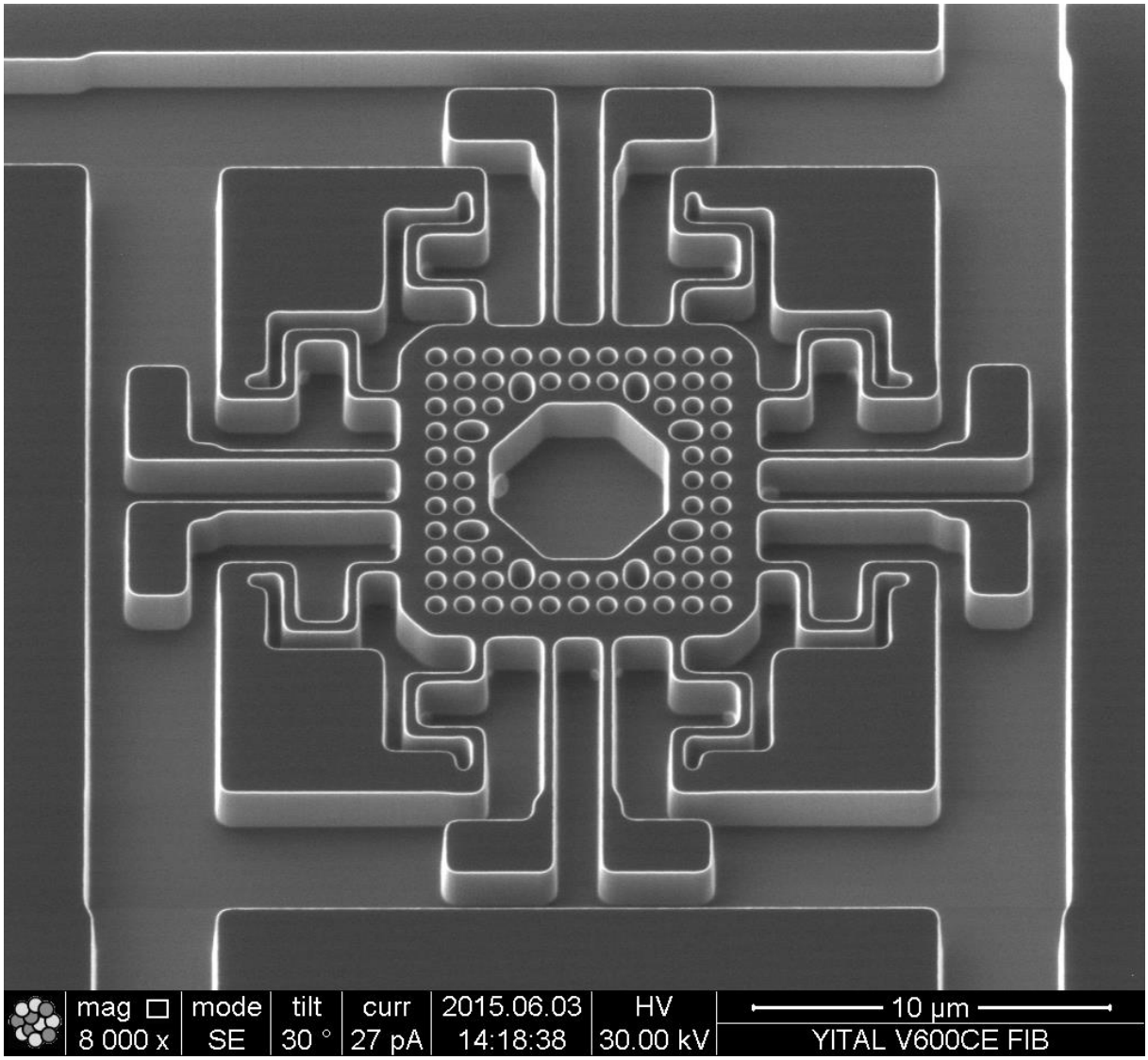

Figure 4.26: FIB micrograph of the structure fabricated by the first RIE silicon etch step.

4.2.2. Mask Layout Design

In the fabrication of our MEMS sensor design, a stepper device is used in the photolithography processes. A stepper is a device that is used to selectively expose the photoresist coated wafer to UV light. In a stepper, the photolithography mask is called a reticle which has one or more individual chip designs on it. The same reticle pattern is transferred onto the wafer repeatedly by scanning the wafer surface step by step. This photolithography method is suitable for mass production where a single design is fabricated in multitude. In the alternate approach, the aligner, the photolithography mask has the same size as the wafer and the entire wafer is exposed at once.

The photolithography mask layouts were designed using the L-Edit layout editor software. We focused on the selection of different device designs that we wanted to fabricate in the first prototype run, and the design of useful test structures.

In terms of device design, devices having different nanowire dimensions were selected to examine the effects of nanowire dimensions on sensor performance. Among the designs listed in Table 4.6, only the four designs having nanowire widths of 250 nm were selected since the other designs could not be fabricated. To be able to assess the effect of nanowire width on sensor performance, values ranging from 250 nm to 550 nm were used instead. Although the results in Figure 4.16 imply that we may not be able to use these designs to measure forces smaller than 100 nN, they will still work well at higher force ranges, enabling the investigation of the effect of nanowire cross-section on sensor performance.

Three different designs were developed regarding the electrical readout connections. These designs are shown in Figure 4.27. In the first electrical readout scheme (Figure 4.27a), all terminals of the nanowire bridges make ohmic contact with the metal lines and each piezoresistor is addressed independently; requiring 8 connections. The second design (Figure 4.27b) has on-chip Wheatstone bridge circuits for each piezoresistor to compensate for thermal drift; requiring 16 connections. In the third design (Figure 4.27c), each piezoresistor has one ohmic contact and one Schottky contact. This configuration is equivalent to a resistor connected in series with a Schottky diode. Such an electrical connection scheme enables multiplexing the piezoresistors which reduces the number of connections to 4 while each piezoresistor can still be addressed individually. The multiplexing scheme is a convenient approach for the electrical connection of an array of sensors as we will discuss further in Section 4.4.

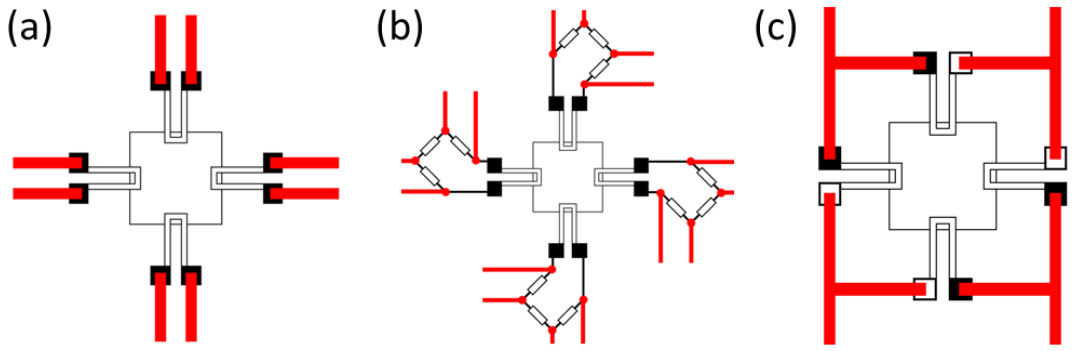

Figure 4.27: Electrical readout connection schemes for sensors with no diodes and no Wheatstone bridge (a), sensors with on-chip Wheatstone bridge (b), and sensors with Schottky diodes (c).

A device without springs was also included in the layout for experimental investigation of the effect of springs on sensor performance. In this device design, nanowire length and width were 5 μm and 250 nm, respectively.

Several test structure designs were also incorporated in the fabrication mask layout. One of these test structures is the cross-bridge resistor which is intended to be used to measure the resistivity of doped layers using the van der Pauw method. This test structure and measurement method is well established commonly employed in semiconductor technology [107-109]. Another group of test structures include individual nanowires of different dimensions both suspended (released) and anchored. These will be used for the I-V characterization of individual nanowires. Similarly, individual Schottky diodes having different silicon-metal contact areas were also included in the mask layout. These test structures are to be used for the I-V characterization of the diodes. In addition to these, we also designed test structures to investigate the effect of cross-talk between different nanowire bridges through the interaction platform. Even though the resistivity of the device layer is two orders of magnitude higher than the resistivity of the doped piezoresistors, there may still be cross-talk between the different piezoresistors through the platform. To investigate this effect, test structures that consist of only an anchored platform and four piezoresistor bridges and a reference piezoresistor were added to the layout.

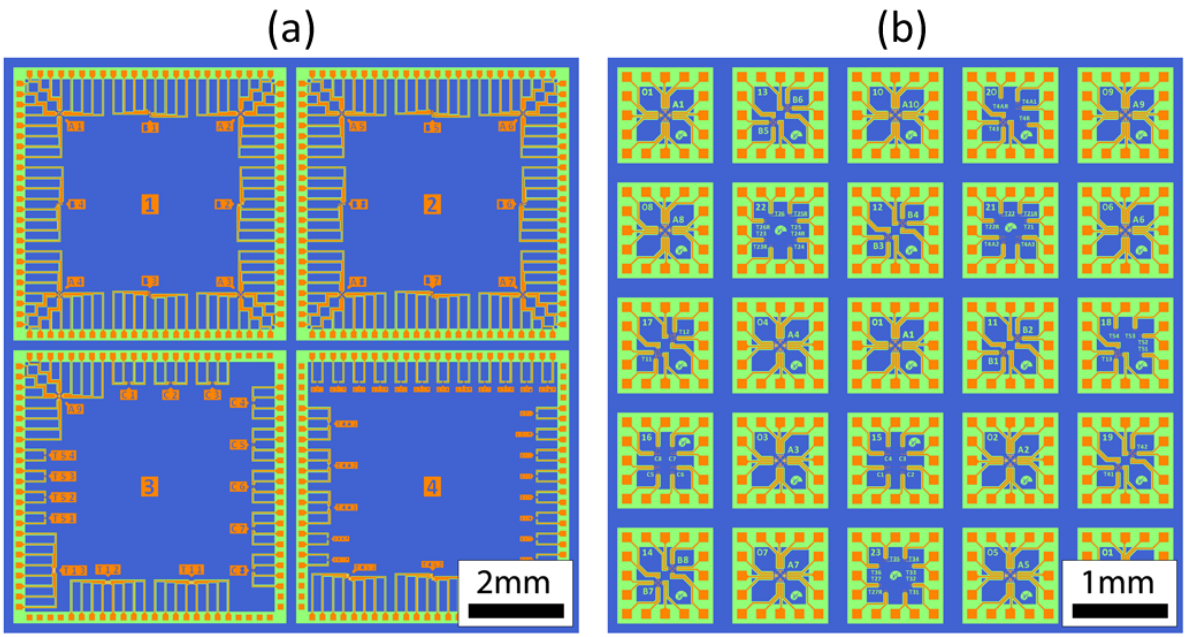

Figure 4.28: A comparison of the initial (a) and the revised (b) mask layout design.

A comparison of our initial and revised photomask layout designs are shown in Figure 4.28. Initially, we had four 5x5 mm chips with all the metal pads located at the periphery of the chip. The flaw of the initial layout design was that considerable space at the central region of the chips was left unused. In photolithography, the central regions usually have higher yield compared to the edges. To utilize this space better, and increase packing density, we decreased the size of the chips and increased the number of chips. The revised design is shown in Figure 4.28b. The same number of devices and test structures are present in the old and revised layout designs but the revised design covers a quarter of the space that the initial design took. The revised design is core-limited whereas the initial design was pad-limited.

4.3. Characterization

To characterize the fabricated MEMS sensors, a traction force of known magnitude and directions must be applied to the sensor and the sensor response should be measured. This can be done using a calibrated force sensor. For the solid platform geometry shown in Figure 4.11, it is very difficult to apply a force parallel to the top surface since the tip of the manipulator would slip. Moreover, the dimensions of the platform (10x10x2 μm) are too small for most commercial force sensor tips to interact with. Due to the small size scale, we propose to use AFM cantilevers to calibrate our sensors. An octagonal hole was etched at the center of the platform for the AFM tip to go in and apply force on the platform. Figure 4.29 shows the sensor structure with etch holes and the octagonal hole with the preferred load application.

In terms of dimensional conformity, AFM is an appropriate choice for probing the sensor interaction platform. It is also possible to use AFM cantilevers to apply lateral forces of known magnitude [110, 111] as shown in Figure 4.29. For the characterization of our MEMS sensor design, we propose to use AFM tips to apply lateral forces on the platform and measure the resistance changes of the piezoresistive nanowire bridges using a semiconductor parameter analyzer SMU.

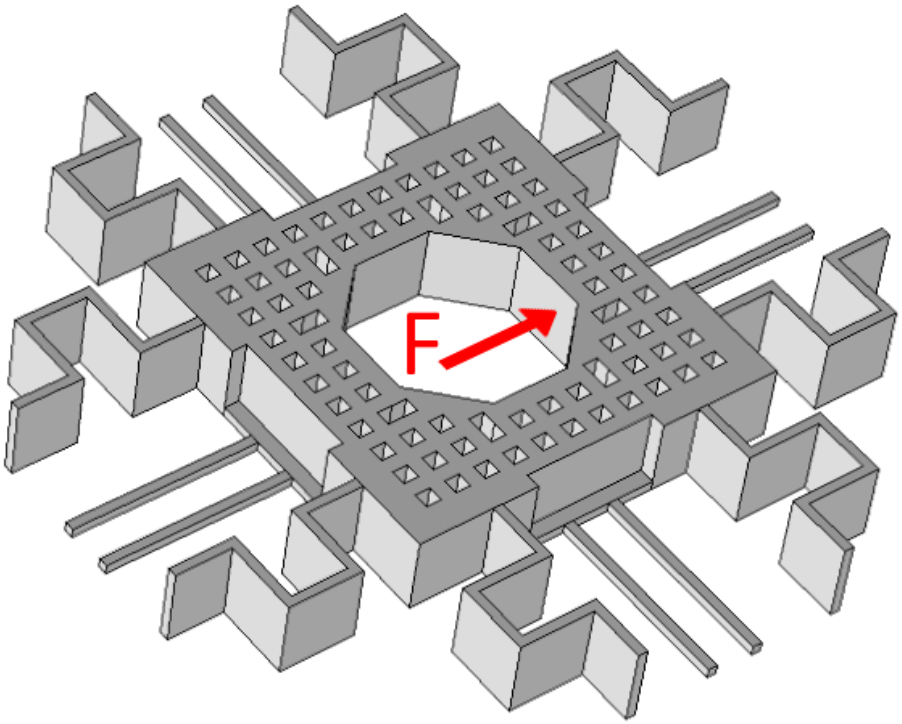

Figure 4.29: The fabricated sensor structure showing the load application preference for characterization.

4.4. 2D Sensor Array Design and Fabrication

Though the initial prototype design, fabrication, and characterization is focused on individual sensors, the long term objective of this study is to fabricate an array of MEMS traction sensors in order to measure the traction force fields between the surface and the adherent cells at multiple locations simultaneously. For future study, we propose a design and fabrication methodology for sensors in array configuration. The electromechanical design of the sensors in array configuration can be the same as the design for a single sensor which was detailed in Section 4.1. The electrical connections for a sensor array, however, are difficult. We propose a multiplexing scheme (Figure 4.30) in order to address each individual sensor in the array. The major advantage of the multiplexed configuration is the reduced number of electrical contacts and conducting metal lines that are required to address each sensor element in the array independently. This enables fabrication of compact arrays.

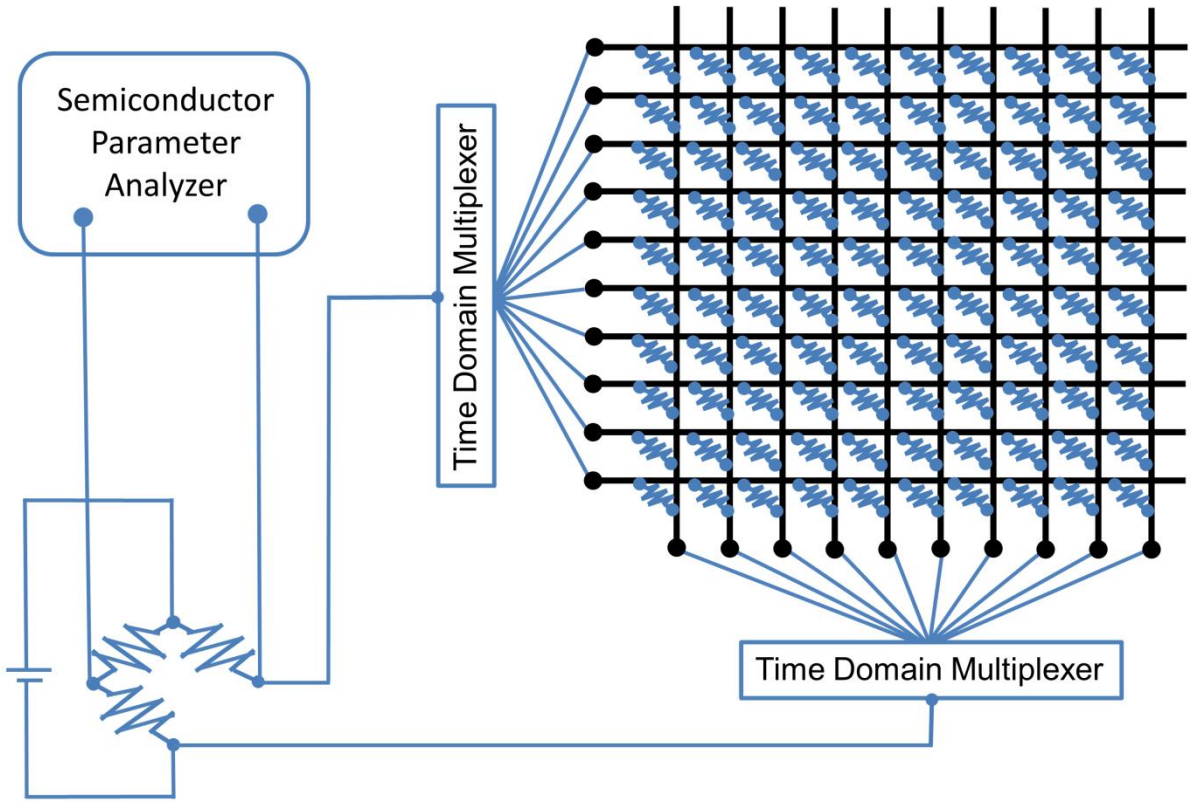

Figure 4.30: The proposed multiplexing scheme for the MEMS sensor array.

Schottky diodes should be added to the sensor design for them to be compatible with a multiplexing configuration. This can be done by having one contact pad of the nanowire bridge doped at low concentration, and the other doped at high concentration. The metal-silicon contact is ohmic for high doped p-type silicon and a Schottky contact is formed with low-doped silicon [101].

The fabrication process flow for a sensor array can be the same as that of a single sensor except for the metallization stage. The multiplexing configuration requires vertical and horizontal metal bus lines to make electrical connections with the sensors. This requires two levels of metallization with an insulation layer in between to prevent short circuits between the metal bus lines. We propose silicon dioxide for the insulation material due to its excellent properties as an insulator and its easy availability in the fabrication processes.

Chapter 5

CONCLUSION AND OUTLOOK

Two methods were developed for the study of cell mechanics and mechanics of cell-substrate interactions at the mesoscale and the microscale. The first method is the stretching of an elastomer substrate with adherent cells and investigating the effect of mechanical deformation on cells. A uniaxial tensile stretcher was designed and built that is compatible with inverted microscope setups. A linear stepper actuator with high displacement resolution was used to stretch the specimen while a load cell having 5N load capacity was used to measure the tension in the specimen. Two different types of PDMS specimens, one having a rectangular geometry, and the other having a dumbbell geometry were prepared with embedded fluorescent microspheres (beads). The samples were stretched while optical microscopy was used to record images of the specimens during stretching. The images were subsequently processed using MATLAB to track the positions of the fluorescent beads and calculate the local displacement and strain fields. The local values of longitudinal, lateral, and shear strain components were calculated.

The average local value of longitudinal strain measured by the present technique was compared with the applied cross-head strain for the two different specimen geometries. It was shown that for the rectangular specimens, the local and cross-head strains overlap, indicating a uniform strain distribution as expected. However, the magnitudes of local strain and local strain rate were shown to be higher than those of applied cross-head strain for dumbbell shaped specimens. These findings agree with the expectations regarding spatial strain distribution in these specimen geometries, and help illustrate the strength and importance of the present method. The measurement of local strain is needed to establish accurate correlations between mechanical deformation and cell response in cell mechanics studies that are based on substrate stretching.

The second method that was developed in this study for the investigation of mechanics of cells and cell-substrate interactions is based on a MEMS traction force sensor. A MEMS force sensor was designed using piezoresistive silicon nanowires as electromechanical transducers. The piezoresistance effect and the piezoresistive properties of silicon were reviewed for establishing fundamental design specifications. The effects of semiconductor doping type and dopant concentration, crystal orientation, and temperature on the sensitivity of silicon piezoresistors were examined. P-type doped silicon nanowire piezoresistors with a dopant concentration of 10^{17} cm^{-3} oriented along the <110> crystallographic directions were preferred for optimum performance and compliance with fabrication constraints.

The structural design of the MEMS traction sensor was carried out with focus on maximizing the effectiveness of the transmission of applied force onto the piezoresistors while maintaining a uniaxial stress-state in the nanowires. Finite element modelling was done using COMSOL Multiphysics® software to predict the mechanical response of the device designs. A sensor design comprising a suspended interaction platform anchored through piezoresistive nanowires and retaining springs was established. The spring geometry was optimized for preventing the out-of-plane tilting motion of the platform while maintaining low in-plane stiffness for effective transmission of applied force onto the nanowires. Using the presented device design, the magnitude and in-plane direction of applied force can be detected by the nanowires that are loaded in a stress-state that deviates by less than 1% from uniaxial tension or compression.

Suitable fabrication process flow and layout designs were developed in collaboration with the fabrication team at the Semiconductor Technologies Research Laboratory (YITAL) of The Scientific and Technological Research Council of Turkey (TUBITAK). The fabrication flow comprises the successive processes of reactive ion etching, doping by ion implantation, metallization, passivation, directional etching of buried oxide, dicing, HF vapor release, and passivation layer removal. The fabrication layout design consists of 25 chips having dimensions of 1 mm x 1mm that have different device and test structure designs. Fabrication stage of the MEMS sensor is currently in progress, and the initial result from the first silicon etching step is presented. In this etching process, the sensor geometry is defined. Good control of thickness and side wall angle, and moderate control of in-plane dimensions are achieved.

In continuation of the work presented in this thesis, the uniaxial stretcher and fluorescent microscopy system is going to be used to study cell mechanics at the mesoscale.

We propose the utilization of dual color fluorescent microscopy for the simultaneous imaging of embedded fluorescent beads and the adherent cells to establish correlations between substrate deformation and the mechanical response of the cytoskeletal intermediate filament networks. Cell migration, morphology, and viability under mechanical deformation can also be studied using the uniaxial stretcher and fluorescent microscopy.

For the characterization of the MEMS sensors which will be carried out once the sensors are fabricated, we propose the use of AFM method to apply lateral forces on the interaction platform and measure the resistance changes of the nanowires using a semiconductor parameter analyzer. For the long term objective of creating an array of MEMS traction sensors, the multiplexing scheme is recommended for electrical readout configuration and a double-pass metallization with silicon dioxide insulation is proposed for the fabrication of metal bus lines.

BIBLIOGRAPHY

[1] Y. Fung, *Biomechanics: Mechanical Properties of Living Tissues 2nd edn*. New York: Springer, 1993.

[2] Y. Fung, *Biomechanics: Circulation 2nd edn*. New York: Springer, 1997.

[3] A. J. Engler, S. Sen, H. L. Sweeney, and D. E. Discher, "Matrix Elasticity Directs Stem Cell Lineage Specification," *Cell*, vol. 126, pp. 677-689, 2006.

[4] T. Yeung, P. C. Georges, L. A. Flanagan, B. Marg, M. Ortiz, M. Funaki, *et al.*, "Effects of substrate stiffness on cell morphology, cytoskeletal structure, and adhesion," *Cell Motility and the Cytoskeleton*, vol. 60, pp. 24-34, 2005.

[5] J. Zheng, P. Lamoureux, V. Santiago, T. Dennerll, R. E. Buxbaum, and S. R. Heidemann, "Tensile regulation of axonal elongation and initiation," *The Journal of Neuroscience*, vol. 11, pp. 1117-1125, 1991.

[6] K. Franze, J. Gerdelmann, M. Weick, T. Betz, S. Pawlizak, M. Lakadamyali, *et al.*, "Neurite Branch Retraction Is Caused by a Threshold-Dependent Mechanical Impact," *Biophysical Journal*, vol. 97, pp. 1883-1890, 2009.

[7] P. C. Georges, W. J. Miller, D. F. Meaney, E. S. Sawyer, and P. A. Janmey, "Matrices with Compliance Comparable to that of Brain Tissue Select Neuronal over Glial Growth in Mixed Cortical Tissues," *Biophysical Journal*, vol. 90, pp. 3012-3018, 2006.

[8] C.-M. Lo, H.-B. Wang, M. Dembo, and Y.-l. Wang, "Cell Movement Is Guided by the Rigidity of the Substrate," *Biophysical Journal*, vol. 79, pp. 144-152, 2000.

[9] S. M. McCormick, S. G. Eskin, L. V. McIntire, C. L. Teng, C.-M. Lu, C. G. Russell, *et al.*, "DNA microarray reveals changes in gene expression of shear stressed human umbilical vein endothelial cells," *Proceedings of the National Academy of Sciences*, vol. 98, pp. 8955-8960, 2001.

[10] D. E. Ingber, "Mechanical Signaling and the Cellular Response to Extracellular Matrix in Angiogenesis and Cardiovascular Physiology," *Circulation Research*, vol. 91, pp. 877-887, 2002.

[11] C. Zhu, G. Bao, and N. Wang, "Cell Mechanics: Mechanical Response, Cell Adhesion, and Molecular Deformation," *Annual Review of Biomedical Engineering*, vol. 2, pp. 189-226, 2000.

[12] B. Morrison, K. E. Saatman, D. F. Meaney, and T. K. McIntosh, "In Vitro Central Nervous System Models of Mechanically Induced Trauma: A Review," *Journal of Neurotrauma*, vol. 15, pp. 911-928, 1998.

[13] D. H. Smith, J. A. Wolf, and D. F. Meaney, "A New Strategy to Produce Sustained Growth of Central Nervous System Axons: Continuous Mechanical Tension," *Tissue Engineering*, vol. 7, pp. 131-139, 2001.

[14] P. Rakic, "Neuron-glia relationship during granule cell migration in developing cerebellar cortex. A Golgi and electronmicroscopic study in Macacus Rhesus," *The Journal of Comparative Neurology*, vol. 141, pp. 283-312, 1971.

[15] Y.-B. Lu, K. Franze, G. Siefert, C. Steinhauser, F. Kirchhoff, H. Wolburg, *et al.*, "Viscoelastic properties of individual glial cells and neurons in the CNS," *Proceedings of the National Academy of Sciences,* vol. 103, pp. 17759-17764, 2006.

[16] S. Siechen, S. Yang, A. Chiba, and T. Saif, "Mechanical tension contributes to clustering of neurotransmitter vesicles at presynaptic terminals," *Proceedings of the National Academy of Sciences,* vol. 106, pp. 12611-12616, 2009.

[17] S. Suresh, J. Spatz, J. P. Mills, A. Micoulet, M. Dao, C. T. Lim, *et al.*, "Connections between single-cell biomechanics and human disease states: gastrointestinal cancer and malaria," *Acta Biomaterialia,* vol. 1, pp. 15-30, 2005.

[18] M. L. Gardel, I. C. Schneider, Y. Aratyn-Schaus, and C. M. Waterman, "Mechanical Integration of Actin and Adhesion Dynamics in Cell Migration," *Annu Rev Cell Dev Biol.,* vol. 26, pp. 315-333, 2010.

[19] D. Wirtz, K. Konstantopoulos, and P. C. Searson, "The physics of cancer: the role of physical interactions and mechanical forces in metastasis," *Nature Reviews Cancer,* vol. 11, pp. 512-522, 2011.

[20] V. Vogel and M. P. Sheetz, "Cell fate regulation by coupling mechanical cycles to biochemical signaling pathways," *Current Opinion in Cell Biology,* vol. 21, pp. 38-46, 2009.

[21] G. B. Blanchard and R. J. Adams, "Measuring the multi-scale integration of mechanical forces during morphogenesis," *Current Opinion in Genetics & Development,* vol. 21, pp. 653-663, 2011.

[22] M.-A. Bray, S. P. Sheehy, and K. K. Parker, "Sarcomere alignment is regulated by myocyte shape," *Cell Motility and the Cytoskeleton,* vol. 65, pp. 641-651, 2008.

[23] N. A. Geisse, M. A. Bray, S. P. Sheehy, B. P. Olding, P. J. Wolfe, and K. K. Parker, "Cytoskeletal structure and Ca2+ spark localization in engineered cardiac myocytes," *European Heart Journal,* vol. 27, pp. 30-30, 2006.

[24] K. M. Stroka and H. Aranda-Espinoza, "A biophysical view of the interplay between mechanical forces and signaling pathways during transendothelial cell migration," *FEBS Journal,* vol. 277, pp. 1145-1158, 2010.

[25] K. M. Stroka and H. Aranda-Espinoza, "Endothelial cell substrate stiffness influences neutrophil transmigration via myosin light chain kinase-dependent cell contraction," *Blood,* vol. 118, pp. 1632-1640, 2011.

[26] A. Pathak and S. Kumar, "Independent regulation of tumor cell migration by matrix stiffness and confinement," *Proceedings of the National Academy of Sciences,* vol. 109, pp. 10334-10339, 2012.

[27] T. Mammoto and D. E. Ingber, "Mechanical Control of tissue and organ development," *Development,* vol. 137, pp. 1407-1420, 2010.

[28] D. E. Discher, P. Janmey, and Y.-l. Wang, "Tissue Cells Feel and Respond to the Stiffness of Their Substrate," *Science,* vol. 310, pp. 1139-1143, 2005.

[29] P. Friedl and K. Wolf, "Plasticity of cell migration: a multiscale tuning model," *Journal of Cell Biology,* vol. 188, pp. 11-19, 2010.

[30] M. Affolter and E. Caussinus, "Tracheal branching morphogenesis in Drosophila: new insights into cell behavior and organ architecture," *Development,* vol. 135, pp. 2055-2064, 2008.

[31] V. Vogel and M. Sheetz, "Local force and geometry sensing regulate cell functions," *Nature Reviews Molecular Cell Biology,* vol. 7, pp. 265-275, 2006.

[32] J. T. Parsons, A. R. Horwitz, and M. A. Schwartz, "Cell adhesion: integrating cytoskeletal dynamics and cellular tension," *Nature Reviews Molecular Cell Biology,* vol. 11, pp. 633-643, 2010.

[33] L. Trichet, J. L. Digabel, R. J. Hawkins, S. R. K. Vedula, M. Gupta, C. Ribrault, *et al.*, "Evidence of a large-scale mechanosensing mechanism for cellular adaptation to substrate stiffness," *Proceedings of the National Academy of Sciences,* vol. 109, pp. 6933-6938, 2012.

[34] B. T. Helfand, L. Chang, and R. D. Goldman, "Intermediate filaments are dynamic and motile elements of cellular architecture," *Journal of Cell Science,* vol. 117, pp. 133-141, 2004.

[35] H. Herrmann, H. Bar, L. Kreplak, S. V. Strelkov, and U. Aebi, "Intermediate filaments: from cell architecture to nanomechanics," *Nature Reviews Molecular Cell Biology,* vol. 8, pp. 562-573, 2007.

[36] D. A. Figlewicz, A. Krizus, M. G. Martinoli, V. Meininger, M. Dib, G. A. Rouleau, *et al.*, "Variants of the heavy neurofilament subunit are associated with the development of amyotrophic lateral sclerosis," *Human Molecular Genetics,* vol. 3, pp. 1757-1761, 1994.

[37] A. Al-Chalabi and C. C. J. Miller, "Neurofilaments and neurological disease," *BioEssays,* vol. 25, pp. 346-355, 2003.

[38] C. Lavedan, S. Buchholtz, R. L. Nussbaum, R. L. Albin, and M. H. Polymeropoulos, "A mutation in the human neurofilament M gene in Parkinson's disease that suggests a role for the cytoskeleton in neuronal degeneration," *Neuroscience Letters,* vol. 322, pp. 57-61, 2002.

[39] A. Jordanova, P. D. Jonghe, C. F. Boerkoel, H. Takashima, E. D. Vriendt, C. Ceuterick, *et al.*, "Mutations in the neurofilament light chain gene (NEFL) cause early onset severe Charcot-Marie-Tooth disease," *Brain,* vol. 126, pp. 590-597, 2003.

[40] S. V. Strelkov, H. Herrmann, and U. Aebi, "Molecular architecture of intermediate filaments," *BioEssays,* vol. 25, pp. 243-251, 2003.

[41] S. Ackerley, P. Thornhill, A. J. Grierson, J. Brownlees, B. H. Anderton, P. N. Leigh, *et al.*, "Neurofilament heavy chain side arm phosphorylation regulates axonal transport of neurofilaments," *Journal of Cell Biology,* vol. 161, pp. 489-495, 2003.

[42] B. T. Helfand, L. Chang, and R. D. Goldman, "The dynamic and motile properties of intermediate filaments," *Annual Review of Cell and Developmental Biology,* vol. 19, pp. 445-467, 2003.

[43] B. T. Helfand, P. Loomis, M. Yoon, and R. D. Goldman, "Rapid transport of neural intermediate filament protein," *Journal of Cell Science,* vol. 116, pp. 2345-2359, 2003.

[44] J. R. Marszalek, T. L. Williamson, M. K. Lee, Z. Xu, P. N. Hoffman, M. W. Becher, *et al.*, "Neurofilament subunit NF-H modulates axonal diameter by selectively slowing neurofilament transport," *Journal of Cell Biology,* vol. 135, pp. 711-724, 1996.

[45] Y.-H. Chou and R. D. Goldman, "Intermediate Filaments on the Move," *Journal of Cell Biology,* vol. 150, pp. F101-F106, 2000.

[46] L. L. Norman, K. Stroka, and H. Aranda-Espinoza, "Guiding Axons in the Central Nervous System: A Tissue Engineering Approach," *Tissue Engineering Part B: Reviews,* vol. 15, pp. 291-305, 2009.

[47] R. D. Goldman, Y.-H. Chou, V. Prahlad, and M. Yoon, "Intermediate filaments: dynamic processes regulating their assembly, motility, and interactions with other cytoskeletal systems," *The FASEB Journal,* vol. 13, pp. S261-S265, 1999.

[48] H. Herrmann and U. Aebi, "Intermediate filaments and their associates: multi-talented structural elements specifying cytoarchitecture and cytodynamics," *Current Opinion in Cell Biology,* vol. 12, pp. 79-90, 2000.

[49] M. B. Omary, N.-O. Ku, G.-Z. Tao, D. M. Toivola, and J. Liao, "'Heads and tails' of intermediate filament phosphorylation: multiple sites and functional insights," *Trends in Biochemical Sciences,* vol. 31, pp. 383-394, 2006.

[50] D. Wlodkowic, S. Faley, M. Zagnoni, J. P. Wikswo, and J. M. Cooper, "Microfluidic Single-Cell Array Cytometry for the Analysis of Tumor Apoptosis," *Analytical Chemistry,* vol. 81, pp. 5517-5523, 2009.

[51] S. E. Cross, Y.-S. Jin, J. Rao, and J. K. Gimzewski, "Nanomechanical analysis of cells from cancer patients," *Nature Nanotechnology,* vol. 2, pp. 780-783, 2007.

[52] D.-H. Kim, P. K. Wong, J. Park, A. Levchenko, and Y. Sun, "Microengineered Platforms for Cell Mechanobiology," *Annual Review of Biomedical Engineering,* vol. 11, pp. 203-233, 2009.

[53] N. J. Sniadecki, A. Anguelouch, M. T. Yang, C. M. Lamb, Z. Liu, S. B. Kirschner, *et al.*, "Magnetic microposts as an approach to apply forces to living cells," *Proceedings of the National Academy of Sciences,* vol. 104, pp. 14553-14558, 2007.

[54] G. Bao and S. Suresh, "Cell and molecular mechanics of biological materials," *Nature Materials,* vol. 2, pp. 715-725, 2003.

[55] O. Loh, A. Vaziri, and H. D. Espinosa, "The Potential of MEMS for Advancing Experiments and Modeling in Cell Mechanics," *Experimental Mechanics,* vol. 49, pp. 105-124, 2009.

[56] M. Raoux, L. Rodat-Despoix, N. Azorin, A. Giamarchi, J. Hao, F. Maingret, *et al.*, "Mechanosensor Channels in Mammalian Somatosensory Neurons," *Sensors,* vol. 7, pp. 1667-1682, 2007.

[57] O. d. Roure, A. Saez, A. Buguin, R. H. Austin, P. Chavrier, P. Siberzan, *et al.*, "Force mapping in epithelial cell migration," *Proceedings of the National Academy of Sciences,* vol. 102, pp. 2390-2395, 2005.

[58] J. L. Tan, J. Tien, D. M. Pirone, D. S. Gray, K. Bhadriraju, and C. S. Chen, "Cells lying on a bed of microneedles: An approach to isolate mechanical force," *Proceedings of the National Academy of Sciences,* vol. 100, pp. 1484-1489, 2003.

[59] S. Yang and M. T. A. Saif, "Force response and actin remodeling (agglomeration) in fibroblasts due to lateral indentation," *Acta Biomaterialia,* vol. 3, pp. 77-87, 2007.

[60] D. B. Serrell, T. L. Oreskovic, A. J. Slifka, R. L. Mahajan, and D. S. Finch, "A uniaxial bioMEMS device for quantitative force-displacement measurements," *Biomedical Microdevices,* vol. 9, pp. 267-275, 2007.

[61] G. Lin, K. S. J. Pister, and K. P. Roos, "Surface Micromachined Polysilicon Heart Cell Force Transducer," *Journal of Microelectromechanical Systems,* vol. 9, pp. 9-17, 2000.

[62] G. Lin, V. I. Wu, R. E. Hainley, L. A. Flanagan, E. S. Monuki, and W. C. Tang, "Development of a MEMS Microsystem to Study the Effect of Mechanical Tension on Cerebral Cortex Neurogenesis," in *Proceedings of the 26th Annual International Conference of the IEEE EMBS,* San Francisco, CA, USA, 2004.

[63] K. J. V. Vliet, G. Bao, and S. Suresh, "The biomechanics toolbox: experimental approaches for living cells and biomolecules," *Acta Materialia,* vol. 51, pp. 5881-5905, 2003.

[64] S. J. Eppell, B. N. Smith, H. Kahn, and R. Ballarini, "Nano measurements with micro-devices: mechanical properties of hydrated collagen fibrils," *Journal of the Royal Society Interface,* vol. 3, pp. 117-121, 2006.

[65] N. Scuor, P. Gallina, H. V. Panchawagh, R. L. Mahajan, O. Sbaizero, and V. Sergo, "Design of a novel MEMS platform for the biaxial stimulation of living cells," *Biomedical Microdevices,* vol. 8, pp. 239-246, 2006.

[66] Y. Sun, B. J. Nelson, D. P. Potasek, and E. Enikov, "A bulk microfabricated multi-axis capacitive cellular force sensor using transverse comb drive," *Journal of Micromechanics and Microengineering,* vol. 12, pp. 832-840, 2002.

[67] M. Li, H. X. Tang, and M. L. Roukes, "Ultra-sensitive NEMS-based cantilevers for sensing, scanned probe and very high-frequency applications," *Nature Nanotechnology,* vol. 2, pp. 114-120, 2007.

[68] M. R. Dusseiller, M. L. Smith, V. Vogel, and M. Textor, "Microfabricated three-dimensional environments for single cell studies," *Biointerphases,* vol. 1, pp. P1-P4, 2006.

[69] D. Sameoto, T. Hubbard, and M. Kujath, "Operation of electrothermal and electrostatic MUMPs microactuators underwater," *Journal of Micromechanics and Microengineering,* vol. 14, pp. 1359-1366, 2004.

[70] T. L. Sounart, T. A. Michalske, and K. R. Zavadil, "Frequency-Dependent Electrostatic Actuation in Microfluidic MEMS," *Journal of Microelectromechanical Systems,* vol. 14, pp. 125-133, 2005.

[71] K. Hayakawa, A. Hosokawa, K. Yabusaki, and T. Obinata, "Orientation of Smooth Muscle-Derived A10 Cells in Culture by Cyclic Stretching: Relationship between Stress Fiber Rearrangement and Cell Reorientation," *Zoological Science,* vol. 17, pp. 617-624, 2000.

[72] K. Naruse, T. Yamada, and M. Sokabe, "Involvement of SA channels in orienting response of cultured endothelial cells to cyclic stretch," *American Journal of Physiology,* vol. 274, pp. H1532-H1538, 1998.

[73] M. J. Yost, D. Simpson, K. Wrona, S. Ridley, H. J. Ploehn, T. K. Borg, *et al.*, "Design and construction of a uniaxial cell stretcher," *American Journal of Physiology - Heart and Circulatory Physiology,* vol. 279, pp. H3124-H3130, 2000.

[74] N. Bonakdar, J. Luczak, L. Lautscham, M. Czonstke, T. M. Koch, A. Mainka, *et al.*, "Biomechanical characterization of a desminopathy in primary human myoblasts," *Biochemical and Biophysical Research Communications,* vol. 419, pp. 703-707, 2012.

[75] A. J. W. McClung, G. P. Tandon, K. E. Goecke, and J. W. Baur, "Non-contact technique for characterizing full-field surface deformation of shape memory polymers at elevated and room temperatures," *Polymer Testing,* vol. 30, pp. 140-149, 2011.

[76] B. Pan, K. Qian, H. Xie, and A. Asundi, "Two-dimensional digital image correlation for in-plane displacement and strain measurement: a review," *Measurement Science and Technology,* vol. 20, 2009.

[77] J. Zhang, Y. Cai, W. Ye, and T. X. Yu, "On the use of the digital image correlation method for heterogeneous deformation measurement of porous solids," *Optics and Lasers in Engineering,* vol. 49, pp. 200-209, 2011.

[78] D. Tscharnuter, M. Jerabek, Z. Major, and R. W. Lang, "Time-dependent poisson's ratio of polypropylene compounds for various strain histories," *Mechanics of Time-Dependent Materials,* vol. 15, pp. 15-28, 2011.

[79] R. H. Pritchard, P. Lava, D. Debruyne, and E. M. Terentjev, "Precise determination of the Poisson ratio in soft materials with 2D digital image correlation," *Soft Matter,* vol. 9, pp. 6037-6045, 2013.

[80] D. Lecompte, A. Smits, S. Bossuyt, H. Sol, J. Vantomme, D. V. Hemelrijck, *et al.*, "Quality assesment of speckle patterns for digital image correlation," *Optics and Lasers in Engineering,* vol. 44, pp. 1132-1145, 2006.

[81] P. Lava, S. Cooreman, and D. Debruyne, "Study of systematic errors in strain fields obtained via DIC using heterogeneous deformation generated by plastic FEA," *Optics and Lasers in Engineering,* vol. 48, pp. 457-468, 2010.

[82] J. P. Butler, I. M. Tolic-Norrelykke, B. Fabry, and J. J. Fredberg, "Traction fields, moments, and strain energy that cells exert on their surroundings," *American Journal of Physiology - Cell Physiology,* vol. 282, pp. C595-C605, 2002.
[83] T. Dey, M. C. Mann, and W. H. Goldmann, "Comparing mechano-transduction in fibroblasts deficient of focal adhesion proteins," *Biochemical and Biophysical Research Communications,* vol. 413, pp. 541-544, 2011.
[84] E. Sollier, C. Murray, P. Maoddi, and D. D. Carlo, "Rapid prototyping polymers for microfluidic devices and high pressure injections," *Lab on a Chip,* vol. 11, pp. 3752-3765, 2011.
[85] F. Schneider, T. Fellner, J. Wilde, and U. Wallrabe, "Mechanical properties of silicones for MEMS," *Journal of Micromechanics and Microengineering,* vol. 18, 2008.
[86] J. Lubliner, *Plasticity Theory*. New York: Dover Publications, 2008.
[87] P. E. Allain, F. Parrain, A. Bosseboeuf, S. Maaroufi, P. Coste, and A. Walther, "Large-Range MEMS Motion Detection With Subangstrom Noise Level Using an Integrated Piezoresistive Silicon Nanowire," *Journal of Microelectromechanical Systems,* vol. 22, pp. 716-722, 2013.
[88] C. Liu, "Piezoresistive Sensors," in *Foundations of MEMS,* ed: Pearson Prentice Hall, 2005, pp. 207-244.
[89] A. A. Barlian, W.-T. Park, J. R. Mallon, A. J. Rastegar, and B. L. Pruitt, "Review: Semiconductor Piezoresistance for Microsystems," *Proceedings of the IEEE,* vol. 97, pp. 513-552, 2009.
[90] C. S. Smith, "Piezoresistance Effect in Germanium and Silicon," *Physical Review,* vol. 94, pp. 42-49, 1954.
[91] Y. Kanda, "A Graphical Representation of the Piezoresistance Coefficients in Silicon," *IEEE Transactions on Electron Devices,* vol. ED-29, pp. 64-70, 1982.
[92] M. A. Hopcroft, W. D. Nix, and T. W. Kenny, "What is the Young's Modulus of Silicon?," *Journal of Microelectromechanical Systems,* vol. 19, pp. 229-238, 2010.
[93] T. Toriyama and S. Sugiyama, "Analysis of Piezoresistance in p-Type Silicon for Mechanical Sensors," *Journal of Microelectromechanical Systems,* vol. 11, pp. 598-604, 2002.
[94] K. Matsuda, K. Suzuki, K. Yamamura, and Y. Kanda, "Nonlinear piezoresistance effects in silicon," *Journal of Applied Physics,* vol. 73, pp. 1838-1847, 1993.
[95] J. A. Harley and T. W. Kenny, "1/F Noise Considerations for the Design and Process Optimization of Piezoresistive Cantilevers," *Journal of Microelectromechanical Systems,* vol. 9, pp. 226-235, 2000.
[96] C.-H. Cho, R. C. Jaeger, and J. C. Suhling, "Characterization of the Temperature Dependence of the Piezoresistive Coefficients of Silicon From -150C to +125C," *IEEE Sensors Journal,* vol. 8, pp. 1455-1468, 2008.
[97] F. J. Morin, T. H. Geballe, and C. Herring, "Temperature Dependence of the Piezoresistance of High-Purity Silicon and Germanium," *Physical Review,* vol. 105, pp. 525-539, 1957.
[98] K. Yamada, M. Nishihara, S. Shimada, M. Tanabe, M. Shimazoe, and Y. Matsuoka, "Nonlinearity of the Piezoresistance Effect of p-Type Silicon Diffused Layers," *IEEE Transactions on Electron Devices,* vol. ED-29, pp. 71-77, 1982.
[99] A. Loui, S. Elhadj, D. J. Sirbuly, S. K. McCall, B. R. Hart, and T. V. Ratto, "An analytical model of thermal drift in piezoresistive microcantilever sensors," *Journal of Applied Physics,* vol. 107, 2010.

[100] Y. Zhou, Z. Wang, Q. Zhang, W. Ruan, and L. Liu, "A Front-Side Released Single Crystalline Silicon Piezoresistive Microcantilever Sensor," *IEEE Sensors Journal,* vol. 9, pp. 246-254, 2009.

[101] M. Despont, J. Brugger, U. Drechsler, U. Durig, W. Haberle, M. Lutwyche, *et al.*, "VLSI-NEMS chip for parallel AFM data storage," *Sensors and Actuators,* vol. 80, pp. 100-107, 2000.

[102] B.-H. Kim, S. Park, H.-C. Kim, K. Chun, D.-I. D. Cho, J.-W. Lee, *et al.*, "MEMS fabrication of high aspect ratio track-following microactuator for hard disk drive using silicon on insulator," presented at the Twelfth IEEE International Conference on Micro Electro Mechanical Systems, Orlando, 1999.

[103] P. T. J. Gennissen and P. J. French, "Sacrificial oxide etching compatible with Aluminum metallization," presented at the 1997 International Conference on Solid State Sensors and Actuators, Chicago, 1997.

[104] J. F. L. Goosen, B. P. v. Drieenhuizen, P. J. French, and R. F. Wolffenbuttel, "Problems of sacrificial etching in the presence of aluminium interconnect," *Sensors and Actuators A,* vol. 62, pp. 692-697, 1997.

[105] M. Bartek and R. F. Wolffenbuttel, "Dry release of metal structures in oxygen plasma: process characterization and optimization," *Journal of Micromechanics and Microengineering,* vol. 8, pp. 91-94, 1998.

[106] N. Fujitsuka and J. Sakata, "A new processing technique to prevent stiction using silicon selective etching for SOI-MEMS," *Sensors and Actuators A,* vol. 97-98, pp. 716-719, 2002.

[107] M. G. Buehler and C. W. Hershey, "The Split-Cross-Bridge Resistor for Measuring the Sheet Resistance, Linewidth, and Line Spacing in Conducting Layers," *IEEE Transactions on Electron Devices,* vol. ED-33, pp. 1572-1579, 1986.

[108] S. Enderling, C. L. Brown, S. Smith, M. H. Dicks, J. T. M. Stevenson, M. Mitkova, *et al.*, "Sheet Resistance Measurement of Non-Standard Cleanroom Materials Using Suspended Greek Cross Test Structures," *IEEE Transactions on Semiconductor Manufacturing,* vol. 19, pp. 2-9, 2006.

[109] L. J. v. d. Pauw, "A method of measuring specific resistivity and hall effect of discs of arbitrary shape," *Philips Research Reports,* vol. 13, pp. 1-9, 1958.

[110] R. W. Carpick and M. Salmeron, "Scratching the Surface: Fundamental Investigations of Tribology with Atomic Force Microscopy," *Chemical Reviews,* vol. 97, pp. 1163-1194, 1997.

[111] M. Z. Baykara, T. C. Schwendemann, B. J. Albers, N. Pilet, H. Monig, E. I. Altman, *et al.*, "Exploring atomic-scale lateral forces in the attractive regime: a case study on graphite (0001)," *Nanotechnology,* vol. 23, 2012.